ZEOLITES AS HOST MATERIALS:
SYNTHESIS, POST-SYNTHESIS TREATMENTS AND ANTIMICROBIAL
PROPERTIES OF ZEOLITES

A THESIS SUBMITTED TO
THE GRADUATE SCHOOL OF NATURAL AND APPLIED SCIENCES
OF
MIDDLE EAST TECHNICAL UNIVERSITY

BY

MELDA İŞLER BİNAY

IN PARTIAL FULFILLMENT OF THE REQUIREMENTS
FOR
THE DEGREE OF DOCTOR OF PHILOSOPHY
IN
MICRO AND NANOTECHNOLOGY

DECEMBER 2021

Approval of the thesis:

**ZEOLITES AS HOST MATERIALS:
SYNTHESIS, POST-SYNTHESIS TREATMENTS AND ANTIMICROBIAL
PROPERTIES OF ZEOLITES**

submitted by **MELDA İŞLER BİNAY** in partial fulfillment of the requirements for
the degree of **Doctor of Philosophy in Micro and Nanotechnology, Middle East
Technical University** by,

Prof. Dr. Halil Kalıpçılar
Dean, Graduate School of **Natural and Applied Sciences**   _____

Prof. Dr. Deniz Üner
Head of the Department, **Micro and Nanotechnology**   _____

Prof. Dr. Burcu Akata Kurç
Supervisor, **Micro and Nanotechnology, METU**   _____

Assoc. Prof. Dr. Didem Kart
Co-Supervisor, **Pharmaceutical Microbio., Hacettepe Uni.**   _____

Examining Committee Members:

Prof. Dr. Emren Nalbant
Chemistry, METU   _____

Prof. Dr. Burcu Akata Kurç
Micro and Nanotechnology, METU   _____

Assoc. Prof. Dr. Çağdaş Devrim Son
Biology, METU   _____

Prof. Dr. Serdar Sezer
Pharmacology, Süleyman Demirel Uni.   _____

Prof. Dr. Eda Ayşe Aksoy
Basic Pharmaceutical Sciences, Hacettepe Uni.   _____

Date: 21.12.2021

I hereby declare that all information in this document has been obtained and presented in accordance with academic rules and ethical conduct. I also declare that, as required by these rules and conduct, I have fully cited and referenced all material and results that are not original to this work.

Name Last name : Melda İşler Binay

Signature :

ABSTRACT

ZEOLITES AS HOST MATERIALS:
SYNTHESIS, POST-SYNTHESIS TREATMENTS AND ANTIMICROBIAL
PROPERTIES OF ZEOLITES

İşler Binay, Melda
Doctor of Philosophy, Micro and Nanotechnology
Supervisor : Prof. Dr. Burcu Akata Kurç
Co-Supervisor: Assoc. Prof. Dr. Didem Kart

December 2021, 145 pages

The development of more efficient and eco-friendly antimicrobial agents with a broader spectrum plays a significant role in culminating prolonged treatment and higher global health. However, the worldwide rise multidrug-resistant bacteria has made traditional approaches to controlling infectious diseases problematic. As a result, developing new classes of antimicrobial medicines capable of treating resistant bacteria is critical. It is stated that using a host as a matrix in applying some antimicrobial agent increases the antimicrobial activity and offers tailorable release. This thesis aims to contribute to the literature with the newly developed antimicrobial host-guest systems.

In the first part of this study, the process of converting the impurity containing locally available natural kaolin into an antimicrobial filler and adding it to the electrostatic powder paint was investigated. In this process, several combinations of binary metal exchanged zeolite A crystals were studied, and an antimicrobial powder paint was developed in partnership industry with IBA KIMYA. The Ag^+ and Zn^{2+} exchanged zeolite A crystals were added into

electrostatic powder paint for this aim, verifying esthetic regulations fulfilling the need of the powder paint industry. The usage of silver has been a controversial issue due to the increased silver contamination in the environment in the last decades. Thus, the second and third parts of the thesis were established based on the need for new environmentally-friendly antimicrobial agents. In the second part of the thesis, the novel antimicrobial host-guest system was developed using thymol, the main component of essential oil thyme, and Titanosilicate ETS-10 crystals. For the encapsulation of thymol, post-treatment of ETS-10 was applied to obtain a hierarchical pore structure in ETS-10. This approach enabled one to enhance the amount loaded and extend the release profile for the purpose of increased antimicrobial efficiency obtained from thymol encapsulation. In the last part of this study, the first two approaches were combined by bringing Zn^{2+} and thymol in the post-treated zeolite X. This superior system offered more effective antimicrobial activity than its counterparts; i.e., thymol/Zn-commercial zeolite X or thymol-post-treated zeolite X systems.

This thesis proposes antimicrobial post-treated carriers to support large thymol payloads that take advantage of a complex form, offering controlled and tailorable release. The high accessibility of the surface area coming from the post-treated process was key to obtain these results. We believe that these systems are suitable for large-scale applications and show potential compared to those seeking antimicrobial solutions.

Keywords: Post-synthesis Treatments for Zeolites, Antimicrobial Activity, Essential Oils, Metal Cations, Sustained Release.

ÖZ

KONAK MALZEME OLARAK ZEOLİTLER: SENTEZ, SENTEZ SONRASI İŞLEMLER VE ANTİMİKROBİYAL ÖZELLİKLERİ

İşler Binay, Melda
Doktora, Mikro ve Nanoteknoloji
Tez Yöneticisi: Prof. Dr. Burcu Akata Kurç
Ortak Tez Yöneticisi: Doç. Dr. Didem Kart

Aralık 2021, 145 sayfa

Daha geniş spektrumlu, daha etkin ve çevre dostu antimikrobiyal ajanların geliştirilmesi, uzun soluklu tedavide ve daha iyi bir küresel sağlığın elde edilmesinde önemli bir rol oynamaktadır. Bunula birlikte, dünya çapında çoklu ilaca dirençli bakterilerin yükselişi, bulaşıcı hastalıkları kontrol etmede geleneksel yaklaşımları sorunlu hale getirdi. Sonuç olarak, dirençli bakterileri tedavi edebilen yeni antimikrobiyal ilaç sınıflarının geliştirilmesi kritik öneme sahiptir. Bazı antimikrobiyal ajanların uygulanmasında bir konak yapısının matris olarak kullanılmasının, antimikrobiyal aktiviteyi arttırdığı ve uyarlanabilir salınım sunduğu belirtilmektedir. Bu tez, yeni geliştirilen antimikrobiyal konak-konuk sistemleri ile literatüre katkı sağlamayı amaçlamaktadır.

Bu çalışmanın ilk bölümünde, yerel olarak temin edilebilen doğal saf olmayan kaolinden zeolite A kristalleri üretilerek, antimikrobiyal dolgu maddesine dönüştürülmüş ve bu dolgu maddesinin elektrostatik toz boyaya eklenme süreci incelenmiştir. Bu süreçte, ikili metal yüklenmiş zeolit A kristallerinin çeşitli kombinasyonları incelenmiş ve endüstri ortağımız olan IBA KİMYA ile antimikrobiyal toz boya geliştirilmiştir. Bu amaçla, elektrostatik toz boyaya, Ag^+ ve

Zn^{2+} yüklenmiş zeolit A kristalleri eklenerek toz boya sektörünün ihtiyacına cevap veren estetik parametreler karşılanmıştır. Son onyıllarda çevrede artan gümüş kirliliği nedeniyle gümüş kullanımı tartışmalı bir konu olmuştur. Bu sebeple, tezin ikinci ve üçüncü bölümleri, çevre dostu yeni antimikrobiyal ajanlara duyulan ihtiyaçtan yola çıkılarak oluşturulmuştur. Tezin ikinci bölümünde, kekik uçucu yağının ana bileşeni olan timol ve Titanosilikat ETS-10 kristalleri kullanılarak yeni antimikrobiyal konuk-konak sistemi geliştirilmiştir. Timolün kapsüllenmesi işleminden önce, ETS-10'da hiyerarşik bir gözenek yapısı elde etmek için sentez-sonrası işlemler uygulanmıştır. Bu yaklaşım, timol kapsüllemesi sürecinde daha fazla timol yüklenmesini sağlayarak, antimikrobiyal etkinliğinin arttırılmasına ve salınım süresinin uzatılmasına olanak sağlamıştır. Bu çalışmanın son bölümünde, ilk iki yaklaşım birleştirilmiş ve sentez-sonrası işlemden geçirilerek hiyerarşik bir gözenek yapısı oluşturulmuş zeolit X kristallerine, hem Zn^{2+} katyonları hem de timol molekülleri yüklenmiştir. Bu üstün sistem emsallerinden yani, timol/Zn-zeolit X veya timol-sentez-sonrası işleme tabi tutulmuş zeolit X sistemlerinden daha etkin antimikrobiyal aktivite sunmuştur.

Bu tez, kontrollü ve uyarlanabilir salınım sunan ve daha fazla miktarda timol yüklenmesine olanak sağlayan sentez-sonrası işlemlerden geçirilmiş antimikrobiyal taşıyıcılar önermektedir. Sentez-sonrası işlemlerinin sağladığı gözenek yüzey alanın artışı, bu sonuçların elde edilmesinde kilit rol oynamıştır. Bu sistemlerin, büyük ölçekli uygulamalar için uygun olduğu ve antimikrobiyal çözümler arayanlara alternatif sunduğu düşünülmektedir.

Anahtar Kelimeler: Zeolitlerde sentez-sonrası işlemler, Antimikrobiyal etkinlik, Uçucu yağlar, Metal Katyonlar, Sürekli Salınım.

To my great lovely family

ACKNOWLEDGMENTS

TABLE OF CONTENTS

LIST OF FIGURES

xviii

LIST OF TABLES

CHAPTER 1

INTRODUCTION

All over the world, infections based on pathogens are crucial problems in lots of areas. Nearly 80% of human infections occur from microbe-contaminated surfaces. Therefore, there is an apparent and crucial demand to prevent the surfaces of typical items from pathogenic microorganisms inducing potential health risks. In textile materials, cross-infection presents a vital problem, especially in hospitals. The communal use of bed sheets, pillowcases, and drapes can provide cross infections. The pathogenic bacteria could transfer to patients, visitors, and staff through these textile materials. Natural products such as cotton are more prone to transmitting microbes than synthetic materials due to having a porous and hydrophilic structure that preserves the proper environment needed for microbial growth. Antimicrobial food packaging is of considerable attention in the food industry due to customer demand and market trends. Active packaging approaches allow controlling the microbial decomposition of fresh food to provide controlled release of additives into food over a lengthy period of time, limiting the potential for unwanted flavors induced by the direct addition of these additives into food. Another demand for antimicrobial additives is water treatment applications. Contaminated water may include infective bacteria that infect humans by direct touch or oral ingestion, resulting in waterborne illnesses. For this reason, antimicrobial membrane-based filtration systems have been developed during the last 30 years to meet increased global demands for potable water supply and wastewater treatment.

Transition group metal cations such as silver and zinc are the most often used ions for antimicrobial activity in many applications due to their higher biocidal activity. Silver cations have been the most effective and thus the most preferred

1

antimicrobial agent used in the industry. Zinc cations also exhibit the necessary antimicrobial activity. Furthermore, the binary use of silver and zinc cations is known to increase the antimicrobial activities observed with respect to singular ionic systems. The methods necessitate utilizing fewer materials, comprising less toxic elements in an affordable and scalable fashion as antibacterial solutions. However, the usage of silver led to several controversial arguments about environmental and sustainability issues, such as lack of resources, utilization of water, utilization of energy, and human health.

In comparison with metallic cations, Essential oils offer much promise as antimicrobial agents with their organic structures. However, these bioactive organic molecules are volatile compounds, and they can quickly lose their antimicrobial activity with contacting air and at harsh conditions. The encapsulation process is the most inspiring solution to control the release of these organic compounds. This encapsulation process also ensures that the metal nanoparticles are well dispersed in the host material, increasing the surface area of the metal nanoparticles and providing a better antimicrobial result using fewer nanoparticles.

The use of zeolites and zeo-type materials as host materials is attractive due to their well-defined, uniform pore size and improved chemical, thermal and mechanical properties. Since the channels and pores of zeolites are in the lower range of the nanometer scale, the guest molecules incorporated into zeolites must also be of nanometer scale. The nanometer-scale porosity opens the possibility of selective sorption in zeolites. Different zeolites with pore structures and morphologies can be incorporated with metal nanoparticles, metal complexes, and organic substances for forming host-guest systems with desirable properties. Performing a hierarchical formation process for zeolites could increase the possibility of obtaining maximum efficiency for the host-guest encapsulation method.

This thesis contains three different antimicrobial host-guest systems, each of them explained in separate chapters. In the first part of this thesis, one of the most common antimicrobial agents, silver, was ion-exchanged with sodium cations in the zeolite LTA framework. Another significant part of this study was that the Zeolite A crystals were obtained from locally available kaolin resources in Turkey, making the process more feasible. This part of the thesis was accomplished as part of the SANTEZ project, opening the possibility of turning our developed product into powder paint in collaboration with IBA KIMYA. For that purpose, the silver and zinc exchanged zeolite A crystals were introduced into electrostatic powder paint, confirming esthetic regulations in the obtained coatings that satisfied the demand for the powder paint industry.

In the second part of this thesis, to meet the search for an environmentally friendly alternative to antibacterial agents used in industry with enhanced sustainability, thymol molecule with well-known antibacterial properties for centuries was chosen as an essential oil product. In order to encapsulate thymol into the nanopores of zeolites, firstly, the zeo-type framework was turned onto a hierarchical nature. This allowed the formation of enlarged pores in the titanosilicate ETS-10, which is the chosen model of zeo-type material to encapsulate thymol molecule. The formation of defects in the ETS-10 framework was performed with post-synthesis treatment methods after synthesis of ETS-10 to increase absorption of thymol molecules into ETS-10. This encapsulation process offered novel absorption properties of thymol molecules.

In the last part, environmentally friendly thymol molecules were also encapsulated into a more commercially available zeolite type of zeolite 13X to be a pioneer in alternative industrial studies. In this process, hierarchical zeolite formation methods were applied to generate hierarchical pores, followed by applying the ion-exchange protocol with zinc cations in accordance with the previously developed know-how during the study.

1.1. Antimicrobial Materials

There is an increasing amount of research on health issues related to microorganism-induced diseases. The antimicrobial materials could be divided into two groups, namely inorganic and organic compounds. Transition group metals and related chelating compounds displaying outstanding antimicrobial activity are utilized as inorganic antimicrobial compounds. As organic compounds, essential oils extracted from plants have been known for centuries to offer a good antibacterial effect against several pathogenic microorganisms.

1.1.1. Metal Cations and Nanoparticles as Antimicrobial Agents

Metal cations and nanoparticle forms of these cations indicate remarkable antimicrobial activity against several microorganisms. The most popular ones are the silver cations (Ag^+), whereas zinc (Zn^{2+}) and copper (Cu^{2+}) are also the other superior ones.

1.1.1.1. Silver as Antimicrobial Agent

Silver is a lustrous, soft transition metal with the highest reflectivity among all metals. The most frequent attribute of silver is that it possesses antimicrobial properties. When silver is diffused into its monoatomic ionic state (Ag^+), which is soluble in aqueous settings, it is known to act as a biocide. This form is the same form found in ionic silver compounds like silver nitrate and silver sulfadiazine, which have been used to treat wounds for a long time. Silver could also be found in metallic nanoparticle form (Ag^0) exhibiting antimicrobial activity [1].

Silver has been adopted to prevent the spread of disease in humans throughout history by introducing it into consumer goods. The first reported use of silver for therapeutic purposes comes from the Han Dynasty in China, around 1500 B.C.E. [2]. Pharmaceutical grade silver, such as silver nitrate, silver sulfadiazine, and colloidal silver, is used in modern medicine. The development of silver as an antibacterial agent

4

ceased when antibiotics were discovered in the early twentieth century. However, in recent years, increased bacterial resistance to most antibiotics has prompted a re-evaluation of the possibilities [1,3].
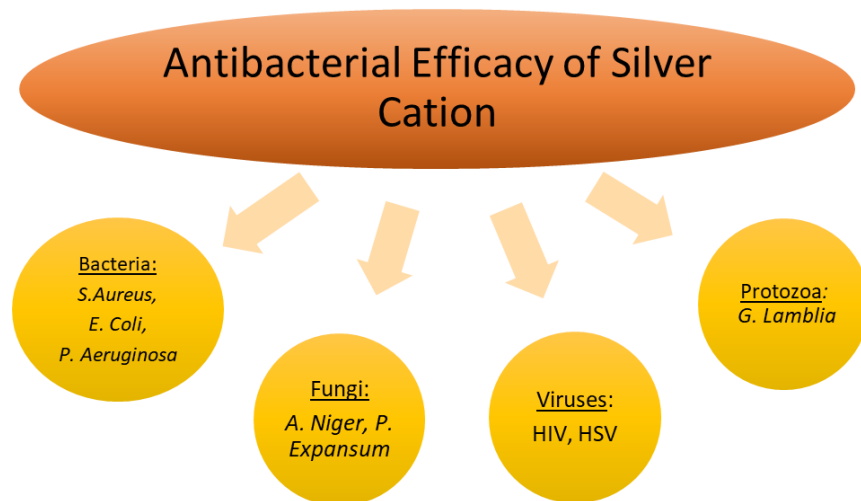
Figure 1. 1. The Broad-spectrum antimicrobial efficacy of silver cations. *S. aureus: Staphylococcus aureus, E.coli: E*scherichia coli*, P.aeruginosa: Pseudomonas aeruginosa*, *A. niger: Aspergillus niger, P. expansum: Penicillium expansum* HIV: Human immunodeficiency virus, HSV: Herpes Simplex Virus 1, *G. lamblia: Gardia lamblia.*

Broad-spectrum antimicrobial silver cations have been proven to knock out a wide range of pathogenic organisms from many classes within species of viruses, bacteria, and fungi (Figure 1.1). Silver cations exhibit remarkable antimicrobial efficacy against bacteria [4–6], fungi [7], viruses [8], and protozoa [9].
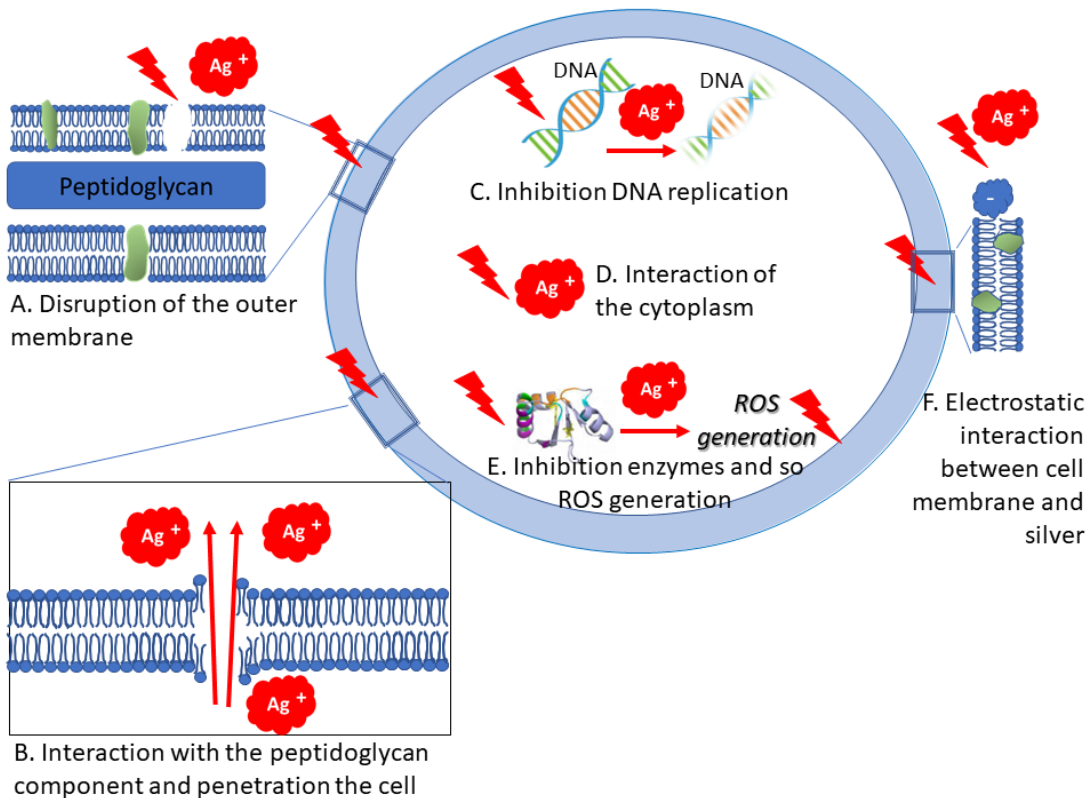
Figure 1. 2. The antibacterial mechanism of silver cations. (A) Disruption of the outer membrane. (B) Interaction with the peptidoglycan component and penetration of the cell. (C) Inhibition DNA replication. (D) Interaction of cytoplasm. (E) Inhibition enzymes and so ROS generation. (F) Electrostatic interaction between the cell membrane and silver cations.

The biocide activity mechanism of silver against bacteria is still not clearly understood. Nonetheless, several noticeable biocide mechanisms of silver cations were stated in the literature. Figure 1.2 indicates the antimicrobial mechanism of silver cations. The antimicrobial activity mechanism of silver cations was listed below;

A. Inhibition of silver cations disrupts the outer membrane [5].
B. Silver cations create pores and penetrate through the bacterial cell by interacting with the peptidoglycan component of the bacterial cell wall [10].

C. The cytoplasm membrane dwindles, and DNA becomes its condensed form after the penetration. DNA molecules lose their replication ability, resulting in the hindrance of cell growth [10].

D. The primary antimicrobial activity originates from the interaction of the cytoplasm of the living cell with silver cations [5].

E. Silver cations inhibit the activity of respiratory enzymes, resulting in reactive oxygen species (ROS). ROS have been linked to oxidative stress by causing damage to DNA, cell membranes, and cellular proteins [4].

F. The electrostatic interaction between the negatively charged cell membrane and positively charged silver cations account for biocidal activity [11].

Multiple antibacterial silver action modes, which target a wide range of microbe biological pathways, benefit from preventing pathogen-based illnesses.

1.1.1.2. Zinc as Antimicrobial Agent

Zinc (Zn^{2+}) is necessary for microorganisms and complex organisms since it is associated with many critical biological mechanisms at its low endogenous level [12,13]. Zinc content in the blood is 10^{-4} M. For catalytic and structural functions, optimal rates of this cofactor are required [14]. Several transporters regulate zinc concentration in physiological conditions; hence Zn^{2+} cations are not mostly destructive to advanced organisms. Zinc intake by cells is controlled by homeostasis [15]. Increasing Zn^{2+} concentrations above ideal levels disrupt Zn^{2+} homeostasis and let Zn^{2+} penetrate the cells, making it toxic to prokaryotes due to higher concentration [16]. As a result, Zn^{2+} may behave as an antibacterial or antifungal agent. Indeed, Zn^{2+} has been accepted to have antimicrobial properties against bacterial and fungal strains. Zn^{2+} cations display similar antimicrobial mechanisms with Ag^+ cations. Like Ag^+ cations, Zn^{2+} cations can also destroy the cell membrane and penetrate the cell [17].

1.1.2. Essential oils as Antimicrobial Agents

Essential oil (EO) extracts of plants exhibit remarkable antimicrobial, antiviral, and antioxidant activity. The extracts are volatile aromatic compounds symbolized by an intense odor. They are attained mainly by distillation, firstly in the Middle Ages. EOs have been widely investigated as antimicrobial, antiviral, anesthetic, anti-inflammatory, sedative, and locally anesthetic solutions. The complex nature of EOs has a crucial role in protecting plants against microorganisms and herbivores by lowering their appetite. Mediterranean and warm countries host various aromatic plants whose extracts consist of these biologically active EOs. EOs are volatile, liquid, translucent, infrequently colored, soluble in organic solvents and lipid structures. They could be extracted from all the components of plants such as fruits, wood, leaves, and stems [18].

1.1.2.1. Constituents of Essential Oils

Many bioactive compounds comprise EOs, and they have broad alterations in chemical profiles such as terpenoids, aldehydes, and phenolic compounds. Figure 1.3 shows some common ones: thymol, carvacrol, carvone, cinnamaldehyde, limonene, citral, p-cymene, eugenol, and menthol.
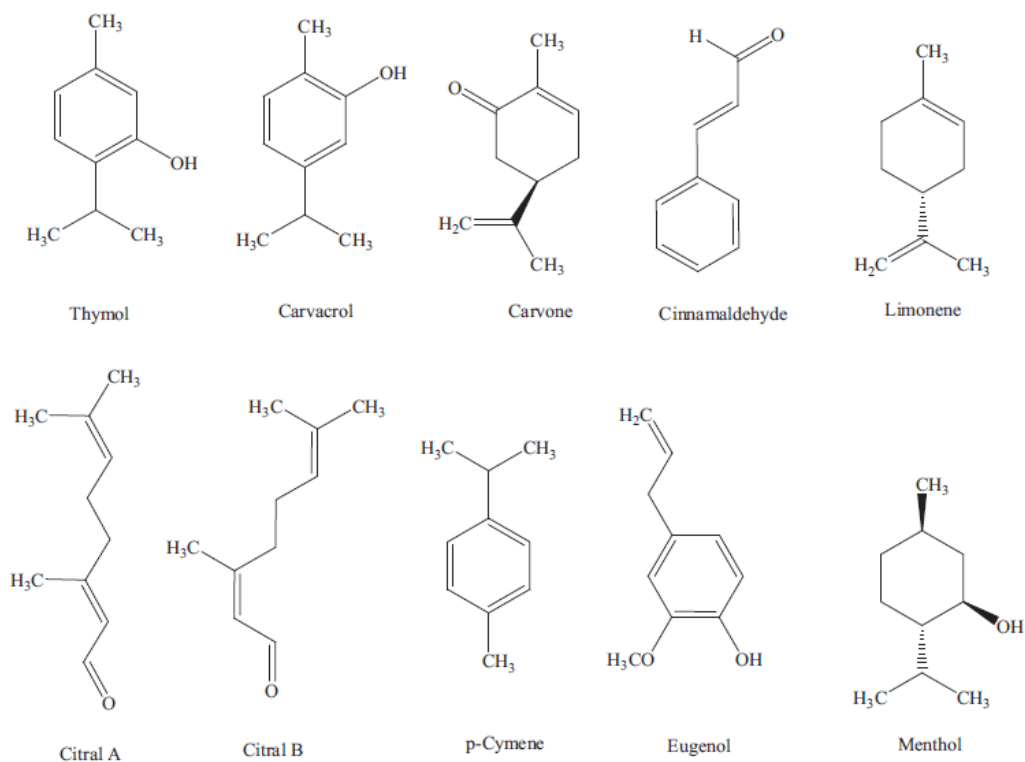
Figure 1. 3. Chemical structure of thymol, carvacrol, carvone, cinnamaldehyde, limonene, citral, p-cymene, eugenol, and menthol [19].

1.1.2.2. The antimicrobial mechanisms of essential oils

All bacteria were classified into two groups: namely gram-positive and gram-negative bacteria. The distinction between these two groups is based on the cellular surface nature of bacteria (Figure 1.4). The cell wall of gram-positive bacteria comprises a thick layer of peptidoglycan made of amino acids and sugars. However, the cell wall of gram-negative bacteria is the combination of thin peptidoglycan and an outer membrane composed of lipopolysaccharides and phospholipids.
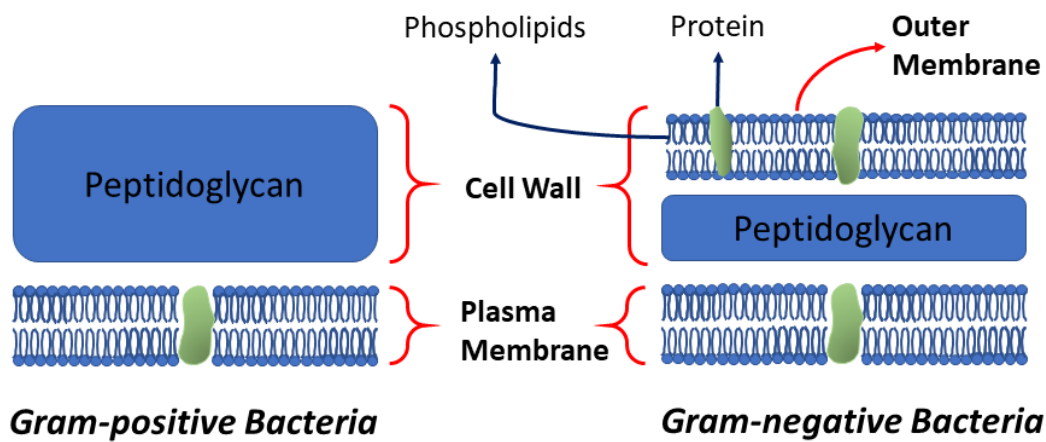
Figure 1. 4. Schematic representation of cell wall structures of gram-positive and gram-negative bacteria.

The difference in cell wall composition leads to the difference in antimicrobial efficacies of biocides. The chemical composition of the gram-positive bacteria cell wall lets hydrophobic molecules penetrate cells. Hydrophobic biocide molecules can disturb enzymes that are responsible for the production of energy. Also, they can change the nature of membrane proteins [20]. This hydrophobic character also leads to splitting the lipids in the bacterial cell membrane. Then, this split process brings about higher permeability in the membrane, membrane expansion, the ruin of membrane proteins, and so a change in ion transport selectivity [21,22]. Thus, the draining of ions or organelles from the cytoplasm could occur [23]. Gram-negative bacteria are more resistant to biocide molecules due to the outer membrane structure of lipopolysaccharides. The outer membrane of gram-negative bacteria has porin proteins which are hydrophilic transmembrane channels. Having hydrophilic channels makes the outer membrane more hydrophilic and resistant to hydrophobic biocide molecules [24].

ATP synthase enzymes responsible for ATP synthesis from ADP are obstructed in the presence of EOs. Thus, the associated bacteria lose its critical cellular activities due to the lack of energy sources such as providing nutrients. The lack of bacteria's fundamental needs brings about cell death [24].
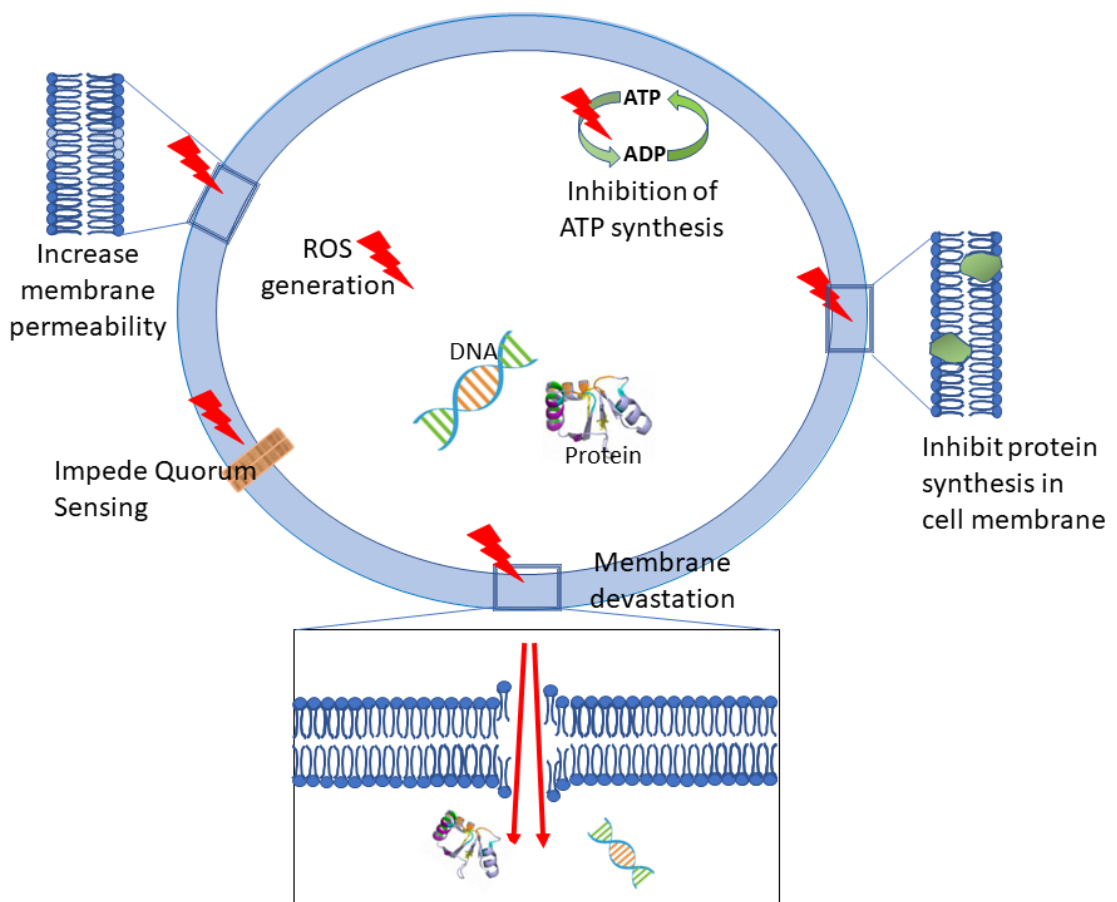
Figure 1. 5. An illustration of the antimicrobial mechanism of EOs against bacteria.

EOs also cause reactive oxygen species (ROS) formation, provoking cell apoptosis and oxidative stress [25]. Interruption of plasma membrane presented by EOs could increase saturated fatty acids in the lipid bilayer and consequently enhance

instability of the unsaturated fatty acid in the cell membrane and rigidity of membrane [26,27]. Figure 1.5. illustrates the antimicrobial mechanism of EOs against bacteria.

EOs are a combination of biocide compounds. The mechanism of antimicrobial activity of EO depends on the type of these bioactive compounds. It is more reliable to discuss several antimicrobial mechanisms for EOs instead of specific antimicrobial mechanisms [23].

Various compounds can hinder membrane protein synthesis, causing cell membrane breakdown. The inhibition of heat-shock compression in bacterial pathogens by carvacrol and *p*-cymene is an example of hindrance protein synthesis. Furthermore, thymol and eugenol disturb lipid-protein interaction and alter protein contours of the plasma membrane [27]. Similarly, limonene causes damages to proteins, fatty acids, nucleic acids in the cell constitution of bacteria [28].

Another vital activity of bacteria is quorum sensing which requires the communication of bacteria with each other, resulting in the adaptation of bacteria to their environment [29]. The signaling molecules of bacteria, such as acyl-homoserine lactones, are responsible for this communication. Cinnamaldehyde is the inhibitor of this communication and results in quorum sensing inactivation [27].

EOs acquire fungicides activity like biocide activity. Ergosterol is one of the vital sterols in the cell membrane structure of fungi. The lipophilic compounds of EOs could penetrate the cell and reach the synthesis pathway of ergosterol and then ruin its synthesis. Also, hydroxyl groups of EOs can react with the membrane of fungi, leading to significant lesions [30]. Similarly, thymol tends to bind ergosterol in the fungi membrane, which raises ion permeability and, lastly, causes cell death [31].

Thymol and (S)-limonene also inhibit pectin methyl esterase (PME), whose role is to modify significant pectins of fungi cell walls. This inhibition alters plasticity,

cellular adhesion, pH, and ionic contents of the cell wall and induces fungi growth, membrane permeability, and integrity [32].

1.2. Zeolites and Zeo-type materials

Zeolites and zeo-type materials have a crystalline structure and framework linked tetrahedra units that comprise open cavities in the forms of channels with well-defined acidity, good thermal stability, and cation exchange selectivity. Their porous structure and cationic nature make these unique materials suitable for ion exchange, adsorption, and catalysis [33].

Zeolites consist of crystalline aluminosilicates with corner-sharing TO_4 tetrahedra, consisting of SiO_4 and AlO_4. These regular tetrahedra sequences form three-dimensional frameworks containing uniform pore sizes. Each T-atom is coordinated by four oxygen atoms from tetrahedral sites, and each oxygen atom is bonded to two T-atom. The coordination of zeolite T-atom leads to several possible frameworks [34]. The difference in the framework comes from the ratio of Si to Al and the crystal morphology. Zeolite crystal morphology could be altered by the gel composition, chemicals, crystallization time, and temperature [35]. Over 1000 unique zeolites are mentioned in the Atlas of Zeolite Structure [36]. In addition to creating zeolites with Si and Al atoms, using P, Ga, Ge, and Ti atoms instead of Si and Al for T atoms can produce zeo-type materials [37].

Most popular zeolites and Engelhard titanosilicate ETS-10 as zeo-type material are typically classified by framework type and pore size in Table 1.1. Membered rings are described as the number of Si or Al/Ti atoms on the smallest possible cross-section.

The zeolite framework, consisting of SiO_4 and AlO_4 tetrahedra, has an anionic framework character due to AlO_4 tetrahedra. Extra-framework cations stabilize the structure. The general empirical formula can be represented as;

$$M_{y/n}^{n+}[(SiO_2)_x.(AlO_2^-)_y. z\, H_2O] \qquad (1.1)$$
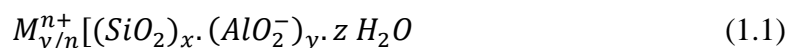
where *M* is an extra-framework cation with n^+ charge.

Table 1. 1. Classification of the most common zeolites and ETS-10.

Zeolite	Framework type	Dimensionality	Membered Ring (MR)	Pore Size (Å)
Zeolite A	LTA	3	8	4.2 X 4.2
Zeolite X	FAU	3	12	7.4 X 7.4
Zeolite L	LTL	3	12	7.4 X 7.4
ZSM-5	MFI	3	10	5.5 X 5.1
ZSM-22	TON	1	10	4.6 X 5.7
ZSM-12	MTW	1	12	6.0 X 5.6
Zeolite Beta	BEA	3	12	6.7 X 6.6
MCM-22	MWW	2	10	5.5 X 4.0
Silicalite-1	MFI	3	10	5.5 X 5.1
ETS-10	-	3	12	4.9 X 7.4

The extra-framework cations responsible for balancing the structure are electrostatically bonded to the framework, allowing zeolite to become advantageous for numerous applications. The most widespread applications in zeolites are ion-exchange, selective sorption, and catalysis [38]. Moreover, thanks to zeolites' rigid and porous nature, nanoparticles and conductive polymer materials can be incorporated into the zeolite, improving their optical or conductive properties.

The most common examples for such a host-guest assembly system are zeolite A and zeolite X. Moreover, ETS-10, a titanosilicate microporous material, can be an alternative host for host-guest systems with unique properties.

1.2.1. Zeolite A

Zeolite A (Linde Type A, LTA framework) was the first zeolite produced for its commercialization. It is also known as Zeolite 3A, 4A, or 5A, based on the exchangeable cation in the zeolite structure. Zeolite 4A, which has high demand in industry, has a Si/Al ratio of 1, meaning that it has a high Cation Exchange Capacity (CEC) [39]. The molar formula of zeolite 4A is $Na_{12}[(SiO_2)_{12}.(AlO_2)_{12}].27H_2O$. Si and Al atoms are located alternately in the tetrahedral-based framework, resulting in sodium and aluminum orthosilicates. These orthosilicate anions are constructed, with oxygen atoms ionically bonded to one tetrahedrally coordinated Al^{3+} cation and at least one Na^+ ion each [40].
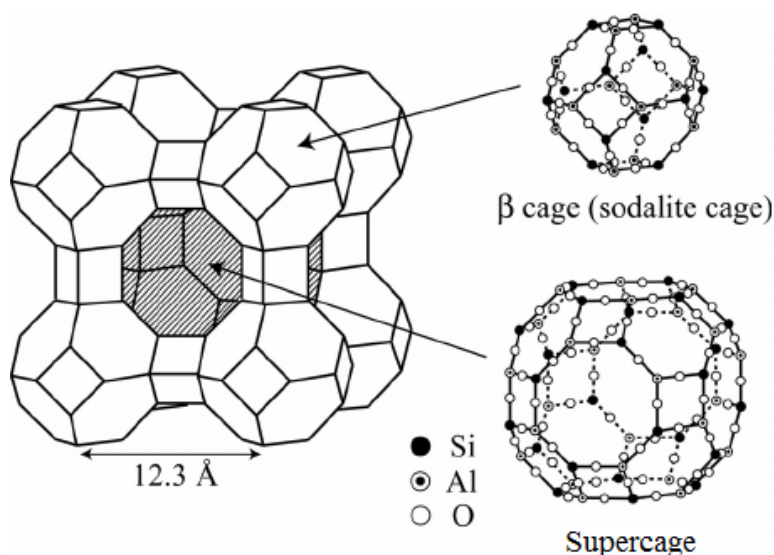
Figure 1. 6. Schematic representation of zeolite A [41].

Zeolite 4A is a small pore-sized zeolite described by a cubic structure. It consists of eight α-cages (or supercages) and eight β-cages (sodalite cages) (Figure 1.6.). The pore diameter is defined by an eight-member oxygen ring and is small at 4.2 Å. This ring structure leads into a larger cavity with a minimum free diameter of 11.4 Å. The cavity is surrounded by the eight sodalite cages (truncated octahedra)

15

connected by their square faces in a cubic structure [42]. The structure has three crystallographically distinct oxygen atoms; 1, 2, and 3 indicate these three distinct oxygen atoms in Figure 1.7.
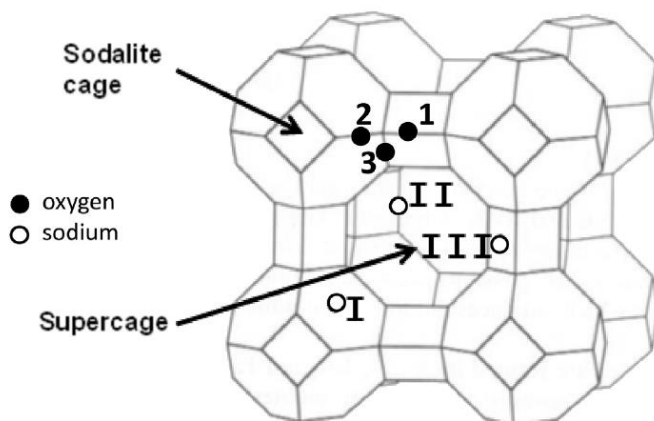
Figure 1. 7. Cation sites in the zeolite A framework [40].

In the zeolite 4A framework, sodium cations fill three main sites, referred to as sites I, II, and III, as illustrated in Figure 1.7. All of them are located almost at the external surface of the supercages. Sites I is positioned at the center of the 6MRs at the border of sodalite cages and supercages, with a slight shift away from the ring's plane and toward the sodalite cage. Sites II interact with three oxygen atoms in the ring and are associated with the 8MRs that separate supercages. They are positioned in the plane of the ring but offset from the ring center. With almost one Na atom per 8MR, site II is nearly half-filled. Site III, which is placed above the center of the 4MRs, has a random occupancy of 5-8%. The supercages, which have a diameter of around 11.4 mm, contain 12 Na^+ atoms on average. As a result, supercages of zeolite A are smaller, but they could contain high amounts of sodium cations. This result lets zeolite A possess a higher ion-exchange capacity [40,43]. Therefore, it is appropriate to use zeolite 4A for the applications in need of ion-exchange, which include antibacterial

applications (Ag^+ exchange), water softeners (Ca^+ exchange), and zeolite 3A (K^+) and 5A (Ca^+) modifications.

1.2.2. Zeolite X

Zeolite X belongs to the Faujasite (FAU) type of zeolite. This type consists of two typical microporous materials depending on the Si/Al ratio: low-silica type X and high-silica type Y. The Si/Al ratio of the typical X type is in the range of 1-1.5, whereas the one of Y type is in the range of 1.5-3 [44].
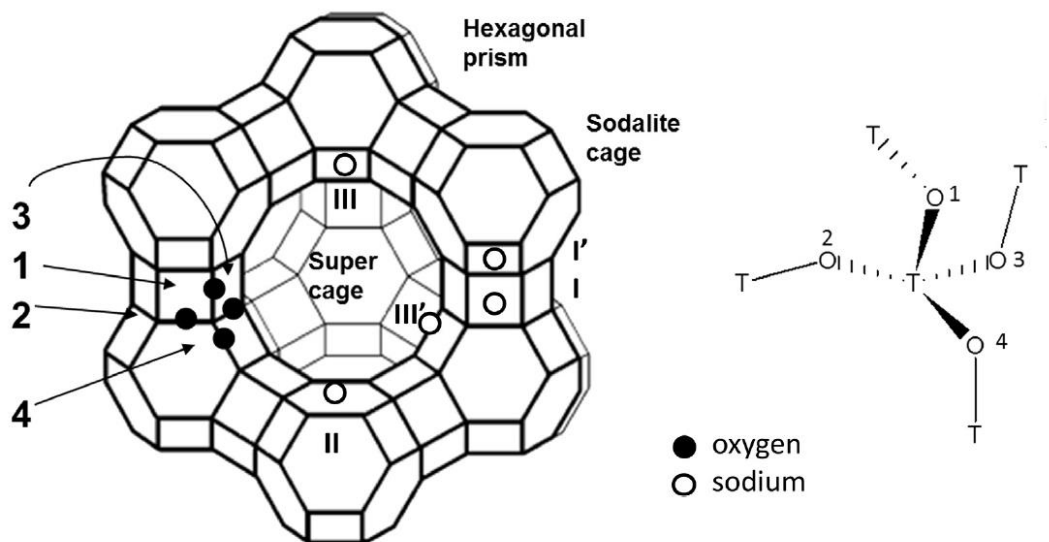
Figure 1. 8. The structure of Na-zeolite X [40].

The FAU is formed by wide supercages accessed through 12-member silicate rings (12MR) with a 7.4 Å diameter. The supercages have a diameter of 13 Å; that is why zeolite X is also referred to as zeolite 13X. The FAU type also has a significantly smaller sodalite cage with access to 6-member silicate rings and hexagonal prisms

linking the sodalite cages. The molar composition of Na- zeolite X is $Na_{96}[Al_{96}Si_{96}O_{384}]$, including eight supercages, eight sodalite cages, and sixteen hexagonal prisms. Figure 1.8 indicates the Na-zeolite X structure. The structure has four crystallographically distinct oxygen atoms, two of which refer to the supercage (1 and 4) and one (2) to the sodalite cage, and the fourth (3) to the hexagonal prism (Figure 1.8). Many extra framework cationic positions might be occupied. Na^+ cations are found on three separate sites in dry faujasites: site I (also known as site I'), site II, and III (also III') [40].

Most researchers assume that sodalite cages and hexagonal prisms, where sites I and I' are positioned, are impenetrable for larger molecules due to the narrow size of the windows. As a result, the supercages would be the location of all faujasite adsorption and catalytic chemistry. These supercages contain on average less than ten Na^+ cations, four of which are positioned at site II and six of which are placed at site III'. These Na ions have considerably weak coordination bonds, and mutual electrostatic repulsion of oxygen atoms may affect them [40].

Zeolite X can be accepted as a proper host for the adsorption of volatile compounds in the host-guest systems to provide controlled release of these compounds [45,46].

1.2.3. Engelhard Titanosilicate ETS-10

Engelhard Titanosilicate ETS-10, first synthesized by Engelhard in 1989, is a significant microporous titanosilicate material with a 3-dimensional network of corner-sharing octahedral TiO_6 and tetrahedral SiO_4 and interconnecting channels and cavities [47,48]. Na^+ and K^+ cations, responsible for balancing the structure, are the exchangeable cations in this framework. The stoichiometry of ETS-10 is represented as $(Na,K)_2TiSi_5O_{13}.nH_2O$. The pore system comprises 12-membered rings and two perpendicular channels letting other molecules penetrate through the pores, possessing pore size with is 4.9 x 7.6 Å [48,49].

ETS-10 crystal structure, unlike other zeolites, has the alteration of long and short bonds along O-Ti-O-Ti-O wires with a diameter of 0.67 nm. This structure has polymorph A (space group $P4_1$ or $P4_3$) and polymorph B (space group $C2/_c$). Polymorph B consist of TiO_3^{2-} chains running through [110] and [11$^-$0] directions, as demonstrated in Figure 1.9 [47,50–52]. Nanoporous SiO_4 with an 8x5 Å pore size encloses each TiO_3^{2-} chain. The lengths of the TiO_3^{2-} molecular chains are larger than 25 nm in highly crystalline ETS-10 [52].
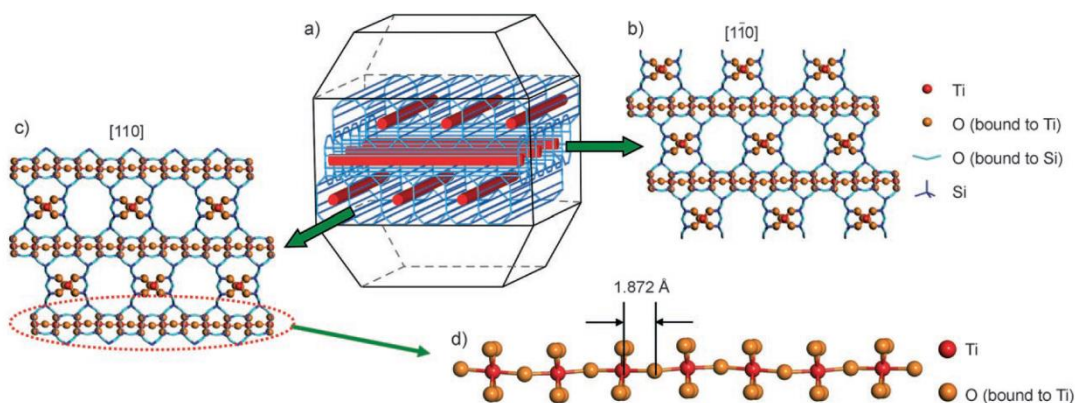
Figure 1. 9. The structure of polymorph B of ETS-10 (a). Truncated-bipyramidal morphology of the ETS-10 crystals with SiO_2 channels (blue) and TiO_3^{2-} chain (red). b) View along the [11$^-$0] axis. c) View along the [110] axis. d) A single TiO_3^{2-} chain [52].

Through scanning electron microscopy, high-resolution electron micrograph, and electron diffraction, it was noticed that ETS-10 could have some structural defects. These defects could be a structural fracture, stacking disorder of broad ellipsoidal pores (12 Si atom rings), 12 membered large rings piled in a diagonal or zig-zag pattern, 3–7 member channels in a straight line, and two equal orthogonal axes in both A and B polymorphs. The sheets are connected in such a way that each one is displaced laterally by one-quarter of a unit cell with the one before it and the one after it. This

shift caused the disorder and faulting of the material's crystal structure. It is important to note that these faults in the ETS-10 structure do not prevent the channel system from absorbing guest molecules. Indeed, this disorder nature requires better access for more giant molecules and enhances the sorption procedure [50,51,53]. Figure 1.10 illustrates an example of defects in ETS-10 channels and pore size caused by defects [51].
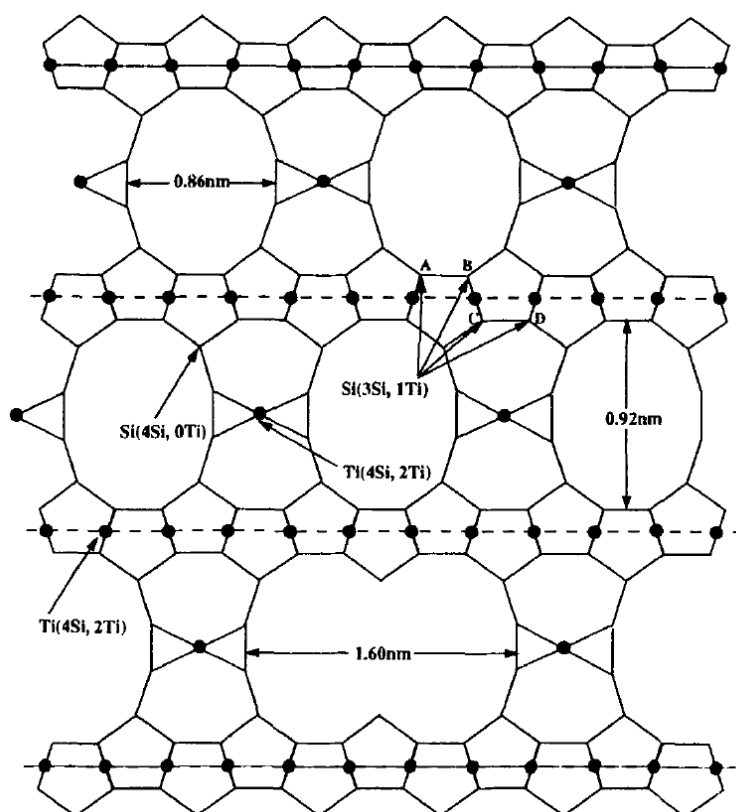
Figure 1. 10. Atomic connectivity in ETS-10. Oxygen atoms are not depicted in the illustration but roughly halfway along each line [51].

Unique TiO_3^{2-} chains arise usage as photochemical and thermal reaction catalysis [49,54,55], photovoltaic solar cell [56], and nanoscale electronic devices [57] for ETS-10 crystals. Moreover, using the ETS-10 in guest-host systems may produce extraordinary results with this unique structure, together with different host molecules.

CHAPTER 2

LITERATURE REVIEW

2.1. Metal Exchanged Zeolites as Antimicrobial Agents

Microbiological infection is becoming a severe problem; therefore, antimicrobial agents were developed to prevent microorganisms' growth [58]. Heavy metals on the nanometer scale, such as silver and zinc, are determined for antimicrobial activity through several bacteria, fungi, and yeast [59]. Although heavy metals have a wide range of bioactivity in microorganisms, a proper host is critical for controlling antimicrobial metals' contact time and efficacy. Crystalline microporous and mesoporous materials, having excellent host properties of ionic or nanoparticle form of metals, have been examined as favorable reinforcement for antimicrobial applications due to safety, durability, and heat resistance [60]. Besides ion-exchanging with heavy metals such as silver and zinc result in odorless and harmless zeolite properties that lead to an increase in the the area of antimicrobial studies.

The literature stated the silver has superior antimicrobial activity against one of the most common pathogenic bacterium, *S. aureus* [61]. The damage of silver to *S. aureus*, gram-positive bacterium, was remarked through transmission electron microscopy (TEM). Figure 2.1 indicates the external morphology of untreated and treated bacteria against silver cation solution. *S. aureus* cells that were not treated maintained their coccal structure, whereas bacteria treated with silver cation solution lost cell integrity [61].

Bar=200nm
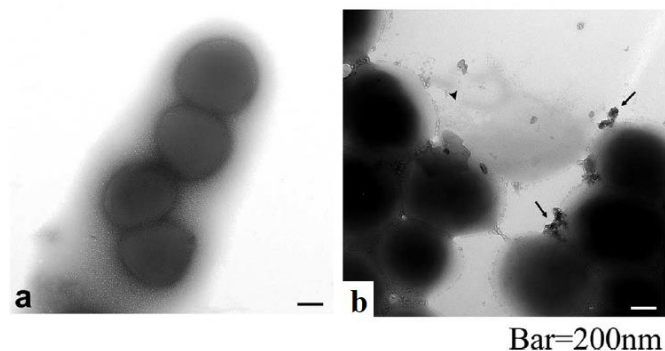
Figure 2. 1. External morphology of *S. aureus* cells observed by TEM of untreated bacteria (a) and bacteria treated with silver ion solution (b). Arrowheads show the release of cellular contents [61].

Untreated *S. aureus* cells displayed typical cell properties and homogenous electron density in the cytoplasm as shown in the cross-section view of TEM images (Figure 2.2). Neither their cell walls nor membranes broke down, indicating a well-preserved peptidoglycan layer and cytoplasmic membrane (Figure 2.2-a-b). However, considerable morphological alterations were detected in *S. aureus* cells treated with silver ion solution. It was also possible to see a localized dissociation of the cell membrane from the cell wall (Figure 2.2-c-d).

Bar=100nm
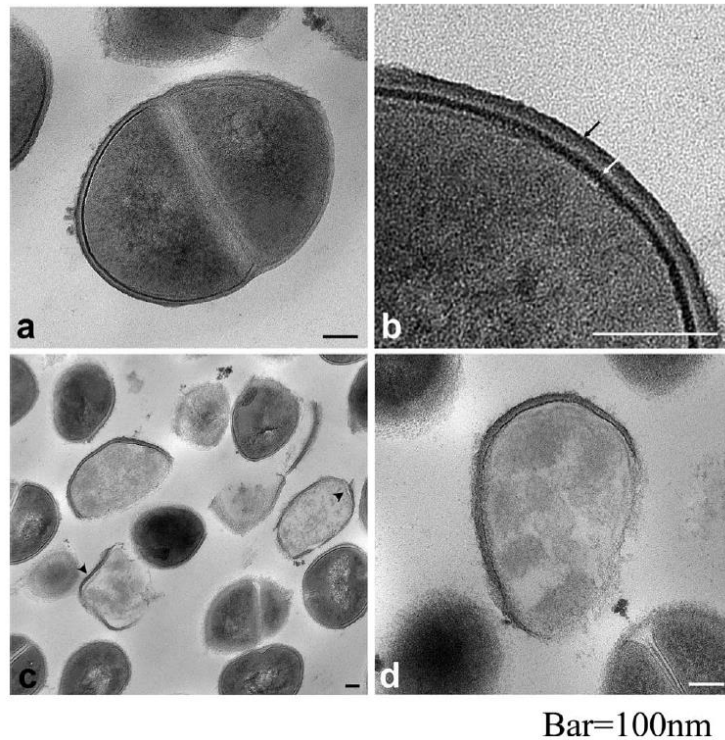
Figure 2. 2. The cross-section TEM images of untreated (a, b) and treated *S.Aurues* (c, d). The peptidoglycan layer and cytoplasmic membrane are denoted by black and white arrows, respectively. Arrowheads show the disconnection of the cell membrane from the cell wall [61].

Top et al. examined the antimicrobial activity of Ag^+, Zn^{2+} and Cu^{2+} exchanged clinoptilolite, which is one of the most traditionally ion-exchangeable natural zeolite [60]. The antimicrobial activity of ion-exchanged clinoptilolite crystals was analyzed against *P. aeruginosa* and *E. coli* by the disk diffusion method. Ion-exchange isotherms revealed significant selectivity of Ag^+ over Na^+, with total replacement of Na^+ observed. Clinoptilolite showed the highest selectivity towards Zn^{2+} and Cu^{2+} over Na^+ only at low concentrations. All the exchanged forms of clinoptilolite exhibited antimicrobial activity. However, it was discovered that increasing metal loading did not necessarily increase antibacterial activity and that a specific limit had to be exceeded.

Matsumura et al. tested the antibacterial capabilities of Ag^+ exchanged zeolite 4A (2.5 wt % Ag, Zeomic) with *E. coli*. After a slow start, the survival rate declined nonlinearly over time. Ion exchange dynamics may be responsible for this characteristic. Additionally, more cells are viable under anaerobic conditions, according to this study. Due to Ag^+-mediated suppression of respiratory enzymes, it was hypothesized that oxygen might lead to ROS production. The close contact of the zeolite and bacteria stimulated antimicrobial activity. The environment or bacteria itself was shown to provide cations (Na^+ and K^+) to exchange Ag^+ [4]. Another study with commercial zeolite 4A was performed by Kaali et al. They examined the ion-exchange behavior of Ag^+, Zn^{2+}, and Cu^{2+} in single, binary, and ternary combinations with zeolite (i.e., Zeomic) [62]. The MIC of single, binary, and ternary ion-exchanged zeolite 4A was evaluated against *S. aureus, Candida tropicalis*, and *P. aeruginosa*. With 5×10^5 CFU/ml of bacteria, the zeolite concentration was changed from 2 to 1024 ppm. The antimicrobial experiments revealed that Ag^+ is more effective than other single ionic systems. The antimicrobial activity of binary and ternary ionic zeolite samples against all three bacteria was similar. This comparable antimicrobial activity was found to be in close relation with the ionic dispersion in the zeolite framework. Accordingly, different ions may obstruct one another's pathway in these systems, affecting ion release and thus antimicrobial activities [62].
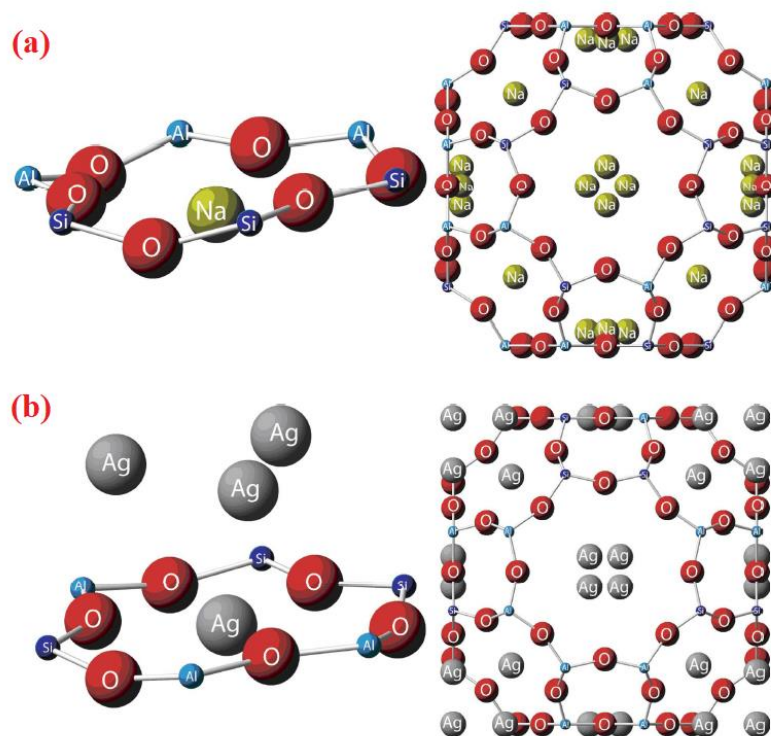
Figure 2. 3. Theoretical distribution of Na^+ ions (a) and Ag^+ ions (b) in the framework of zeolite A [63].

Kaali et al. continued their study to estimate ion distribution in the framework of zeolite 4A based on the ion exchange and release results stated in their previous study [63]. The distribution of silver and sodium ions in the structure is remarkably similar, and the experimental results match the theoretical data quite well. The significant difference is that there are three more silver ions adsorbed into the silver zeolite adsorbed on the edge of the unit cell (Figure 2.3).
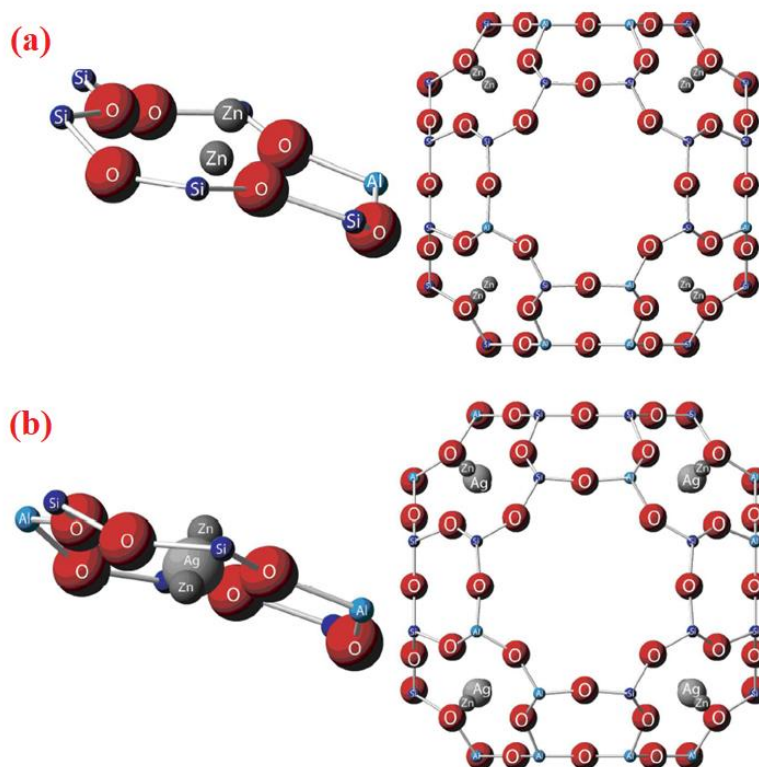
Figure 2. 4. Theoretical distribution of Zn^{2+} ion (a) and Ag^+-Zn^{2+} ion (b) exchanged zeolite A [63].

According to Kaali et al., zinc ions, like sodium and silver, are distributed in the sodalite cages in the zinc exchanged zeolite 4A system, as illustrated in Figure 2.4-a. In most binary and ternary exchanged systems, ion exchange takes place in the sodalite cage areas. The ionic distribution in the silver-zinc system is a little more complicated. According to the release rates in the binary zinc-silver system, one silver ion is surrounded by two zinc ions within the sodalite cage (Figure 2.4-b). As a result, zinc ions on the outer surface readily exchange ions readily available in the solution, whereas the second zinc ion is obstructed by the silver ion, making it less likely to re-exchange with sodium in the solutions [63]. This hindrance directly influences the antimicrobial activity of binary exchanged zeolite systems [62]

Demirci et al. investigated the antibacterial efficacy of Ag^+, Zn^{2+}, and Cu^{2+} exchanged zeolite A and X against bacteria (*S. aureus, E. coli, P. aeruginosa, B. cereus*), yeast (*C. albicans, C. glabrata*), and fungus (*A. Niger, P. vinaceum*) [64]. For bacteria, yeast, and fungi, the incubation periods were 24 hours, 48 hours, and 72 hours, respectively. Ag^+ exchanged samples delivered the highest antibacterial result. The MIC value for *P. aerugino*sa was 32 mg/ml for Ag^+-zeolite X, although 64 mg/ml for the other three bacteria. The MIC value for *B. cereus* was 16 mg/ml in the Ag^+-zeolite A sample, while 32 mg/ml for the other three bacteria. With 2.048 mg zeolite/ml, this Ag^+-zeolite A sample also had the fastest rate of Ag^+ released into the media (39–70 ppm Ag^+ over 0.5–24 h). The MIC value for the bacteria varied from 256 to 2048 mg/ml for the Cu^{2+} and Zn^{2+} exchanged zeolites. The MIC of the Ag^+- zeolites against yeast and fungus ranged from 128 to 1024 mg/ml. In the case of Cu^{2+} and Zn^{2+} exchanged zeolites, the MIC value in yeast and fungus varied between 512 and 2048 mg/ml [64].

It has been reported that Ag^+ exchanged zeolite X (5.8 wt% Ag) had a bactericidal effect against *Staphylococcus aureus, Escherichia coli,* and *Pseudomonas aeruginosa* [6]. When exposed to zeolite loadings of 150–1000 mg/ml, all three bacteria (5 x 10^5 CFU/ml) disappeared within 2 hours. After 45 minutes of exposure to 150 mg/ml zeolite, no live cells were discovered in *E. coli*, and the same finding was made in *S. aureus* and *P. aeruginosa* after 60 minutes of treatment. When microorganisms were present, the amount of Ag^+ released from zeolite was more significant than in broth alone, showing that bacteria were absorbing Ag^+.
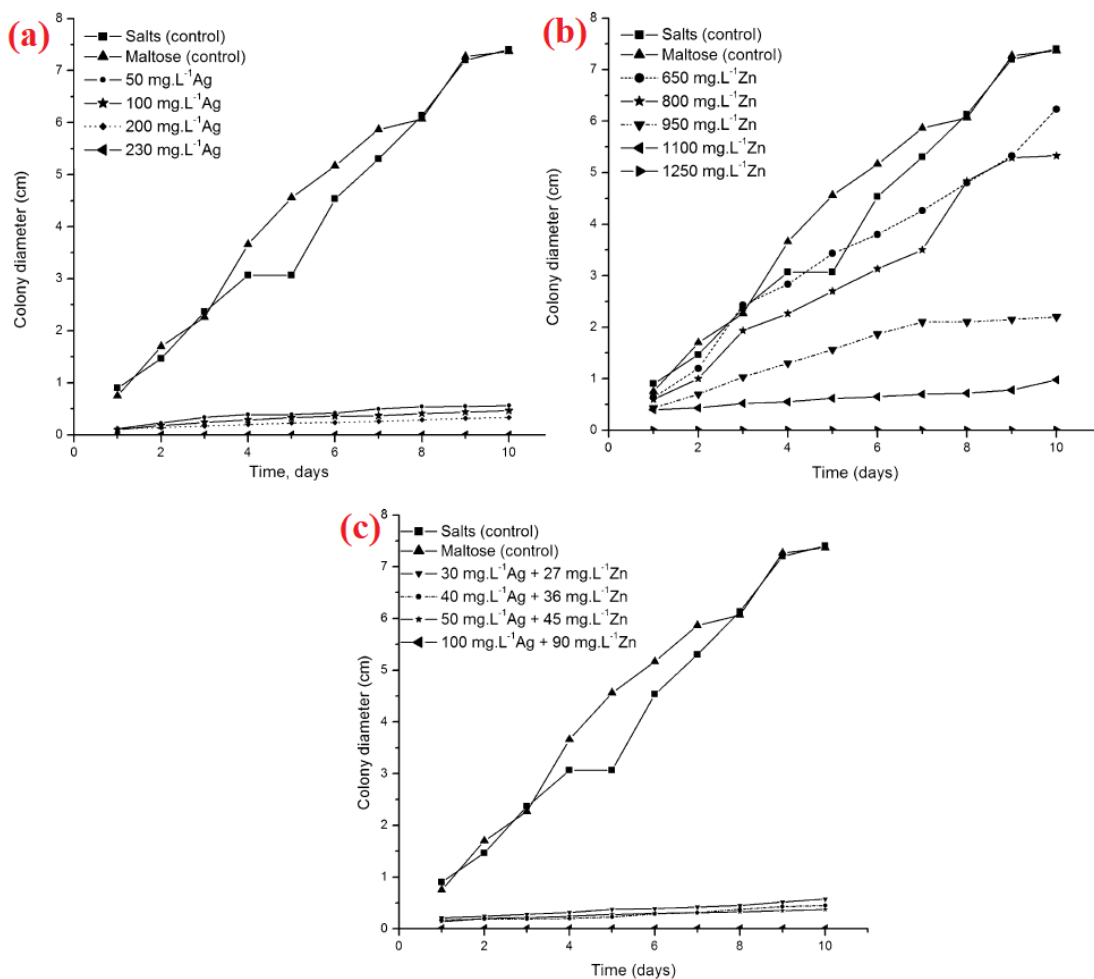
Figure 2. 5. *A. niger* colony growth mean value in an agar medium with several metal-exchanged zeolite concentrations (cm). AgA (a), ZnA (b), and ZnAgA (c) [65].

Another study introduced Ag^+ and Zn^{2+} in the zeolite A in single and binary combinations [65]. Different cation exchanged levels were acquired from zeolite A (NaA), i.e., zeolite A containing Ag^+ (AgA), Zn^{2+} (ZnA), and Ag^+/Zn^{2+} (AgZnA), and their antifungal activities were examined. The minimum inhibitory concentration (MIC) of the exchanged zeolites was evaluated against *Aspergillus niger*. For single exchanged zeolite A, the concentration values of Ag^+ and Zn^{2+} was varying between $50 < [Ag^+] < 1000$ mg/L and $650 < [Zn^{2+}] < 2000$ mg/L. For binary exchanged zeolites,

28

the concentration values of Ag^+ and Zn^{2+} was changing from $30 < [Ag^+] < 250$ mg/L and $50 < [Zn^{2+}] < 400$ mg/L. Figure 2.5. shows the growth inhibition of single and binary exchanged zeolites against *A. niger.* According to Figure 2.5, the binary exchanged zeolite sample with $[Ag^+] = 100$ mg/L and $[Zn^{2+}] = 90$ mg/L exhibits growth inhibition similar to that obtained with single exchanged zeolite of $[Ag^+] = 230$ mg/L. The antifungal activity of these compounds was also tested followed by their addition into waterborne coating formulations. Results show that zeolites of type A supported by Ag^+ and Zn^{2+} can be a valuable tool for producing waterborne coatings with longer microbiological protection than conventional organic biocides [65].

Dutta et al. summarized the silver introduced zeolites [66]. According to this study, closer interaction between silver zeolite and microorganisms enhances antibacterial activity. Smaller zeolite crystals release silver ions more rapidly, and the smaller silver nanoparticle on the zeolite display superior antimicrobial activity. For cell death, yeast requires more silver zeolite than bacteria. Antimicrobial activity is enhanced by surface modification of silver exchanged zeolite, upon introducing positive charge onto the zeolite surface. Under anaerobic conditions, silver zeolites show an antimicrobial effect, however, at a much lower rate. Bacteria with thicker cell walls needed the use of additional silver zeolites. When gram-positive and gram-negative bacteria are exposed to silver-containing zeolites, they undergo different structural modifications. Even after two years of storage, silver-introduced zeolites were shown to exhibit antimicrobial efficacy [66].

In conclusion, a crystalline zeolite host material provides more effective antimicrobial activity due to the durability of antimicrobial efficacy and controlled release.

2.2. Essential Oils

2.2.1. Thymol: the widespread ingredients of Thyme

Among essential oils (EOs), thyme has been the most common one against pest insects. Thyme is a Mediterranean fragrant evergreen shrub, known since ancient times in traditional medicine. The isomers thymol (2-isopropyl-5-methylphenol) and carvacrol (5-isopropyl-2-methylphenol), both derived from the precursor p-cymene, another constituent of T. vulgaris, are the two types of thyme components [67]. Figure 2.6 shows the chemical structure of the thymol molecule.
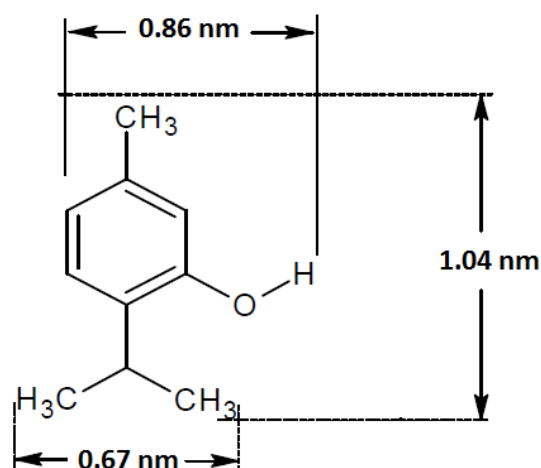
Figure 2. 6. The chemical structure and dimension of thymol molecule [68].

Thymol and its phenol isomer carvacrol have phenolic groups. Hydroxyl groups in the phenolic group disintegrate the outer membrane of gram-negative bacteria containing lipopolysaccharides and proteins. This disintegration leads to leakage of lipopolysaccharides. Hydroxyl constituents also interrupt the plasma membrane, so the proton motive force (PMF) and electron flow [22,69–71]. Figure 2.7 indicates a schematic representation of the antimicrobial activity of thymol.
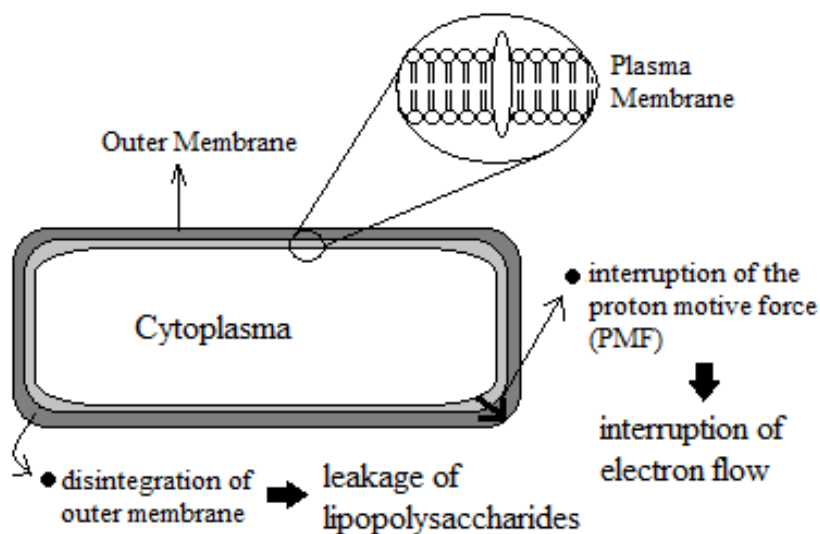
Figure 2. 7. A schematic representation of the antimicrobial activity of thymol.

EO extracts of plants exhibit remarkable antimicrobial antiviral and antioxidant activity; thus, they are proper alternatives to hazardous synthetic antimicrobial agents [72,73]. However, oxidation and volatility are the main drawbacks of utilizing EOs for antimicrobial applications. Encapsulating EOs in a porous structure is an excellent way to overcome these limitations [73]. This process also offers high efficiency and high payload with a controlled release due to protecting the load from surroundings [74].

2.2.2. Encapsulation of Essential Oils

Among the several host materials, β-cyclodextrin is the most popular host material used to retain and preserve bioactive property [68,75–79]. β-cyclodextrin is a non-toxic oligosaccharide containing a hydrophilic outer surface and hydrophobic hollow inner surface [77]. The binding of EO compounds to β-cyclodextrin brings about the complex, depending on guest compound hydrophobicity and molecular geometry [77]. Antibacterial thymol compound was loaded in β-cyclodextrin, and thymol's presence into β-cyclodextrin by forming the complex between the hydrophobic inner surface of

β-cyclodextrin was proved by UV-visible and FTIR analyses in several studies [68,76]. In another study, the inclusion of Lippia gracilis EO into β-cyclodextrin, that is, the formation of the complex was showed with thermogravimetric analysis (TGA) and differential thermal analyses (TDA) [79].
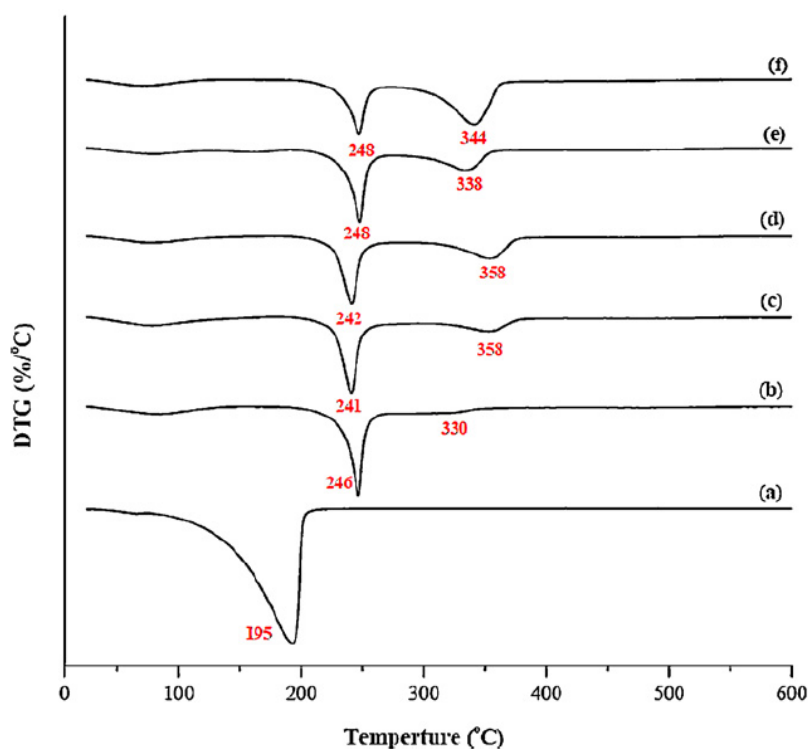
Figure 2. 8. DTG thermograms of (a) oregano essential oil (OEO), (b) chitosan nanoparticles and (c)–(f) OEO-loaded chitosan nanoparticles prepared using different initial weight ratios of chitosan to OEO: (c) 1:0.1, (d) 1:0.2, (e) 1:0.4, and (f) 1:0.8 [80].

Similar to β-cyclodextrin, chitosan was studied as a host material for encapsulating EO such as oregano and Lippia sidoides [80,81]. FTIR analysis was performed to detect the presence of EO in chitosan molecules. TGA-DTG analyses were achieved to determine the thermal stability of the latest product containing

chitosan and EO [80,81]. Figure 2.8 indicates DTG thermograms of the oregano encapsulated chitosan samples. According to Figure 2.8, the presence of new T_d around 340 °C (Figure 2.8 c–f) could be attributed to the T_d of encapsulated oregano EO with an increase in the loading of oregano EO. Moreover, the release of EO depending on time was detected with UV-VIS analysis [80].

In another study, encapsulation enhanced antimicrobial activity was investigated [82]. Thymol and carvacrol were also encapsulated into liposomes. Additionally, the antimicrobial activity assays of pure thymol, pure carvacrol and their encapsulated compounds were achieved. It was concluded that liposome encapsulation enhanced the antimicrobial activity [82].

Moreover, carvacrol was encapsulated into layers of clay galleries to use in active packaging [83,84]. The prepared clay/carvacrol hybrid was developed as active antimicrobial films with low-density polyethylene (LDPE). The results obtained from the (TGA) of clay/carvacrol hybrid samples are shown in Figure 2.9. According to Figure 2.9, carvacrol exhibits one distinct weight loss around 160 °C, attributed to the evaporation of carvacrol. On the other hand, the distinct weight loss was observed to increase up to 200 °C, which was ascribed for the evaporation of carvacrol. Consequently, the authors stated that clay/carvacrol hybrid materials exhibited thermal stability after the high-temperature melting process in polymer production, as shown in Figure 2.9 [83].
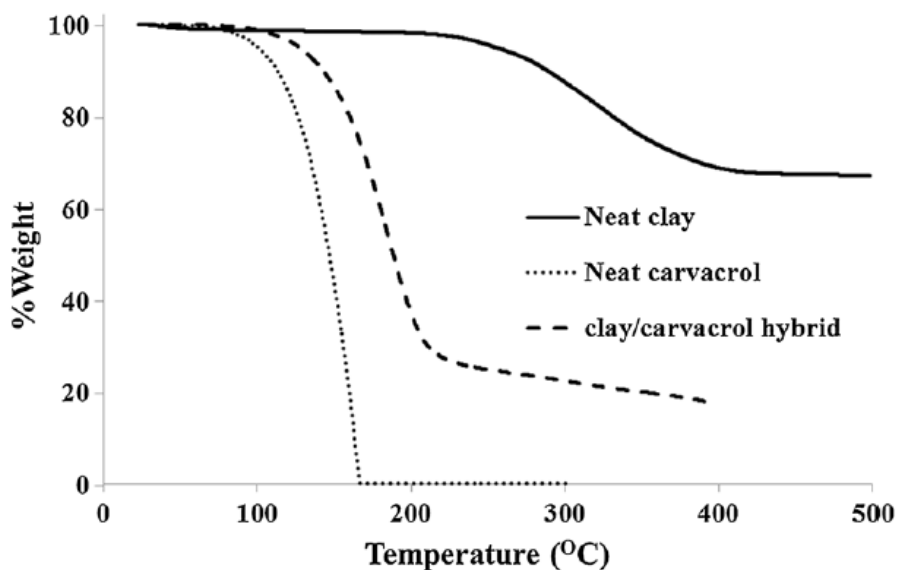
Figure 2. 9. TGA analysis results of clay, carvacrol, and clay/carvacrol hybrid [83].

Thymol and p-cymene were also encapsulated into polylactide microcapsules, and their release study was performed [85]. It was determined that the release of thymol and p-cymene depended on the lipophilic property of media [85]. Also, the release of thymol from zein based films was investigated, and it is stated that the release of thymol was affected by the thickness of layers [86].

Furthermore, fragrances used in detergents, soap, and personal care products were encapsulated in the literature to control their release. Firstly, Procter & Gamble Co patented the encapsulation of fragrances in the zeolite framework [87]. For that purpose, the absorption and desorption kinetics of a fragrance molecule into the zeolite framework called triplal was studied [45].

Similarly, encapsulations of EOs into microporous solids were also studied. It was first patented by Post Harvest Solutions Ltd. [88] for active packing. This invention claimed zeolites, clays, cellulose fibers, silica gel, and aluminum oxide as hosts for

EOs. It was stated that this invention offered release control of EOs from porous solids during more extended periods than pure EOs [88].

In the literature, silica was also used as a host material for encapsulating EOs due to their porous property. Trichloroisocyanuric acid (TCCA), thymol, eugenol, and thymoquinone were encapsulated into porous silica [89,90]. Amorphous silica provided only well-dispersion of TCCA, whereas ordered porous MOFs also led to the controlled release of TCCA [90]. This result indicated that the well-ordered porous property of host materials is essential for the release of EOs. In another silica encapsulation example in the literature, Mattos et al. investigated the antimicrobial activity of thymol encapsulated silica [74]. They performed surface modification for silica before encapsulation of thymol to tailor the release time of thymol from the structure and preserve antimicrobial activity for a long time. Amine and carboxyl groups are bonded into silica, providing a lower release rate and more prolonged antimicrobial activity [74].

It is stated that controlling the release of EOs provides long-term antimicrobial activity [84,89]. In the literature, the encapsulated EOs, such as thymol, carvacrol, and eugenol, exhibited long-term antifungal activity for up to 14 days. In contrast, the same substance in a pure state showed no antifungal activity after a couple of days [89]. In another study, the antimicrobial activity of carvacrol in low-density polyethylene (LDPE) and clay encapsulated carvacrol in low-density polyethylene (LDPE) were compared. It was shown that the antimicrobial activity of carvacrol maintained the antimicrobial activity even after one month through clay encapsulation [84]. Figure 2.10 indicates the antimicrobial activity of LDPE/carvacrol and LDPE/(clay/carvacrol) films against *E. coli*. According to Figure 2.10, the maximum bacterial reduction was obtained using Clay2 encapsulation even after one month.
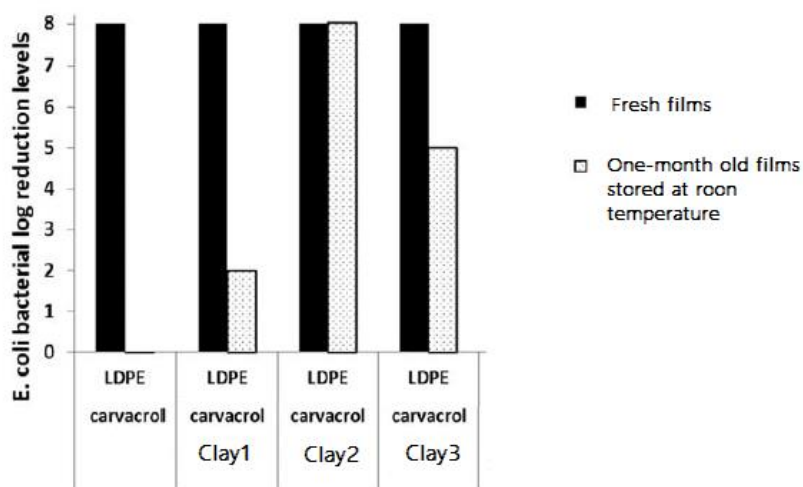
Figure 2. 10. Antimicrobial activity of melt-compounded LDPE/carvacrol and LDPE/(clay/carvacrol) films against *E. coli*. Results are presented for both fresh and a month old films (stored at room temperature) [84].

2.3. Zeolites as Host Materials for Antimicrobial Agents

The use of zeolites and zeo-type materials as host materials is attractive due to their well-defined, uniform pore size and improved chemical, thermal and mechanical properties. Since the channels and pores of zeolites are in the lower range of the nanometer scale, the guest incorporated into zeolites must also be in nanometer scale. The nanometer-scale porosity opens the possibility of selective sorption in zeolites. Different zeolites with pore structures and morphologies can be incorporated with metal nanoparticles and/or metal complexes and organic substances to form host-guest systems with desirable properties [37,45].

2.4. Hierarchical Zeolites/Zeo-type Materials

The encapsulation of organic and organometallic molecules into zeolite framework sites has invited significant attention for many applications. However,

36

diffusion limitations through smaller sized pore structures prevent mass transport. Hierarchical zeolites, containing both micro and mesopores, enhance diffusion access through pore framework systems [91,92]. In order to provide several hierarchical systems as bottom-up routes, there is a need to supply proper active volume and defects in the zeolite framework, which can be achieved by using organic and inorganic structure-directing agents during synthesis[93–96]. On the other hand, top-down routes necessitates removal of framework atoms as a part of post-synthesis treatment for forming hierarchical [97,98]. Figure 2.11 shows the summary of methods for the production of hierarchical zeolites.
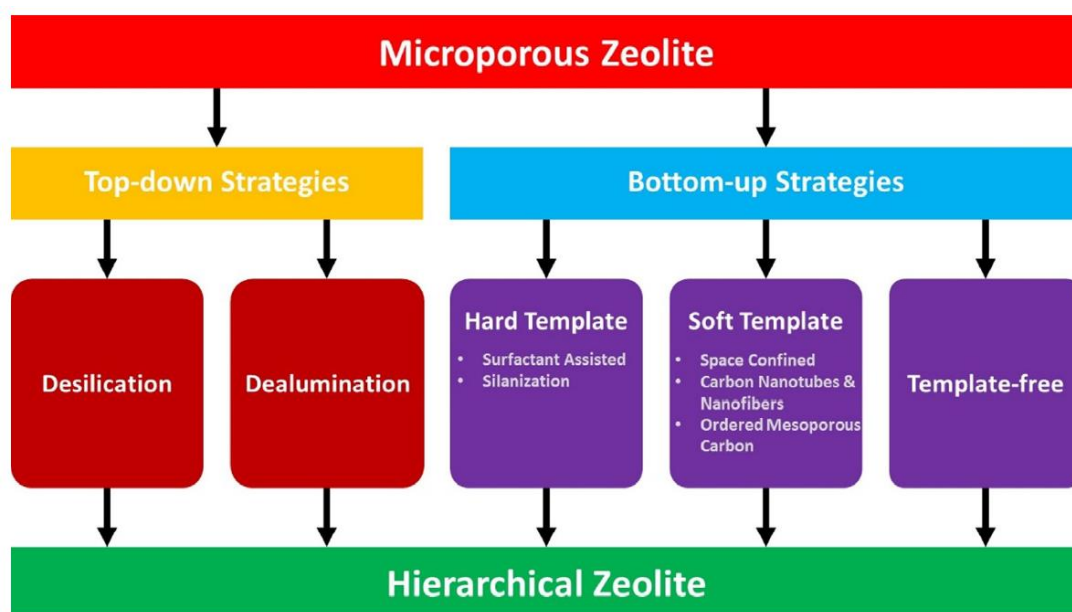
Figure 2. 11. The graphical representation of several hierarchical zeolite creation strategies [92].

2.4.1. Bottom-up Routes

Hard template approaches involve adding solid materials into the zeolite mother gel to behave as mesoporous templates during the zeolite crystal growth. The

prevalent procedures for applying hard template methods consist of three main steps. The first step is adding zeolite precursor gel into the solution of the templates, the second one is aging the zeolite mother liquor with the templates for a predetermined time at low temperature, and the third one is the hydrothermal treatment for crystallization in a standardized environment. The last step is the elimination of the templates by the dissolution or combustion process. During the last years, the application of hard template methods has been examined extensively, and carbonaceous materials are one of the most researched hard templates. Carbonaceous templates are most useful for their structural variety, chemical inertness, and ease of removal. However, their disadvantages, such as hydrophobicity, limit their applicability [92].

Soft templates have also been used for the production of hierarchical zeolites or zeolitic materials. The two most widespread and significant soft templates are surfactants and polymers. Silylane cationic polymers, silanized zeolitic seeds, organosilanes, and amphiphilic organosilanes are the new generation soft templates that are efficient in creating secondary porosity into the zeolite framework [92].

Hierarchical zeolites can also be produced without the use of templates. Several strategies emphasize template-free techniques. One of the most common techniques is intercrystallinity formed upon aggregation of crytals [99]. Although, nanocrystal aggregation and self-assembly are extensively employed for forming zeolites with intercrystalline mesoporosity, the produced zeolites are usually structurally unstable due to the tight agglomeration among the nanocrystals [100]. Another method is the use of rotating zeolite intergrowths to produce self-pillaged MFI nanosheets resulting in mesoporosity [101]. This template-free method is facile and effective. The drawback of this process is that organic molecules are generally difficult to obtain, and post-treatment is needed for organic molecule removal [92].

Due to high cost, unavailable templates, and handicapped purification for removal of the template after synthesis, the bottom-up routes generally are not adapted for their use in industrial-scale [102]. However, post-synthesis treatments containing steam, acid, and alkaline treatments are more prone to industrialization [102–104]. For this reason, in this study, implementing post-synthetic routes was preferred for obtaining hierarchical zeolites and thus defect formation instead of the bottom-up methods.

2.4.2. Top-Down Routes

Dealumination and desilication are the main techniques for top-down routes in order to form hierarchical zeolites. Dealumination has been recognized as one of the most efficient demetallization processes. This process was initially employed to improve the zeolite Si/Al ratio to achieve a stable structure; however, some random mesopores were seen to be generated. Steaming, acid leaching and calcination are three methods causing hydrolyzation of Al-O-Si bonds in the zeolite structure [92].

The steaming technique is usually performed above 500 ℃, breaking Al-O-Si bonds. The breaking bonds brought about the loss of aluminum, which then caused the formation of defects in the zeolite structure. The transfer of less stable silicon to aluminum sites leads to the creation of the domains of silanol rich spots. The procedure described can repair part of the amorphous structure and generate several mesopores [103]. A calcination procedure can also be used to induce dealumination. Zeolite Beta was subjected to steam treatment at 500°C and calcination at 750°C. The Lewis acid sites were shown to increase at the expense of Brønsted acid sites [105]. Acid leaching could be used as a suitable approach to eliminate aluminum from a zeolite structure. After steaming or heat treatment, weak acids are commonly employed to remove debris. However, the presence of concentrated aqueous acids alone also stimulates breakage of Si-O-Al bonds, resulting in aluminum species extraction from the zeolite network and mesopore production [92].

Although dealumination is used to form hierarchical porosity in zeolites, aluminum extraction decreases the acidity of the zeolites. Furthermore, the mesopores generated with this approach usually have a very wide range of size distribution. Some of them are produced within the zeolite structure and are not connected to the exterior surface. Therefore, they do not contribute to enhancing mass transfer.

Desilication has been used extensively on a wide range of zeolites, including FAU, MFI, BEA, CHA, IFR, MTW, MOR, AST, FER, TON, and TUN [92]. The most common desilication method is to treat zeolite samples with NaOH solution [98,106]. Nevertheless, different varieties of zeolites were shown to display distinct properties under the same desilication treatment conditions. Although alkaline treatment of zeolites could produce mesoporosity, mesopore formation unavoidably reduced the micropore system [107]. A later investigation by the same group discovered that both silica and alumina were taken away from the zeolite framework and far less aluminum was extracted in alkaline environment compared to silicon [98]. The majority of silicon atoms dissolved from the exterior surface, preserving the zeolite's crystallinity. The morphological changes induced in ZSM-5 crystals caused by alkaline treatment under various conditions, such as varying periods and concentrations, are depicted in Figure 2.12. According to Figure 2.12, defects on the outer surface of the zeolite were created after alkaline treatment. A test reaction for cumene cracking showed an improvement in catalytic performance. This improvement can be explained by increased diffusivity due to generated mesopores [98]. The presence of neighboring aluminum species in the framework was discovered to restrict silicon extraction. Thus, the Si/Al ratio of the original zeolite is a critical parameter to manage Si-O-Si bonds in mesoporosity formation [92]. It was concluded that the Si/Al ratio of 50 was ideal for creating mesoporous structures through alkaline treatment while conserving zeolite crystallinity [108].
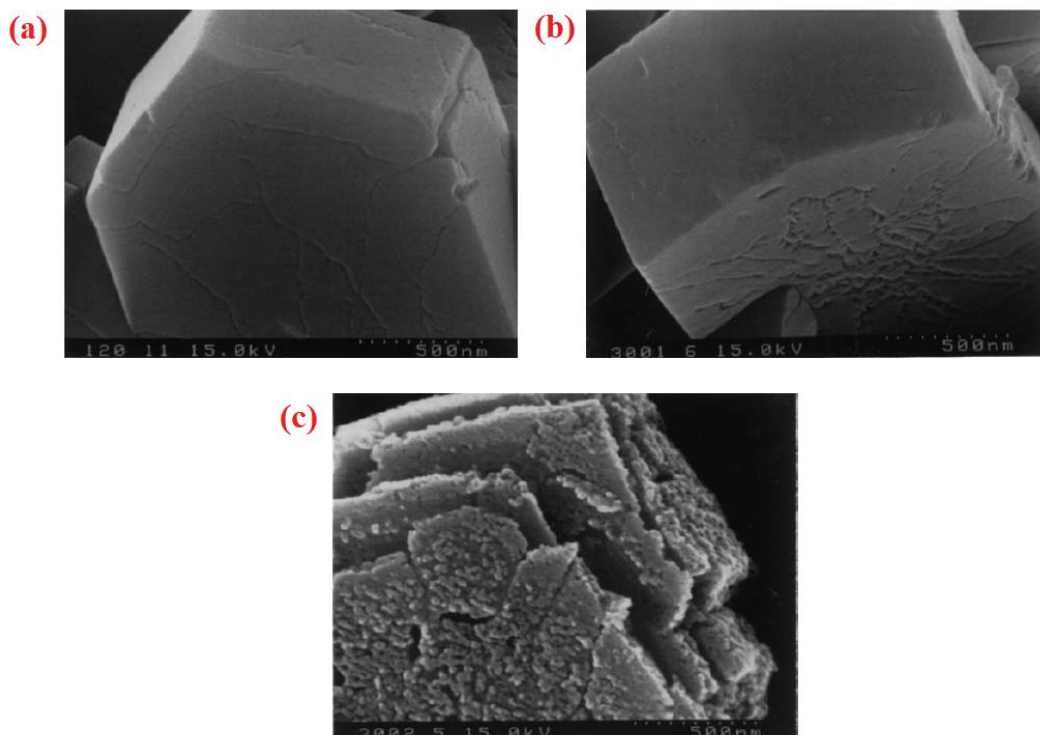
Figure 2. 12. SEM images of NaOH solution treated ZSM-5. Treatments were performed with 0.1M NaOH solution at 338K for 120 min (a), 0.1M NaOH solution at 338K for 300 min (b), and 0.2M NaOH solution at 353K for 300 min (c) [98].

Groen et al. revealed that zeolite beta was prone to significant silicon extraction and mesoporosity formation due to the weaker stability of aluminum in its structure than mordenite and ZSM-5. However, it also had high microporosity and loss in crystallinity [109].

Desilication of ZSM-5 in aqueous solutions of organic hydroxides was shown to result in hierarchical zeolites containing both microporosity and mesoporosity [110]. In this research, TPAOH and TBAOH were applied as organic hydroxides. Due to its minor reactivity of organic bases with silicon, the use of organic base allowed a significant control over the desilication process compared with the rapid silicone leaching process using NaOH. Moreover, using organic hydroxides were shown to

deliver proton directly into the mesoporous structure without the need of ion-exchange with NH_4NO_3. According to Tsai and his coworkers, an increase in the surface area of TS-1 was observed with TPAOH post-treatment with no remarkable change in the pore structure. On the other hand, NaOH lead to a modification in the pore structure of TS-1 and promoted the formation of mesopores [111].

Furthermore, it is possible to use this method for zeolites with greater Si/Al ratios due to low organic hydroxide selectivity in silicon extraction [110]. Peréz-Ramírez and et al. reported a modified process of desilication to generate hierarchical zeolites with no severe losses in microporous volume. NaOH was added as the pore development moderator in this study, while TPA^+ or TBA^+ organic cations were introduced. This new technique exhibited better transport and higher catalytic activity in the hierarchical zeolites [112].

The combination of several alkalines and salt compounds was performed as post-treatment for LTA type zeolites. Different pore volumes and external surface areas were obtained depending on the concentration and type of chemicals [113]. Verboekend and his coworkers treated zeolite A with several combinations of aqueous KCl, NH_4Cl, Na_2H_2EDTA, and $NaNO_3$ solutions. Subsequent ion exchange of KCl and NH_4Cl increased external surface area slightly (from 2 m^2/g to 3 m^2/g). However, after these subsequent ion exchange processes, another subsequent acid washing with Na_2H_2EDTA enhanced the external surface area to 62 m^2/g [113]. Table 2.1 shows the summary of textural properties of the parent and post-synthesis treated zeolites in the literature.

Table 2. 1. The summary of textural properties of the parent and treated zeolites.

Authors	Zeolite type	Chemical	V_{pore} (m^3/g) (before)	V_{pore} (m^3/g) (after)	V_{micro} (m^3/g) (before)	V_{micro} (m^3/g) (after)	V_{meso} (m^3/g) (before)	V_{meso} (m^3/g) (after)	S_{total} (m^2/g) (before)	S_{total} (m^2/g) (after)	S_{ext} (m^2/g) (before)	S_{ext} (m^2/g) (after)
Verboekend (2012)[114]	Zeolite Y	H$_4$EDTA	0.34	0.34	0.30	0.29					22	40
Verboekend (2012)[114]	Zeolite Y	H$_4$EDTA+NaOH	0.34	0.41	0.3	0.28					22	123
Verboekend (2012)[114]	Zeolite Y	H$_4$EDTA+NaOH+ Na$_2$H$_2$EDTA	0.34	0.47	0.3	0.23					22	223
Verboekend (2013)[113]	Zeolite X	NaOH	0.26	0.29	0.23	0.23	0.03	0.06			22	26
Verboekend (2013)[113]	Zeolite X	Na$_2$H$_2$EDTA	0.26	0.31	0.23	0.27	0.03	0.04			22	31
Verboekend (2013)[113]	Zeolite X	KCl+NH$_4$Cl	0.26	0.22	0.23	0.13	0.03	0.09			22	75
Verboekend (2013)[113]	Zeolite X	KCl+ NH$_4$Cl + NaOH	0.26	0.34	0.23	0.26	0.03	0.08			22	53
Verboekend (2013)[113]	Zeolite X	KCl+ NH$_4$Cl + Na$_2$H$_2$EDTA	0.26	0.45	0.23	0.26	0.03	0.19			22	122
Verboekend (2013)[113]	Zeolite X	NaNO$_3$+CsOAc	0.26	0.23	0.23	0.21	0.03	0.02			22	15

Table 2.1. Continued.

Authors	Zeolite type	Chemical	V_{pore} (m³/g) (before)	V_{pore} (m³/g) (after)	V_{micro} (m³/g) (before)	V_{micro} (m³/g) (after)	V_{meso} (m³/g) (before)	V_{meso} (m³/g) (after)	S_{total} (m²/g) (before)	S_{total} (m²/g) (after)	S_{ext} (m²/g) (before)	S_{ext} (m²/g) (after)
Verboekend (2013) [113]	Zeolite X	KCl+ NH$_4$Cl + Na$_2$H$_2$EDTA + NaNO$_3$+ CsOAc	0.26	0.39	0.23	0.13	0.03	0.26			22	95
Verboekend (2013) [113]	Zeolite A	KCl+ NH$_4$Cl	0	0	0	0	0	0			2	3
Verboekend (2013) [113]	Zeolite A	KCl+ NH$_4$Cl + Na$_2$H$_2$EDTA	0	0.14	0	0.01	0	0.13			2	62
Verboekend (2013) [113]	Zeolite A	NaNO$_3$+ CsOAc	0	0	0	0	0	0			2	1
Verboekend (2013) [113]	Zeolite A	KCl+ NH$_4$Cl + Na$_2$H$_2$EDTA + NaNO$_3$+ CsOAc	0	0.12	0	0	0	0.12			2	59
Groen (2008) [109]	Zeolite Beta	NaOH	0.31	0.52	0.22	0.1			615	705	60	370
Abello (2009) [110]	ZSM-5 (Si/Al=42)	TBAOH	0.28	0.38	0.17	0.15	0.11	0.23			60	150
Abello (2009) [110]	ZSM-5 (Si/Al=42)	TPAOH	0.28	0.29-0.59	0.17	0.17-0.13	0.11	0.12-0.46			60	80-180
Perez-Ramirez (2009) [112]	ZSM-5	TPA$^+$ + NAOH	0.25	0.51-0.57	0.17	0.09-0.14	0.08	0.37-0.48				

Table 2.1. Continued.

Authors	Zeolite type	Chemical	V_{pore} (m^3/g) (before)	V_{pore} (m^3/g) (after)	V_{micro} (m^3/g) (before)	V_{micro} (m^3/g) (after)	V_{meso} (m^3/g) (before)	V_{meso} (m^3/g) (after)	S_{total} (m^2/g) (before)	S_{total} (m^2/g) (after)	S_{ext} (m^2/g) (before)	S_{ext} (m^2/g) (after)
Tsai (2010) [111]	TS1	TPAOH					74	69	546.2	423	341	261
Tsai (2010) [111]	TS1	NAOH					74	98	546.2	507	341	230
Groen (2004) [108]	MFI (Si/Al=17)	NaOH			0.15	0.14	0.1	0.24	415	410	40	65
Groen (2004) [108]	MFI (Si/Al=37)	NaOH			0.17	0.13	0.09	0.55	430	505	40	180
Groen (2004) [108]	MFI (Si/Al=1008)	NaOH			0.16	0.15	0.03	0.15	390	440	15	80
Thibault-Starzyk (2009) [106]	ZSM-5	NaOH	0.28	0.57	0.17	0.09			449	510	58	227
Ogura (2000) [107]	NH$_4$-ZSM-5	NaOH			0.171	0.133	0.072	0.279				
Ogura (2001) [98]	ZSM-5	NaOH			0.18	0.13	0.15	0.28	303	320	6.63	115.4
Goa (2004) [115]	ETS-10	HCl							367	355		
Lv (2007) [116]	ETS-10	HF							290	279		
Lv (2007) [116]	ETS-10	HNO$_3$							290	350		
Lv (2007) [116]	ETS-10	H$_3$PO$_4$							290	317		
Lv (2007) [116]	ETS-10	citric acid							290	323		
Pavel (2006) [117]	ETS-10	H$_2$O$_2$			0.1558	0.1598						
Xamena (2003) [118]	ETS-10	HF									21	27-30

2.4.2.1. Post-synthesis Treatment of ETS-10

For zeo-type materials such as ETS-10, the acidic and peroxidic medium were preferred as post-treatment techniques compared to alkaline treatments [115–118]. Llabréz I Xamena and his coworkers showed that aqueous mild HF solution resulted in silicon leaching from the structure with enhanced photocatalytic activity in degradation of aromatic molecules [118]. Lv et al. studied nitric, fluoric, phosphoric, and citric acid to leach titanium species from the TiO_6 chains in the ETS-10 framework and concluded that the alteration of alkali cations by protons changed the structure of ETS-10 [116].
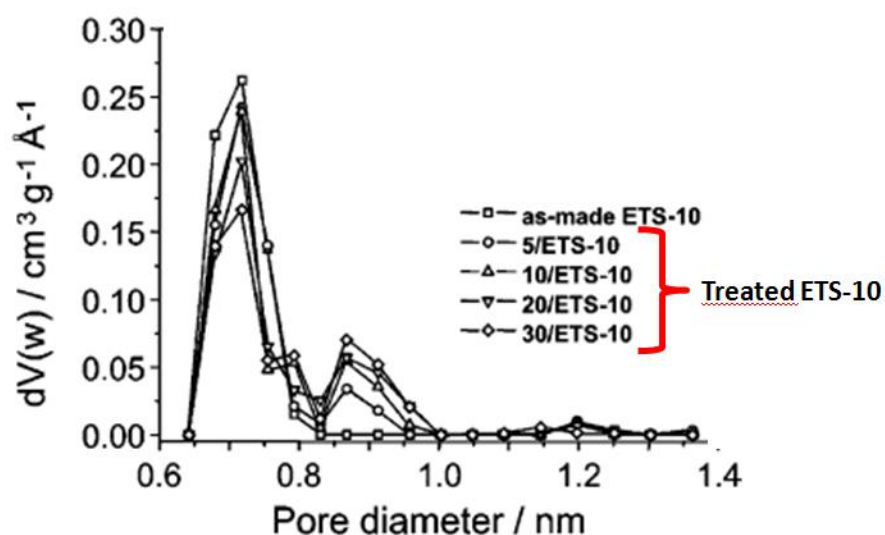
Figure 2. 13. NLDFT pore size distributions of as-synthesized and H_2O_2 treated ETS-10 [117].

Another chemical used to leach titanium species from the ETS-10 structure was aqueous hydrogen peroxide solution (i.e., H_2O_2). H_2O_2 lead to numerous defects depending on the concentration and exposure time [117]. Figure 2.13 indicates the pore size distribution of as-synthesized and treated ETS-10 crystals, treated using three different aqueous H_2O_2 solutions, i.e., 10, 20, and 30 wt.%. The H_2O_2 post-treatment led to a bimodal micropore size distribution in ETS-10 samples. The formation of

supermicropores can explain this situation due to leaching titanium units from the ETS-10 structure.

2.4.2.2. Post-synthesis Treatments of Zeolites X

The removal of aluminum from the structure of FAU type structure by reaction of ethylenediaminetetraacetic acid (EDTA) compounds lead to an increase in the external area of zeolite [102,103,113,114]. Zeolite Y was employed for aqueous H_4EDTA solutions as it maintains a greater crystallinity than mineral acids [119]. Treatment with aqueous H_4EDTA solutions resulted in progressive yield losses (fall to 70% for the concentration of 0.2 M), whereas crystallinity dropped dramatically (fall to *ca.* 20% for the concentration of 0.2 M) as illustrated in Figure 2.14-a [35]. Aqueous Na_2H_2EDTA treatment had been utilized to extract excess frame Al from the steamed zeolites of USY [35,119]. Ideally, it should minimally impact the parent crystals. According to Figure 2.14-b, the crystallinity of zeolite Y increased to 104%, indicating that some amorphous species were removed [35].
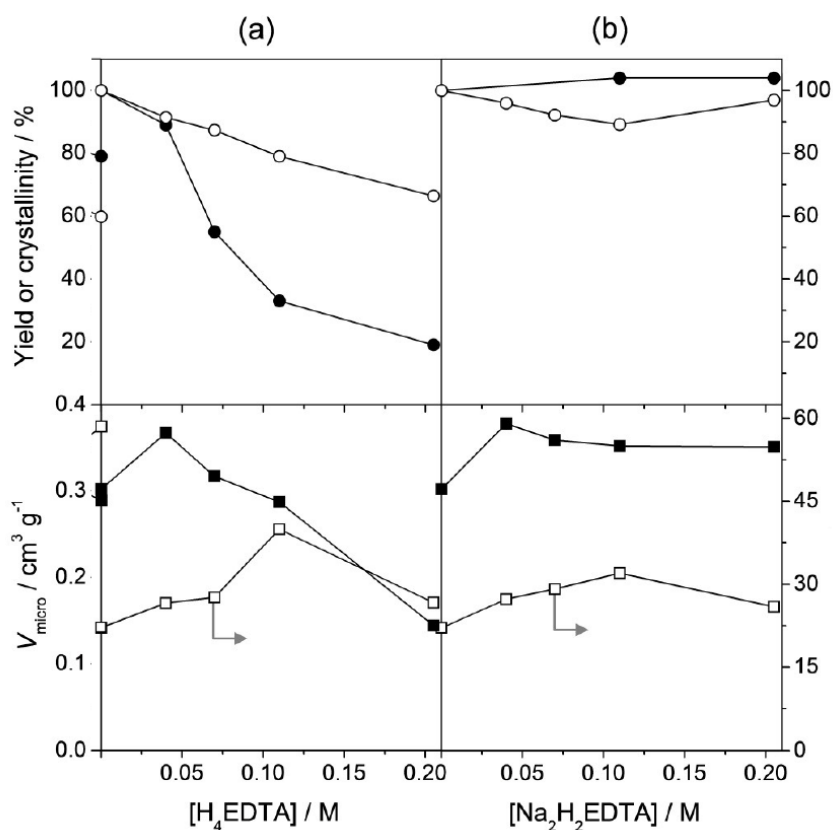
Figure 2. 14. The effect of aqueous H₄EDTA (a) and Na₂H₂EDTA (b) on crystallinity (solid circles), yield (open circles), micropore volume (solid squares), and mesopore surface area (open squares) of the Y zeolites. The parent Y zeolite is denoted at 0 M [35].

A moderate dealumination treatment with H₄EDTA can overcome the strong framework stability of zeolite Y in alkaline conditions. Desilication in NaOH and acid washing in aqueous Na₂H₂EDTA allowed the formation of mesopores. On the other hand, similar dealumination of zeolite X , is difficult to produce without introducing massive structural damage [35,114]. However, partial amorphization followed by sequential removal of the resultant material provides an alternative method to create hierarchical zeolite X by post-synthetic approach. Verboekend performed ion-exchange using KCl followed by NH₄Cl treatment with zeolite X [35]. Subsequent alkaline treatment of this zeolite (i.e., NaOH) led to a considerably low yield.

48

Moreover, subsequent aqueous Na_2H_2EDTA as a mild acid treatment offered mesopore creation after ion exchange of KCl followed by NH_4Cl. In contrast to alkaline treatment, changing the amount of Na_2H_2EDTA solution showed to be more efficient in enhancing treatment efficiency [35]. Verboekend prepared mesoporous zeolite X crystals with four time ion exchange using KCl and NH_4Cl, followed by subsequent aqueous Na_2H_2EDTA treatment. Figure 2.15 shows the SEM images of conventional and hierarchical X produced based on this process [113].
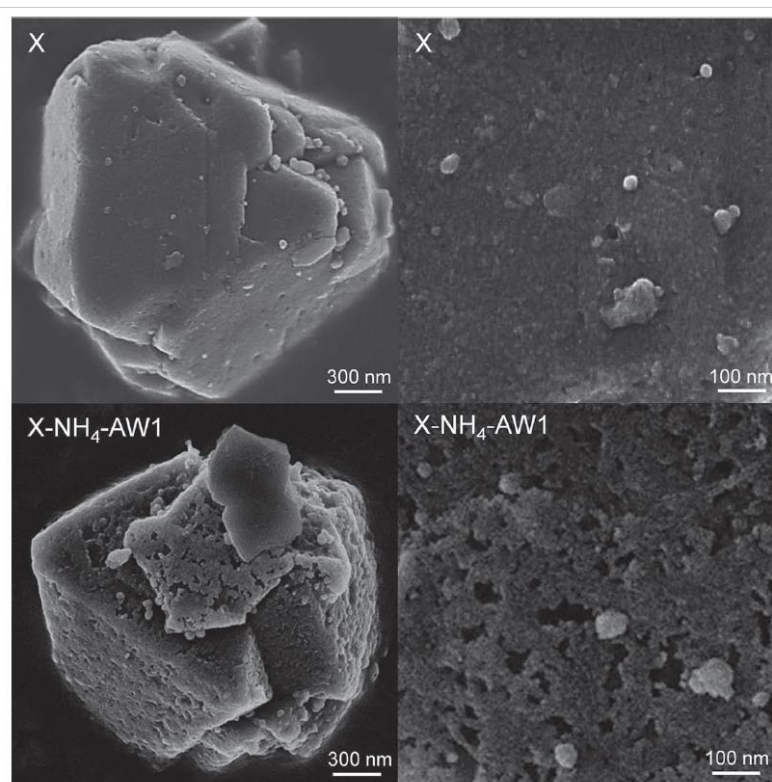
Figure 2. 15. SEM images of conventional and hierarchical X. X-NH$_4$-AW1 indicate ion exchange of KCl four times and followed by NH4Cl four times, then subsequent aqueous Na_2H_2EDTA treatment [113].

2.5. Goals and Objectives

Goals:

The main goal of this thesis is the development of sustainable and environmentally friendly antimicrobial compounds with high potential to be used in the industry based on zeolitic frameworks. Specifically, this will be investigated using two approaches: First, utilizing transition group metals, and second, exploring thymol molecules as their alternatives to obtain antibacterial behavior. The whole work was arranged based on three main chapters, as illustrated in Figure 2.16. The objectives to attain this goal are as follows:

Objectives:

- Preparation of silver/zinc (Ag^+/Zn^{2+}) exchanged zeolite ready to be used in the electrostatic powder paint industry,
  - ✓ To synthesize zeolite A from local kaolin sources at a low cost without impurity,
  - ✓ To perform binary silver and zinc ion-exchange process to obtain antimicrobial zeolite A crystals,
  - ✓ To investigate silver and zinc exchanged zeolite A crystals as an antibacterial additive for electrostatic powder paint in the industry,
- To develop novel antimicrobial ETS-10 crystals,
  - ✓ To synthesize titanosilicate ETS-10 without impurity,
  - ✓ To apply post-synthesis treatments to create defects and so to enlarge micropores into the ETS-10 framework,
  - ✓ To examine the adsorption of thymol molecules in post-treated ETS-10 crystals and investigate adsorption kinetics of thymol,
  - ✓ To explore the antibacterial activities of thymol encapsulated post-treated ETS-10 crystals,
- To create thymol and zinc cation incorporated post-treated zeolite X,

✓ To achieve post-treatment techniques to generate enlarged pore structure in the framework of commercial zeolite X crystals,

✓ To perform zinc ion-exchange process,

✓ To encapsulate thymol molecules into zinc exchanged post-treated zeolite X crystals and examine adsorption kinetics of thymol,

✓ To discover the antibacterial activities of thymol and zinc incorporated post-treated zeolite X crystals.
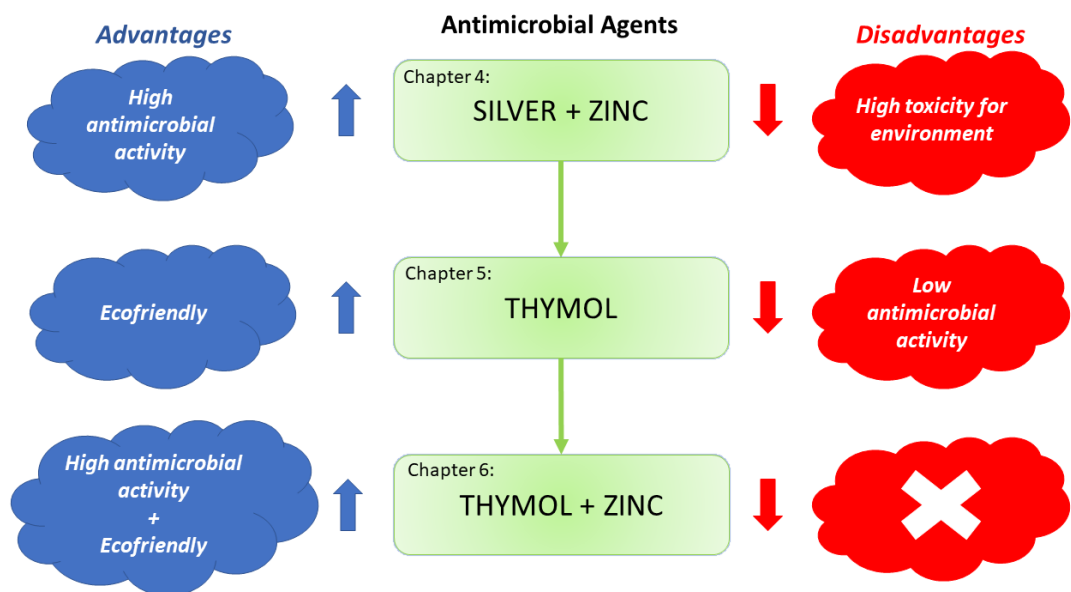
Figure 2. 16. The flow chart of usage of antimicrobial agents in the chapters of this thesis.

CHAPTER 3

EXPERIMENTAL PROCEDURES

3.1. Zeolites

For zeolite A synthesis, Balıkesir Kaolin was used as the main silica and alumina source for zeolite synthesis. Sodium hydroxide (Sigma-Aldrich, anhydrous pellets) and sodium silicate solution (Sigma-Aldrich, 26.5% SiO_2) was used to generate the desired gels.

The chemicals; TiO_2 (P25, 76 wt. % anatase and 24 wt. % rutile, Degussa) and $NaSiO_2$ were obtained from Sigma-Aldrich. NaCl (99.0%), KCl (99.0%), and H_2SO_4 (96.5%) were received from J.T. Baker for the synthesis of ETS-10.

Commercial zeolite 13X was purchased from Sigma-Aldrich.

3.1.1. Synthesis of Zeolite A

Zeolite A crystals were synthesized from a recipe of Du et al. [120]. Kaolin was calcined at 800 °C for 1.5 h to obtain active metakaolin. The resulting metakaolin was mixed with the proper amount of sodium hydroxide, distilled water, and, if needed, sodium silicate solution to generate the desired gel formulas shown in Table 3.1. The resulting gel was stirred at 500 rpm for four h in a water bath at 60 °C. Aged gels were placed in an oven where hydrothermal synthesis was carried out at 100 °C for four h in static conditions in a sealed HDPE bottle. The molar gel composition was optimized to obtain high crystallinity from reaction mixtures of the following compositions: 2.44 SiO_2:1 Al_2O_3:a Na_2O:b H_2O (a = 3.14-4.7 and b = 110-220). The resulting crystals

were centrifuged, washed with deionized water 3-4 times, and dried at 60 °C. The most crystalline product to be used in antibacterial studies was denoted as sample NaA.

Table 3. 1. Zeolite A gel parameters.

Sample Code	SiO_2/Al_2O_3	Na_2O/SiO_2	H_2O/SiO_2
A0-1	2.44	1.29	45
A0-2	2.44	1.29	90
A0-3	2.44	1.93	45
A0-4	2.44	1.93	90

3.1.2. Synthesis of Engelhard Titanosilicate ETS-10

Engelhard Titanosilicate ETS-10 crystals were synthesized using the gel composition 3.4 Na2O: 1.5 K2O: TiO2: 5.5 SiO2: 150 H2O [76]. 1.62 g sodium chloride and 2.48 g potassium chloride were dissolved in 14.14 g deionized water for the synthesis. 13.09 g sodium silicate was added to the aqueous salt solution in a high-density polyethylene bottle (HDPE) and hand-shaken for 5 min, forming the Si precursor solution. For the formation of Ti source, 0.88 g commercial TiO_2 (P25) was added into an aqueous solution of a sulfuric acid solution prepared by mixing 0.75 g sulfuric acid with 7.07 g deionized water. The solution was hand-shaken vigorously for 5 min. The resulting white, viscous solution was obtained by pouring the Ti precursor solution into the Si precursor solution and hand-shaken for 5 min. After measuring the pH of the solution (pH =10.6-10.8) using a Hanna 2211 pH/ORP meter, the gel was introduced into 10 mL Teflon-lined stainless steel autoclaves for 72 hours at 503 K. After the synthesis, the crystals were cooled at room temperature, centrifuged, and washed with deionized water several times and lastly dried for a day at 323 K.

3.2. Formation of Engineered Zeolites/Zeo-type Materials

Aqueous H_2O_2 solution (wt. %50 in H_2O) was purchased from Sigma-Aldrich for the post-synthesis treatments of ETS-10 crystals.

For the production of hierarchical zeolite from commercial zeolite 13X, KCl (99+%, ACS reagent) was received from ACROS Organics, and NH_4Cl (for analysis EMSURE® ACS, ISO, Reag. Ph Eur) and Na_2H_2EDTA (Titriplex® III) were obtained from Merck.

3.2.1. Post-Synthesis Treatments of ETS-10 crystals

In order to create defects in the ETS-10 framework and enlarge the channels, 1 gr of as-synthesized ETS-10 crystals were subjected to 100 mL of 10 wt.% aqueous H_2O_2 solutions for 10 minutes and also 30 wt.% aqueous H_2O_2 solutions for 30 minutes at room temperature [117]. The treated crystals were washed, centrifuged three times with deionized water, and dried overnight in an oven at 323 K. The products were labeled with the conditions of hydrogen peroxide treatment. The sample notations are ETS for as-synthesized ETS-10, 10-ETS for the sample treated 10 wt.% aqueous H_2O_2 for 10 min, and 30-ETS for the sample treated 30 wt.% aqueous H_2O_2 for 30 min.

3.2.2. Post-Synthesis Treatments of Zeolite X

Hierarchical zeolite X crystals were produced in three consecutive steps, listed in Table 3.2. The process is adapted from the study of Verboekend et al. [113]. The treatments were achieved under magnetic stirring using beakers. After each step, the formed crystals were cooled at room temperature, centrifuged, washed with deionized water three times, dried for a day at 323 K, and then used for the next step.

Table 3. 2. The list of chemical treatments for the production of hierarchical zeolite X.

# of steps	Chemical	Amount of zeolite (gr)	Volume of the solution (ml)	Concentration of the solution (M)	Time (h)	Temperature (°C)
1	KCl	10	130	3	2	65
2	NH$_4$Cl	10	500	3	2	65
3	Na$_2$H$_2$EDTA	1	62.5	0.11	6	100

3.3. Encapsulation of Antibacterial Agents into Zeolite Framework

The encapsulation methods of antimicrobial agents have been performed in two different ways depending on the molecular structure of the antimicrobial agent. The ion-exchange process achieved the encapsulation of the transition metal cations, i.e., Ag^+ and Zn^{2+}. In comparison, thymol molecules are encapsulated by physical adsorption.

3.3.1. Ion-exchanged Zeolites

Silver nitrate (AgNO$_3$) and zinc sulfate heptahydrate (ZnSO$_4$.6H$_2$O) that were used for ion exchange processes were purchased from Sigma-Aldrich and Merck, respectively. The ion-exchange procedure used in this thesis is illustrated in Figure 3.1.

56
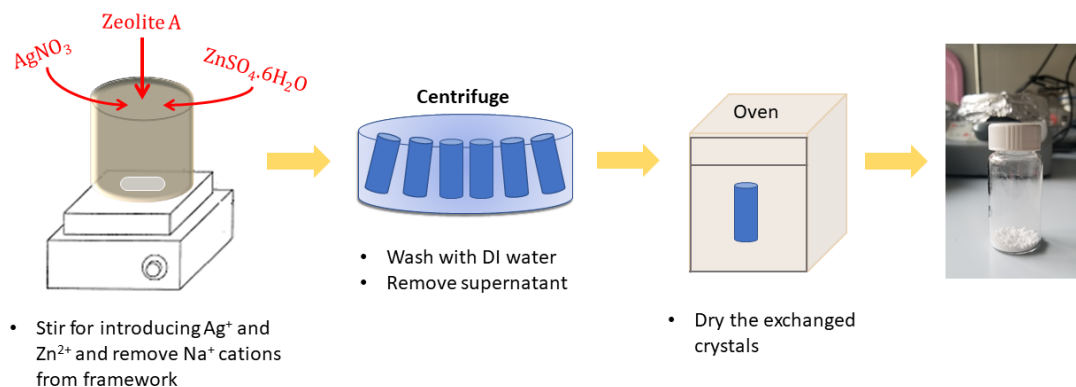
Figure 3. 1. The ion-exchange procedure of cation exchanged zeolites.

In chapter 4, silver (Ag^+) and silver/zinc (Ag^+/Zn^{2+}) exchanged zeolite A crystals were prepared by adding 10 g as-synthesized zeolite A crystals into 200 mL aqueous $AgNO_3$ or $AgNO_3$-$ZnSO_4.6H_2O$ solution with varying concentrations from 2.3 mM to 23.7 mM. The solutions were magnetically stirred for 24 h in a dark environment. Ion-exchanged zeolites were centrifuged (7500 rpm for 4 min). The samples were repeatedly washed with excessive deionized water after that they were dried at 45 °C for approximately 24 h. For the materials with silver, precautions were taken due to the light sensitivity of silver. The prepared silver (Ag^+) and silver/zinc (Ag^+/Zn^{2+}) exchanged zeolite A crystals were denoted as "mAgnZn", where "m" and "n" indicate the calculated Ag^+ and Zn^{2+} loading amount by weight, respectively. Also, as-synthesized zeolite A was named "NaA".

In chapter 6, the ion-exchange aqueous solutions of $ZnSO_4.6H_2O$ were prepared for commercial zeolite X, and hierarchical zeolite X. 1 gr of zeolite was added to these $ZnSO_4.6H_2O$ solutions separately and stirred for 24 h at room temperature. The detailed parameters are listed in Table 3.3. In this chapter, commercial zeolite X, post-treated zeolite X, and the ion-exchanged forms of these zeolites are denoted as X, TX, ZnX, and ZnTX, respectively.

Table 3. 3. The ion-exchange parameters for chapter 6.

Sample	Concentration of ion-exchange solution (M)	Amount of ion-exchange solution (mL)	Time of ion-exchange (h)
X	0.032	30	24
TX	0.1	30	24

3.3.2. Thymol Loading into Zeolites

In this thesis, thymol ($\geq 98.5\%$) was purchased from Sigma-Aldrich. As the adsorption experiment, 500 mg of as-synthesized and post-treated zeolites and 1000 mg of thymol were transferred into each separate glass petri dish. These petri dishes were then placed in a closed glass vessel and kept there for adsorption for two weeks for ETS-10 crystals and three months for zeolite X crystals. The percent encapsulation of each sample was calculated with three separate petri dishes with a standard deviation. The percent encapsulation of each sample was calculated from Eq. (1) [121];

$$\% \, Encapsulation = \frac{weight \, of \, thymol \, (m_{THY})}{weight \, of \, zeolite \, (m_{zeo})} \times 100 \qquad (1)$$

Where m_{zeo} is the weight of ETS-10 before placing the desiccator and m_{THY} is the weight difference of ETS-10 crystals before and after placing the desiccator.

3.4. Preparation of Paint Coatings

In chapter 4, Ag^+/Zn^{2+} exchanged zeolite A crystals were used for the production of antimicrobial electrostatic powder paint. The procedure of this chapter is presented in Figure 3.2.
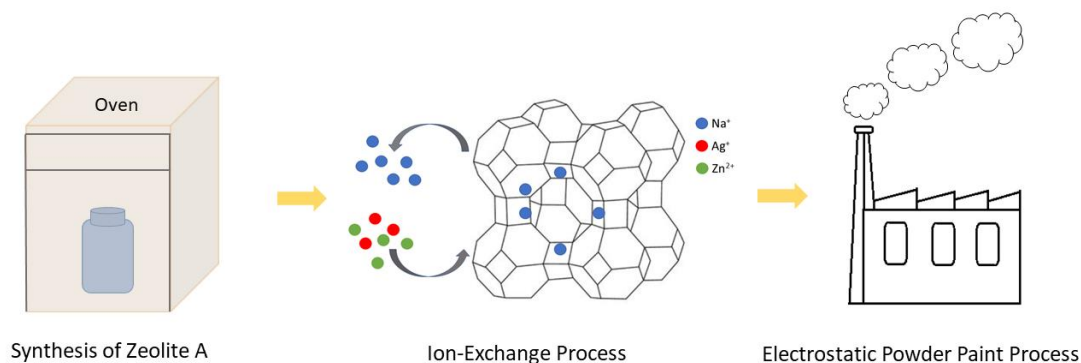
Figure 3. 2. The procedure of paint containing Ag^+/Zn^{2+} exchanged zeolite A.

Thermosetting paint coatings based on epoxy and polyester resins and metal-exchanged zeolite mixtures (mAgnZn) were prepared initially in a dry form by mixing different proportions of antibacterial zeolite with the powder paint materials in a twin-screw extruder. The samples are denoted as mAgnZn-X, X being the weight percent of zeolite in the paint matrix. Mainly three different weight percentages were investigated, which were 0.8, 1.6, and 3.2 wt.%. 0.8 wt.% was chosen according to the industrial guideline used as a standard for the amount of antibacterial agent in the paint formulation. To investigate the effect of zeolite loading with the different metal amounts on antibacterial and color transformations of the coated alumina surfaces, increased zeolite loading amounts were subjected to study. Afterward, the product was pulverized. The pulverized products adhered onto the surface of aluminum plates with the dimensions of 30 x 5 cm electrostatically. Then, the aluminum plates coated with powder paint were heated, causing the powder to melt and be cured to form a continuous, durable film. Lastly, the plates coated with paint were cut into 5 x 5 cm pieces for antibacterial tests. The antibacterial paint coating production process is shown in Figure 3.3.

59
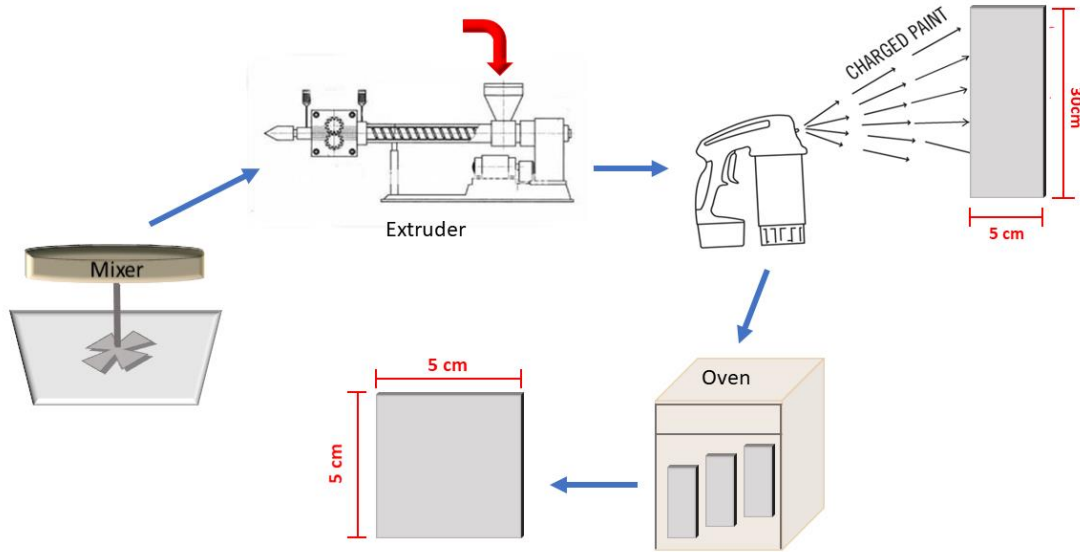
Figure 3. 3. The process of preparation of paint coatings.

3.5. Color Analysis

In chapter 4, the color analyses of coated aluminum plates were performed with Agilent Cary 60 UV-Vis Spectrophotometer. Color parameters were determined with The CIE-Lab color system, which is described as a 3-dimensional (3D) measurement system [122]. L, a and b represent brightness, red-green and yellow-blue proportion of color. The total color difference with respect to the zeolite free films is calculated from Eq. (4.1):

$$\Delta E = \sqrt{\Delta L^2 + \Delta a^2 + \Delta b^2} \qquad (4.1)$$

As indicated in the formula, all Δ represent the differences corresponding to zeolite free films and zeolite including films. For "white paint", the ΔE value must be in the range of -1 and +1.

3.6 Release Assay and Kinetics

For the release assays of thymol from the zeolitic framework, phosphate buffer saline (PBS) (pH 7.4, liquid, sterile-filtered, suitable for cell culture) was purchased from Merck, and NaCl (ReagentPlus®, ≥99%) was procured from Sigma-Aldrich.

The release assays of thymol were studied using Agilent Cary 60 UV-Vis spectrophotometer at 274 nm. Phosphate buffered saline (PBS) was used for ETS-10 crystals, whereas NaCl solution (3.5% w/v) that was prepared with PBS was used for zeolite X crystals. In a typical release assay of thymol, 25 mg of thymol loaded crystals were immersed in 20 ml of solution without stirring. After a predetermined interval of time, 2 ml of a suspension of the solution was taken off and measured and then put back into the suspension. The analysis is illustrated in Figure 3.4.
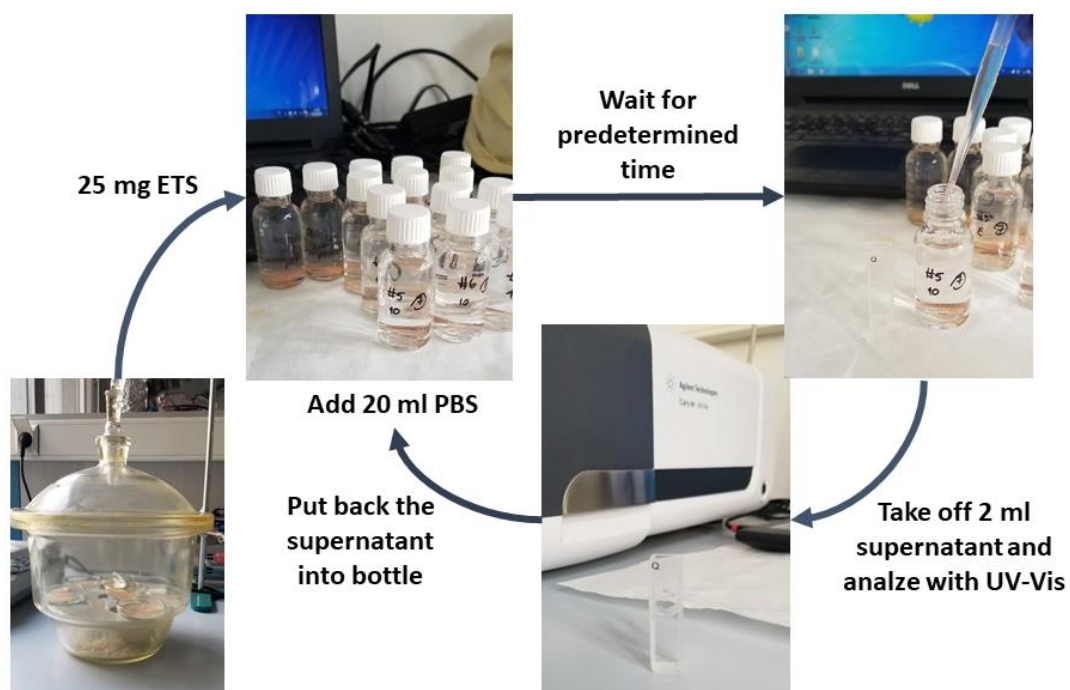
Figure 3. 4. The analysis of thymol release from the zeolitic framework.

The release assays were examined for ten days. The released concentration of thymol was determined via the acquired calibration curve of thymol at 274 nm (Appendix A, Figure A1). For the further study of thymol release mechanisms from the hierarchical structures, various kinetic models were conducted to determine the release mechanism equations, such as Higuchi [121], Korsmeyer-Peppas [123,124], Elovich [74], Zero-order and Hixson-Crowell [125]. The equations of related kinetics are listed in Appendix B. The percentage of cumulative thymol release was calculated based on Eq. (2).

$$\% \; cumulative \; thymol \; release = \sum \frac{M_t}{M_0} \times 100$$

3.7. Thermal Desorption Study

For the thermal desorption study, ZnTX-thy was removed from the desiccator and placed in an oven at pre-determined temperatures (i.e., 75°C, 100°C, 150°C, 200°C, 250°C, and 300°C) for a constant amount of time (i.e., 2 min, 5 min, and 7 min). 50 mg of ZnTX-thy kept in the oven were immersed in 20 ml of ethanol and stirred for 7 min. Then the solution was centrifuged at 8000 rpm for 5 min. After the centrifuge, the supernatant of this solution was analyzed through a UV-Vis spectrophotometer. The supernatant consisted of the released thymol from ZnTX-thy framework. The thymol absorbance peak at 274 nm was recorded after UV-Vis spectrophotometer analysis. The released thymol from ZnTX-thy at room temperature was taken as 100%. All these steps were performed for each of the indicated time and temperatures. The thermal desorption graph was drawn with the recorded absorbance thymol peaks. Figure 3.5. illustrates the thermal desorption study for ZnTX-thy.
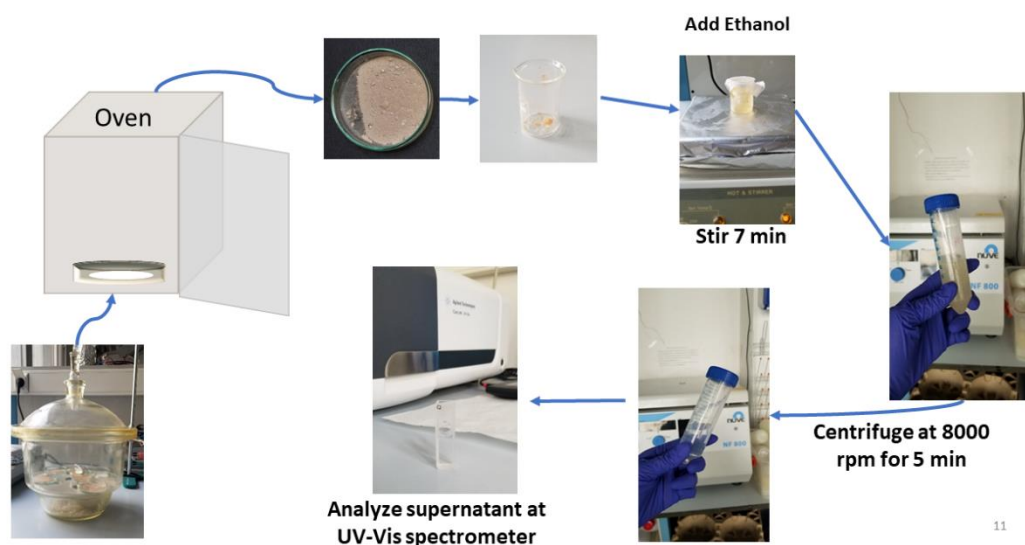
Figure 3. 5. The illustration of the thermal desorption study of ZnTX-thy.

3.8. Antimicrobial Assays

3.8.1. Disc Diffusion Test

Disc diffusion tests were performed to determine the zone of inhibition for some of the single and binary ion-exchanged zeolite NaA in chapter 4. This test was done with the pathogenic bacteria *E. coli* taken from the patients in the health center in Middle East Technical University. Overnight growth *E. coli* suspension was uniformly spread on Mueller–Hinton agar with a sterile inoculating loop. 0.19 g of exchanged zeolites in the form of pellets was located into the bacterial layer. The zone of inhibition on bacterial culture was measured after incubation for 24 h at 37 °C.

In chapter 5, the antimicrobial activities of thymol loaded ETS, 10-ETS, and 30-ETS on *P. aeruginosa* (ATCC 27853), *S. aureus* (ATCC 29213), and *C. albicans* (90028) were also determined by the disc diffusion method in the Faculty of Pharmacy,

Hacettepe University. The bacteria and *C.albicans* yeast inoculums were suspended in sterile saline and diluted according to 0.5 Mc Farland standard and then spread on Mueller–Hinton agar (Merck) and Saburaud dextrose agar (SDA) plates, respectively. The preparation of samples for the analysis is illustrated in Figure 3.6. The ethanol suspension of thymol loaded ETS-10 crystals was prepared (20% wt/wt). All pathogenic organisms were inoculated on Mueller–Hinton agar (Merck) at 37 °C overnight. Paper discs dropped with 140 µl thymol loaded ETS-10 crystals were located on agar plates. The plates were incubated at 37°C for 24 h. After incubation, the inhibition zones (mm) were measured. Ciprofloxacin (5 µg) and fluconazole (25 µg) were used as standards [126,127].
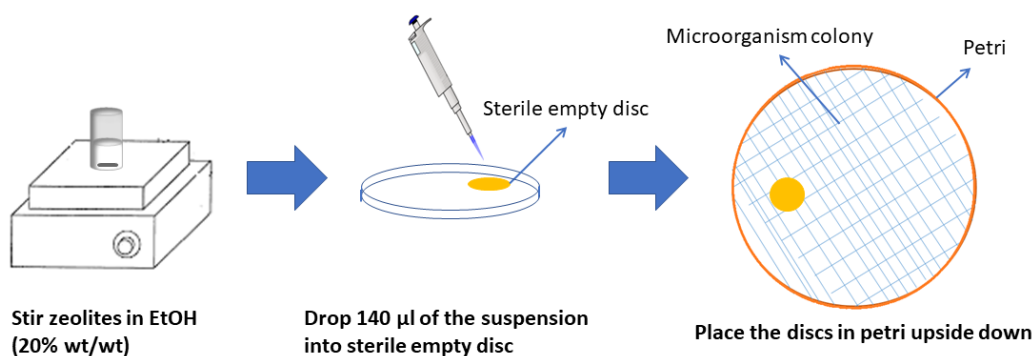
Figure 3. 6. The preparation of thymol loaded ETS-10 samples for the Disc Diffusion Assays.

3.8.2. Japanese Industrial Standard (JIZ) 2801

The antibacterial efficacy of paint composites produced by mixing with Ag^+ or Ag^+/Zn^{2+} zeolites was assessed against *E. coli* (ATCC 8739) and *S. aureus* (ATCC 6538P) based on the JIS Z 2801 standard. For the sake of clarification, a brief description of this standard assay is given. First, a single loop of bacteria from the preserved bacterial strain was transferred to nutrient agar and incubated at a

temperature of 37 °C $\pm$ 1°C. The incubated bacteria were diluted from 10^5 to 10^6 CFU/mL. Each paint coated sample was placed in a separate sterile petri dish, and 0.4 ml of the test inoculums was pipetted onto these test surfaces, as shown in Figure 3.7. The test inoculums were covered with a thick nylon bag and cut into 4 cm x 4 cm size. The samples were placed at 37 °C $\pm$ 1°C for 24 h.
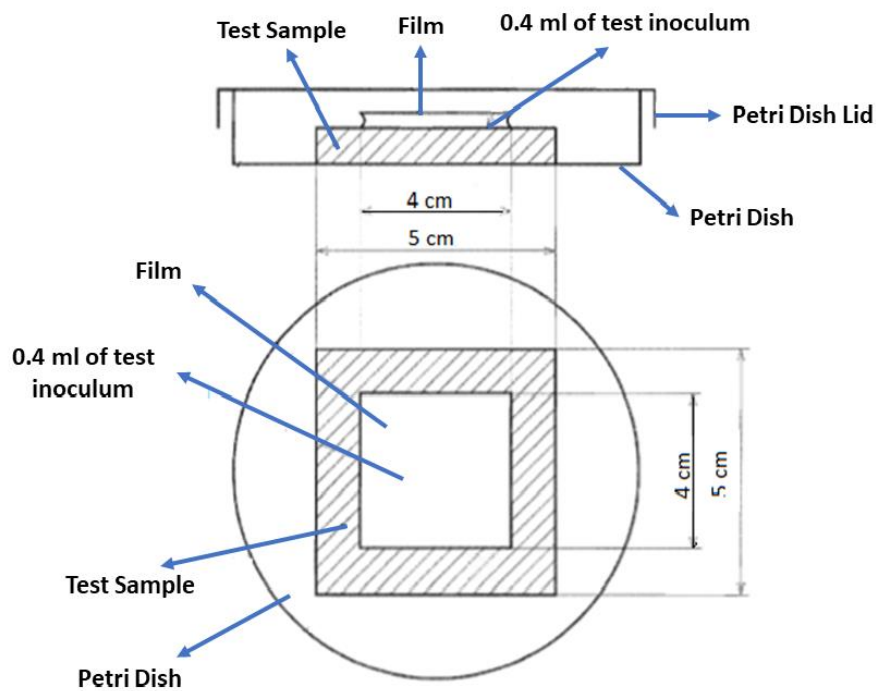
Figure 3. 7. The illustration of inoculum on the test sample for the JIS 2801 standard.

After 24 h, the samples were washed with 1 ml of SCDLP (Soybean casein digest lecithin polysorbate) in the petri dishes. 10 ml of plate count agar was spilled into each petri dish. Serial dilutions were performed with PBS (phosphate buffered saline) for each sample and each dilution was placed into a sterile petri dish. The illustration of serial dilutions for each sample is shown in Figure 3.8.
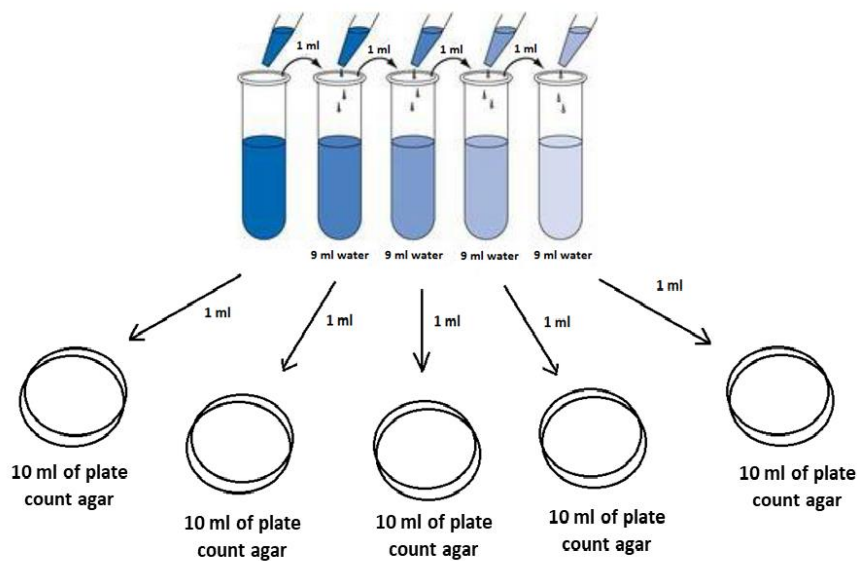
Figure 3. 8. The illustration of serial dilutions.

The petri dishes were incubated at 37 °C ± 1°C for 48 h. After incubation, colonies were quantified. Percent reduction of bacteria after 24 hour contact time was calculated from Eq. (4.2):

$$\% \ Reduction = \left[\left(\frac{B-C}{B} \right) x \ 100 \right] \qquad (4.2)$$

where B is the average number of viable bacteria in the blank sample after 24 h, and C is the average number of viable bacteria in the test samples after 24 h.

An aluminum plate was applied for coatings as a "blank" for antibacterial efficacy tests. Besides paint coatings containing metal loaded zeolites, paint coatings containing as-synthesized zeolite and paint coatings without any zeolite were also analyzed in order to determine the effect of metal ions and raw materials of paint on antibacterial efficacy, respectively.

3.9. Analytical Techniques

Zeolite A, ETS-10, zeolite X, and their post-synthesis treated forms were characterized by various techniques such as Field Emission Scanning Electron Microscopy (FE-SEM), X-ray Diffraction (XRD), UV-Vis spectrophotometer, Raman Spectroscopy, Electron Micro Probe Analysis (EPMA), X-ray Fluorescence Microscopy (XRF), Brunauer-Emmett-Teller (BET) surface area analysis and Inductively Coupled Plasma (ICP) spectrophotometry and Fourier Transform Infrared Spectroscopy (FT-IR). Except for UV-Vis spectrophotometer and Fourier Transform Infrared Spectroscopy (FT-IR) all characterization studies were performed at METU central laboratory. UV-Vis spectrophotometer was achieved in our laboratory. Fourier Transform Infrared Spectroscopy (FT-IR) was performed in the Department of Chemistry in METU.

3.9.1. Field Emission Scanning Electron Microscopy (FE-SEM)

The field emission scanning electron microscope (FE-SEM) images were captured using a Hitachi S-4700 FE-SEM with an accelerating voltage of 10 kV and 10 A beam current in secondary electron imaging mode.

3.9.2. X-ray Diffraction

Phase identification of the samples was achieved by powder X-Ray diffraction analysis using Cu Kα radiation (Rigaku Ultima IV diffractometer) between 5° and 50° with a scan speed of 1°/min.

3.9.3. UV-Vis Spectroscopy

In this thesis, the Agilent Technologies Cary 60 UV-Vis spectrophotometer was performed for several purposes. In chapter 4, the color of the paint coatings was determined by CIE-Lab color analyses with Cary WinUV Color Software. In chapter 5, thymol loaded ETS-10 crystals were analyzed with Diffuse Reflectance (DR) attachment. The DR data were collected for the wavelengths between 200-800 nm. The Kubelka-Munk function was used to convert the reflection data to absorption data and obtain absorption spectra. For the thymol release assays in chapters 5 and 6, the

absorption spectra of the release solution were assessed in wavelengths between 200-800 nm. The characteristic thymol peak at 274 nm was detected. The intensity of this characteristic peak was evaluated for the thymol release assays.

3.9.4. Raman Spectroscopy

In the Raman spectroscopy analyses, a Renishaw type Raman micro-scope was used, with an excitation wavelength of 532 nm and an acquisition power of 0.5 - 1 mW.

3.9.5. X-Ray Fluorescence Microscopy

The chemical composition of kaolin, used in chapter 4, was determined using a Rigaku ZSX Primus II X-ray fluorescence spectrometer.

3.9.6. Electron Micro Probe Analysis (EPMA)

The elemental composition of paint coatings was explored via electron microprobe (EPMA) analysis using the wavelength-dispersive (WDS) Cameca SX50 electron microprobe. A current of 25 nA, a 20 kV accelerating voltage, and a spot size of 5 microns were used as basic parameters.

3.9.7. Brunauer-Emmett-Teller (BET) surface area analysis

The pore size and area of the post-synthesis treated ETS-10, and zeolite X crystals and thymol loaded ones were evaluated by Brunauer-Emmett-Teller (BET) surface area analysis. This analysis was carried out by Quantachrome Corporation Autosorb-6B instrument.

3.9.8. Inductively Coupled Plasma - Optical Emission Spectroscopy (ICP-OES)

Metal concentrations in the ion-exchanged zeolites were determined by inductively coupled plasma optical emission spectrometry (ICP-OES–Perkin Elmer Optima 4300DV).

3.9.9. Fourier Transform Infrared Spectroscopy (FT-IR)

Powder ETS-10 crystals were analyzed by Fourier transform infrared (FTIR) spectroscopy (Thermo Scientific Nicolet iS10) with attenuated total reflection (ATR) attachment. The samples were mixed with high-density polyethylene (HDPE), in powder form, in the concentration of 5% (wt/wt), and transformed into pellet form. Pellet HDPE was used as a reference.

CHAPTER 4

ANTIBACTERIAL PAINT COATINGS CONTAINING SINGLE AND BINARY ION-EXCHANGED ZEOLITE A

In this chapter, a wide range of silver and zinc ion-exchanged zeolite 4A crystals were prepared to observe their effect on the change in antimicrobial activity over a broad spectrum. Accordingly, zeolite 4A was particularly chosen for this investigation, which retains the highest ion-exchange capacity known among different types of zeolites [39].

4.1. Synthesis and characterization of zeolite A

Raw kaolin sample was supplied from a local company, which is located in the Sındırgı, Balıkesir region of Turkey. The chemical composition of kaolin was determined from X-ray fluorescence (XRF), and the obtained results are shown in Table 4.1.

Table 4. 1. Chemical analysis of raw kaolin in wt% from X-ray fluorescence analysis (XRF).

Constituent	wt. %
SiO_2	53.6
Al_2O_3	43.9
K_2O	0.92
Fe_2O_3	0.69
TiO_2	0.39
MgO	0.19
CaO	0.17
Na_2O	0.13

According to Table 4.1., there are 0.69 wt% Fe_2O_3 and 0.39 wt % TiO_2 impurity components, which cause discoloring of the raw material and the final product. Typical process routes were followed for activation of kaolin, given that the optimization of the molar gel composition had to be investigated.
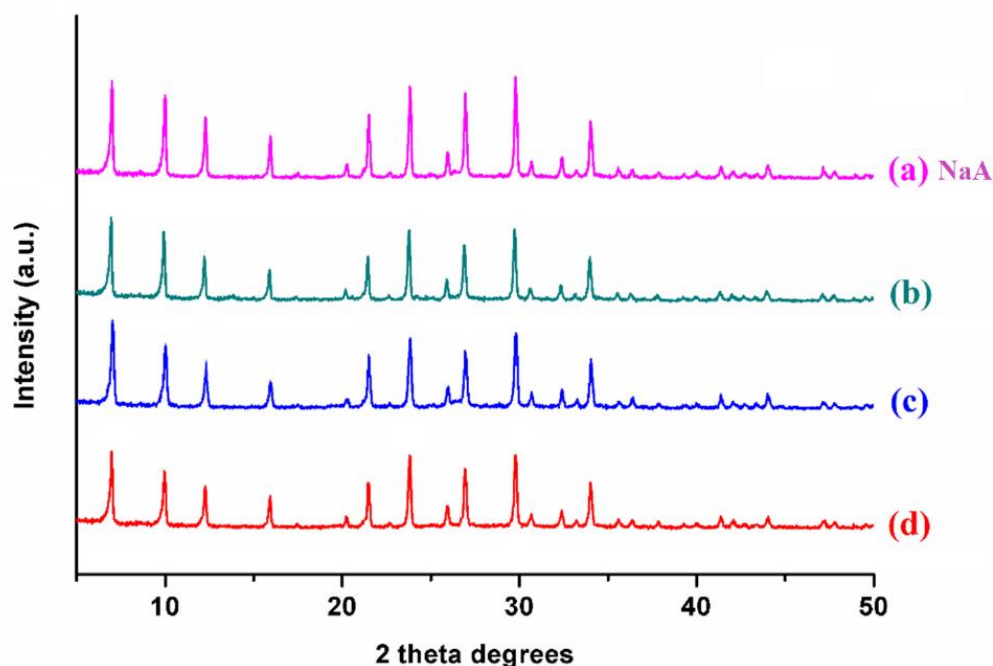
Figure 4. 1. XRD patterns of the zeolites synthesized with codes A0-1 (a), A0-2 (b), A0-3 (c) and A0-4 (d).

Figure 4.1 shows the X-ray diffraction patterns of the four samples with four different gel compositions along with a commercial zeolite A sample. Due to the importance of crystallinity of zeolite A in various applications, the crystallinities of the final products were compared, taking the most crystalline product as reference material. Optimum synthesis conditions were predicted accordingly. Percent crystallinity data was calculated via the method of Murat et al. [128], which were 100 for A0-1, 96.7 for A0-2, 96.9 for A0-3, and 93.3 for A0- 4. Upon comparing the XRD patterns of A0-1, A0-2, and A0-3, A0-4, it was observed that the peak intensities of

A0-1 and A0-3 were higher than A0-2 and A0-4 showing the most crystalline products were obtained for samples synthesized with a lower amount of water in the synthesis gel. This result correlates well with the literature data, which was explained with a decrease in the probability of nuclei formation and crystal growth of the system due to the lower concentration of species in the gel upon increased water content resulting in lower crystallinity and higher amorphous content in the final product [129,130].
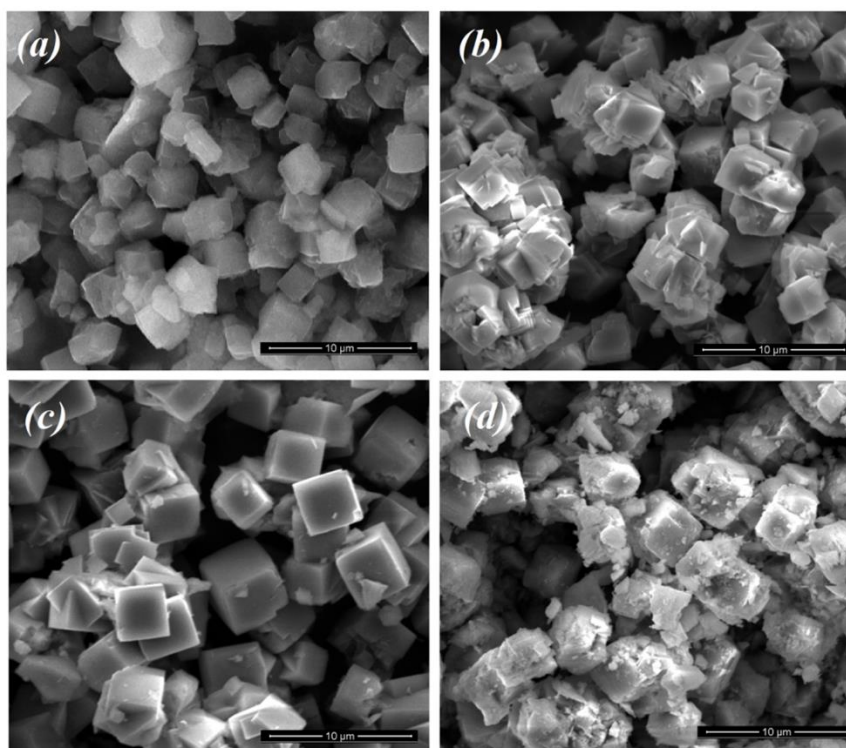
Figure 4. 2. SEM images of the zeolites synthesized with codes A0-1 (a), A0-2 (b), A0-3 (c) and A0-4 (d).

Figure 4.2 also indicates the SEM images of these four samples. According to Figure 4.2, the SEM images of A0-1 and A0-3 were also more of a desired cubic morphology with better crystalline products. The alkalinity of the system is another important parameter for zeolite synthesis [129,131]. Upon comparing A0-1 with A0-3 and A0-2 with A0-4 for constant SiO_2/Al_2O_3 ratio, it was seen that the highest crystallinity

belonged to samples A0-1 and A0-2 with the lowest Na^+ content. This behavior can be due to the tendency of increased dissolution of zeolite itself upon increased Na^+ content, which results in less crystallinity of the final product [129,130]. Another study indicated that the formation of sodalite structures rather than LTA structures occurred when increasing alkalinity in the zeolite gel [132].

Consequently, A0-1 with the synthesis gel parameters of SiO_2/Al_2O_3:2.44, Na_2O/SiO_2:1.29, H_2O/SiO_2:45 resulted in increased crystallinity and thus used as the main unmodified zeolite denoted as NaA. Accordingly, NaA was chosen to be the host material for all further ion-exchange studies. The general scheme for the preparation of coatings using NaA is illustrated in Figure 4.3. Given that the raw material used to prepare NaA was kaolin, it was of significant importance to prepare antibacterial powder samples that would adequately meet the esthetic criteria for the powder paint industry.
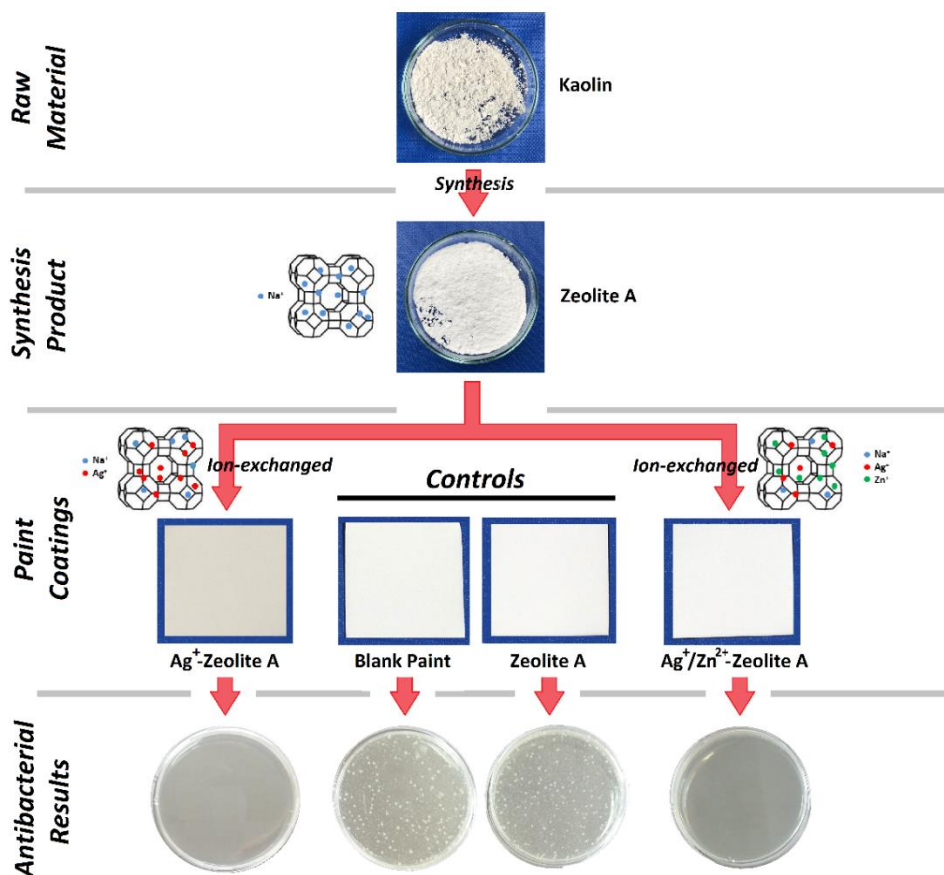
Figure 4. 3. The flow chart of antibacterial paint coatings containing single and binary ion-exchanged zeolite A.

4.2. Characterization of ion-exchanged zeolites

XRD patterns of as-synthesized zeolite NaA crystals, as well as the ion-exchanged samples, are presented in Figure 4.4. A decrease in the intensity of diffraction peaks between 2θ of 10 to 12 was observed for the ion-exchanged samples. This decrease was attributed to the dealumination of the ion-exchanged zeolite structure due to the localization of extra-framework silver [133]. This result is also coherent with a small Si/Al ratio increase, as described in Table 4.2.
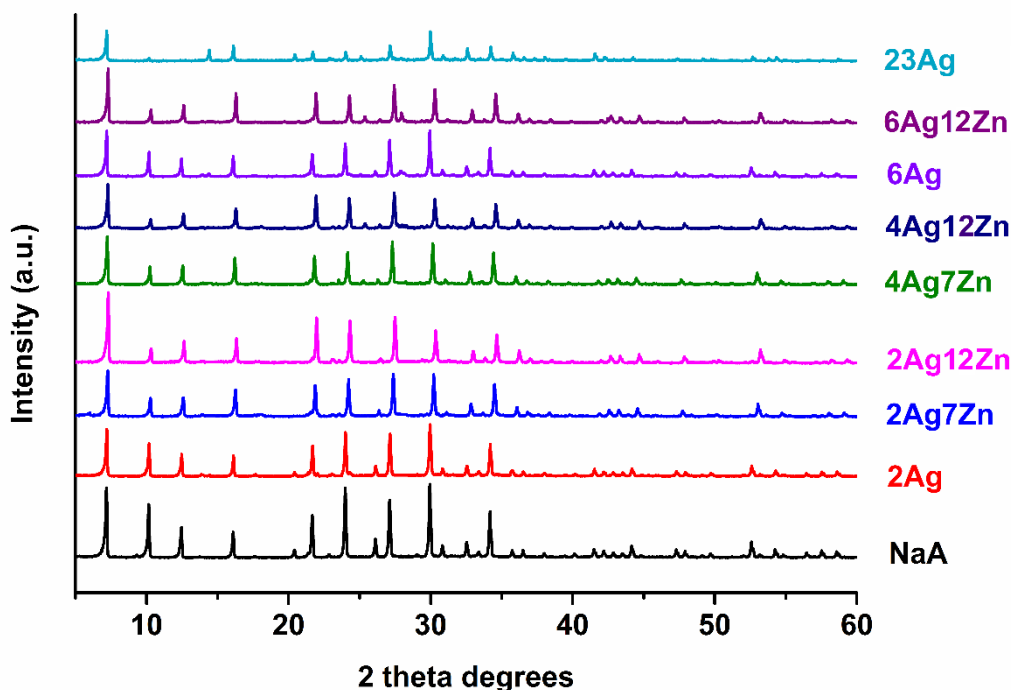
Figure 4. 4. XRD patterns of as-synthesized and ion-exchanged NaA crystals.

A slight shift to higher 2θ degrees for the samples containing Zn^{2+} cation was seen in Figure 4.4. This shift might be explained by the change in lattice parameters in the presence of both Ag^+ and Zn^{2+} cations [134,135]. There is no significant change in crystallinity for zeolite NaA crystals containing less silver (2Ag). Although the increase in silver amount decreased the crystallinity of exchanged zeolite, the characteristic XRD peak positions for all samples were well preserved, indicating ion-exchanged samples maintain the intrinsic crystalline structure of zeolite A. The only sample losing characteristic peaks is the maximum Ag^+ loaded sample (23Ag), and its calculated crystallinity decreased to 37.4%. The most significant change in Si/Al ratio was also observed for this sample (Table 4.2).

Table 4. 2. Chemical analysis and percent crystallinity of as-synthesized and ion-exchanged zeolite NaA sample.

Sample Name	Si/Al	wt. % Na	wt. % Ag	wt. % Zn	Crystallinity (%)
NaA	1.05	11	_	_	100
2Ag	1.07	10.2	1.67	_	95.6
2Ag7Zn	1.18	6.02	1.32	6.96	95.7
2Ag12Zn	1.00	2.95	2.14	11.7	95.3
4Ag7Zn	1.17	5.73	2.47	6.6	84.5
4Ag12Zn	1.19	3.04	3.26	11.1	83.7
6Ag	1.16	8.96	5.31	_	75.7
6Ag12Zn	1.09	2.95	5.61	12.6	82.9
23Ag	1.27	2.62	27.4	_	37.4

Table 4.2 also presents the quantitative results of all zeolite samples obtained by chemical analysis. It can be seen that Ag^+ and Zn^{2+} metal ions in metal-exchanged samples were in correlation with the calculated amounts, suggesting an increase in Ag^+ and Zn^{2+} amounts with increasing Ag^+ and Zn^{2+} loading content into zeolite NaA crystals along with decreasing Na^+ content. As seen in Table 4.2, the crystallinity of the samples decreased with increasing Ag^+ and Zn^{2+} loading, and the crystal structure ruined majorly at 23Ag with the crystallinity of 37.4 %.

4.3. Characterization of paint coated samples

In industry, maintaining esthetical properties of the products is the critical aim that any additive will not affect the color of the products. For this purpose, ΔE values of all samples with representative photographs of the obtained coatings are plotted and shown in Figure 4.5. The targeted ΔE values for coated surfaces to be used in the paint industry range from -1 to +1, as also emphasized in Figure 4.5.
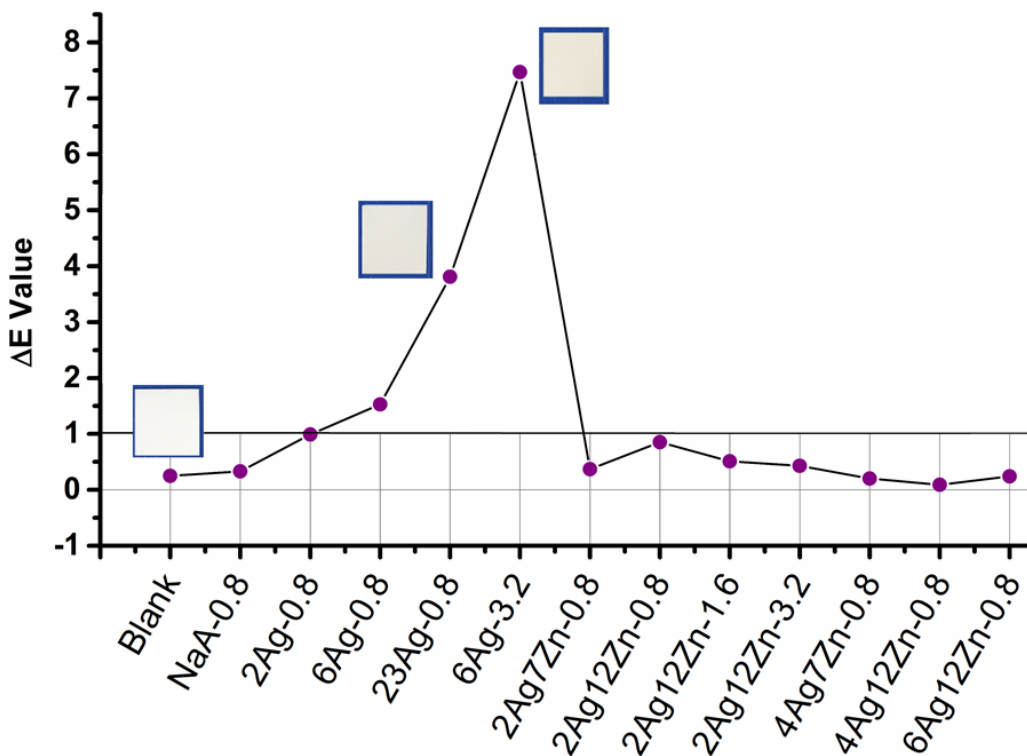
Figure 4. 5. Color difference (ΔE) values of powder paint coatings.

Upon comparing the samples that contain only Ag^+ ion according to Figure 4.5, 0.8% zeolite loading matched this criterion with a slightly increased ΔE value for 6 wt.% Ag^+ loaded zeolite containing coatings (6Ag-0.8). However, the zeolite loading amount (3.2%) seems to be deteriorating the color of the coatings immediately, as observed for sample 6Ag-3.2. A relatively less but significant deterioration was observed upon increasing the Ag^+ content to 23 wt.% even at a low zeolite loading amount (23Ag-0.8). These two samples have an apparent yellowish dark color, which was more significant for 6Ag-3.2. Accordingly, an increase in Ag^+ concentration in zeolite and also zeolite concentration in the paint for only Ag^+ ion-exchanged zeolites increased ΔE values sharply and ruined visual inspection of these coatings. Similar studies were also performed using a silica matrix with ΔE values of almost up to 18 [136]. Thus, obtaining antibacterial efficacy in composites with increased Ag^+ content or

Ag^+-containing matrix materials may not meet the industrial criteria and should be assessed with special care. For that reason, these two samples were not used for antibacterial efficacy tests.

The results suggest that the ΔE values of binary ion-exchanged samples were close to zero with much improved coloring qualities similar to the blank sample that includes no zeolite. It was seen that adding Zn^{2+} ions besides Ag^+ ions into the zeolite framework enhanced the visual appearance of the coatings. Similar observations were made visually for waterborne coatings in a previous study [65]. However, in the current study, the coloring quality was quantitatively measured and compared with each other for much lower Ag^+ concentrations with additional Zn^{2+} loadings for electrostatic powder paint coatings for the first time. Additionally, the effect of zeolite loading on the color development as a function of changing the amount of Ag^+ and Zn^{2+} was also determined and was shown to play a more significant role in the deterioration of the color of the paint coatings compared to ion loading amount.

The enhancement of ΔE value by the addition of Zn^{2+} ion can be explained by the fact that Zn^{2+} addition leads to a compensating behavior among L, a, and b values with respect to the blank sample resulting in white color with a reasonable ΔE value. Thus, coatings with 0.8% zeolite containing 6 wt.% Ag^+ (i.e., 6Ag-0.8) has a higher ΔE value of 1.53, while coatings with zeolite containing the same concentration of Ag^+ with 12 wt.% Zn^{2+} (i.e., 6Ag12Zn-0.8) has an acceptable ΔE value of 0.24. Moreover, increasing zeolite concentration in the powder paint from 0.8 to 3.2 % with constant Ag^+ and Zn^{2+} concentration (i.e., 2Ag12Zn-0.8, 2Ag12Zn-1.6, and 2Ag12Zn-3.2) showed again an acceptable ΔE value within the intended range.

To investigate the homogeneous distribution of metal loaded zeolites into the paint matrix, electron probe micro analyses (EPMA) were performed for Al, Si, Na, Ag, and Zn elements, as shown in Figure 4.6. The distributions of Na, Al, Si, Ag and Zn ions in samples that were treated for antibacterial purposes indicate zeolite distribution. EPMA results showing Ti and S distribution are due to the paint

composition. Figure 4.6-a refers to the paint coatings prepared only with zeolite without any exchanged cations (NaA-0.8). Accordingly, the homogeneous distribution of zeolite crystals can be easily assessed in the paint coated layers from the signals coming from Al, Si, and Na for an area of 50μ x 50μ. These zeolite crystals were hard to observe by FE-SEM analysis (not shown), suggesting that the crystals were embedded into the coated layer and formed a homogeneous mixture with other nanoparticles in the paint ingredients.
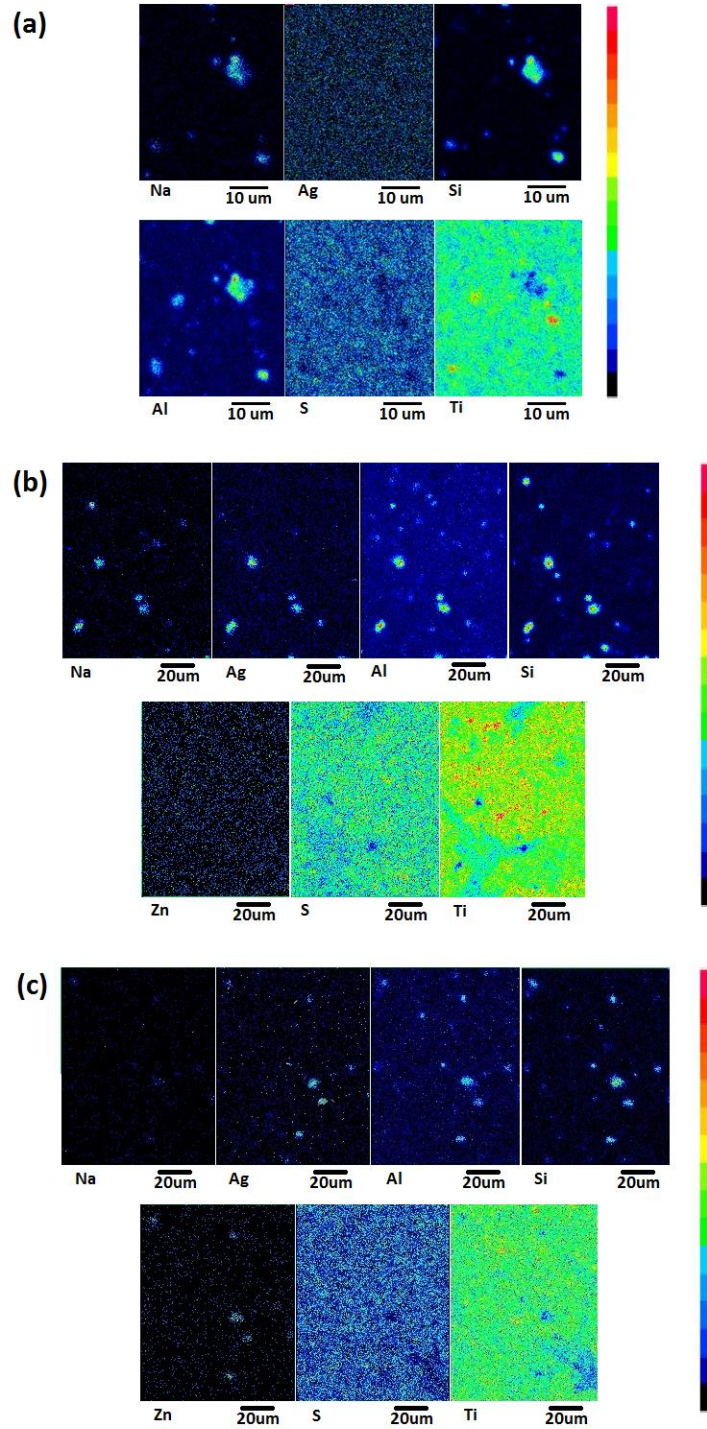
Figure 4. 6. EPMA images of NaA-0.8 (a), 6Ag-0.8 (b) and 2Ag12Zn-0.8 (c). The colored scale bar at the right indicates the relative concentration of each element.

EPMA results obtained from 6Ag-0.8 and 2Ag12Zn-0.8 samples for an area of 100μ x 100μ are shown in Figure 4.6-b and 4.6-c, respectively. Again, the homogeneous zeolite distribution on the coated layer can be judged from Al, Si, and Na elements. For this particular sample, Ag^+ distribution matches the distribution of zeolitic ions, where no Zn^{2+} was observed in Figure 4.6-b. The presence of Zn^{2+} ions can be clearly located for 2Ag12Zn-0.8 in Figure 4.6-c. In this particular sample, Na^+ detection was very low, almost unrecognizable. These results are in correlation with the chemical analysis results, as shown in Table 4.2, where Na^+ content for 2Ag12Zn-0.8 is much reduced with respect to 6Ag-0.8. This low Na^+ content is expected since both Ag^+ and Zn^{2+} ions are exchanged with Na^+ ions for the 2Ag12Zn-0.8 sample.

4.4. Antimicrobial assays

The antibacterial efficacy of the prepared paint coated surfaces was tested against Gram-negative *E. coli* ATCC 8739 and the Gram-positive *S. aureus* ATCC 6538P according to the JIS Z 2801 standard, and the percent reductions in bacterial counts were calculated after 24 hours. Table 4.3 and 4.4 summarize all the antibacterial efficacy results of the coatings against *E. coli* and *S. aureus,* respectively.

According to Table 4.3 and 4.4, the coating with the paint alone showed the antibacterial effect of 14.21% reduction for *E. coli* and 15.18% reduction for *S. aureus*, which is in correlation with previous studies suggesting color pigments could act as biocides for some kinds of bacteria [137]. Moreover, coatings prepared using NaA with no Ag^+ or Zn^{2+} ions (i.e., NaA-0.8) did not contribute to antibacterial activity, 13.03% for *E. coli* and 10.21% for *S. aureus*. This can be due to the inhibitory effect of the zeolite framework preventing antibacterial pigments from reaching the surface of the coating.

Table 4. 3. Antibacterial activity results of paint coatings containing zeolite A according to JIS Z 2801 standard against *E. coli.*

Sample	Concentration of Bacteria (CFU)		Reduction %
	0 h	24 h	
Paint w/out NaA-0.8	4.07×10^4	3.62×10^5	14.21
NaA-0.8	4.07×10^4	3.67×10^5	13.03
2Ag-0.8	4.07×10^4	2.83×10^5	32.94
6Ag-0.8	4.07×10^4	4.64×10^1	99.99
2Ag7Zn-0.8	4.07×10^4	7.60×10^4	81.99
2Ag12Zn-0.8	4.07×10^4	3.38×10^1	99.99
2Ag12Zn-1.6	4.07×10^4	2.11×10^1	99.99
2Ag12Zn-3.2	4.07×10^4	2.11×10^2	99.95
4Ag7Zn-0.8	4.07×10^4	1.01×10^5	76.07
4Ag12Zn-0.8	4.07×10^4	6.33×10^4	85.00
6Ag12Zn-0.8	4.07×10^4	1.05×10^5	75.12

Expected antibacterial activity of minimum 99% reduction in bacterial counts could not be attained by a single 2 wt.% Ag^+ ion-exchanged zeolite (2Ag-0.8) for minimum zeolite loading of 0.8%, whereas 6Ag-0.8 showed almost 100% efficacy even at the lowest loading amount. However, as shown in Figure 4.5, 6Ag-0.8 and even 23Ag-0.8 possessing a ΔE value at the upper limits were not suitable for esthetic purposes. Furthermore, increased zeolite loading and Ag^+ amount for single Ag^+ loaded zeolite coatings were not suitable due to their very high ΔE values and were not subjected to antibacterial tests (in Figure 4.5, 23Ag-0.8 and 6Ag-3.2). The antibacterial mechanism of silver is still not clearly understood. Nonetheless, Yamanaka *et al.* reported that the inhibition of silver ions disrupts the outer membrane [5]. It was also proposed that after silver ions penetrate the cell, the cytoplasm membrane dwindles and DNA becomes condensed form. DNA molecules lose their replication ability, resulting in the hindrance of cell growth [10]. Moreover, it is asserted that the main antibacterial activity is originated from the interaction of the cytoplasm of the

living cell and silver ions [5]. It is also stated that the electrostatic interaction between the negatively charged cell membrane and positively charged cations, for biocidal activity [11]. Accordingly, different secondary cations such as Zn^{2+} could be used to enhance antibacterial activity with an additional advantage of decreasing the amount of Ag+ for health and cost concerns [65]. Thus, the effect of adding Zn^{2+} cation in addition to Ag^+ was tested for powder coatings.

Table 4. 4. Antibacterial activity results of paint coatings containing zeolite A according to JIS Z 2801 standard against *S. aureus.*

Sample	Concentration of Bacteria (CFU)		Reduction %
	0 h	24 h	
Paint w/out NaA-0.8	3.45×10^4	3.24×10^5	15.18
NaA-0.8	3.45×10^4	3.43×10^5	10.21
2Ag-0.8	3.45×10^4	2.48×10^5	35.08
6Ag-0.8	3.45×10^4	1.38×10^2	99.96
2Ag7Zn-0.8	3.45×10^4	7.64×10^4	80.00
2Ag12Zn-0.8	3.45×10^4	1.42×10^2	99.99
2Ag12Zn-1.6	3.45×10^4	1.41×10^2	99.99
2Ag12Zn-3.2	3.45×10^4	7.64×10^1	99.98
4Ag7Zn-0.8	3.45×10^4	7.35×10^4	80.76
4Ag12Zn-0.8	3.45×10^4	5.73×10^4	85.00
6Ag12Zn-0.8	3.45×10^4	1.14×10^5	70.16

Having the advantage of obtaining reasonable ΔE values for all Zn^{2+} loaded zeolite coatings (Figure 4.5), it was crucial to obtain 99% antibacterial efficacy for reaching the industrial demand according to Japanese Industrial Standard JIS Z 2801 standards. For that purpose, 7 wt.% and 12 wt.% Zn^{2+} addition to 2 wt.%, 4 wt.% and

6 wt.% Ag^+ loaded zeolite coatings were subjected to antibacterial tests. According to Table 4.3 and 4.4, 7 wt.% Zn^{2+} addition to 2Ag-0.8 sample led to a significant increase in antibacterial efficacy; however, the criteria of 99% reduction could not be reached. On the other hand, the addition of 12 wt.% Zn^{2+} lead to a superior antibacterial efficacy for *E. coli* and *S. aureus* with above 99% for 2 wt.% Ag^+ loaded zeolite coatings as shown for samples 2Ag12Zn-0.8, 2Ag12Zn-1.6, and 2Ag12Zn-3.2.
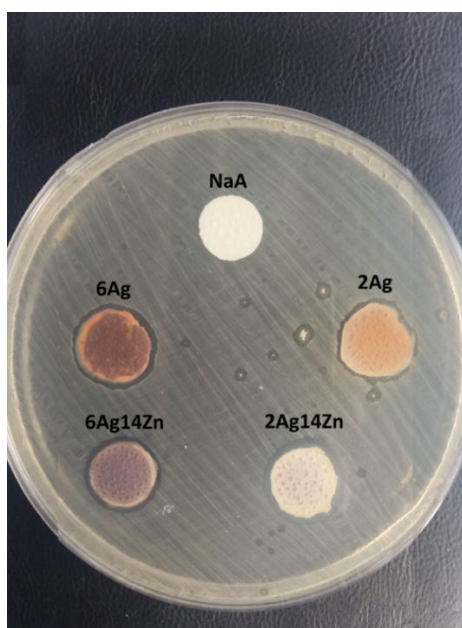
Figure 4. 7. Inhibition zones of single and binary ion-exchanged zeolite NaA.

Upon adding Zn^{2+} ions into the samples with 4 wt.% Ag^+ loading, lowered antibacterial efficacy was observed for both *E. coli* and *S. aureus* with respect to the results obtained for 2 wt.% Ag^+ loaded samples. As shown in Table 4.3, 76.06% and 85.00% reduction in *E. coli* was observed for 4Ag7Zn-0.8 and 4Ag12Zn-0.8, respectively, suggesting that Zn^{2+} addition does not necessarily always result in high antibacterial efficacy and an optimum Ag^+ content is essential. Interestingly, adding

Zn^{2+} into even higher Ag^+ loaded coating samples resulted in even more reduced activities as shown for sample 6Ag12Zn-0.8 with 75.12% and 70.16% reduction for *E. coli* and *S. aureus*, respectively.

In addition to the antibacterial efficacy assay of paint coated samples according to the JIS Z 2801 standard, powder ion-exchanged zeolite samples were subjected to the disc diffusion method to attain a general indication of their efficacy. This test was only applied to 2Ag, 2Ag12Zn, 6Ag, and 6Ag12Zn samples, and the results were shown in Figure 4.7 since the most remarkable results were obtained for these samples by JIS Z 2801 standard. As expected, no antibacterial activity was observed for zeolite NaA, whereas the presence of silver in the zeolite framework for the 2Ag sample was shown to exhibit antibacterial activity against *E. coli*. An increase in silver content in zeolite increased the antibacterial activity for the 6Ag sample. Zinc addition to the sample with lower silver content leads to a larger zone of inhibition similar to the one obtained for the 6Ag sample, with an obvious improvement in white color. Interestingly, zinc addition to 6Ag resulted in a reduced zone of inhibition (6Ag12Zn), with a change in the observed color. These results were in correlation with the results obtained for the coated samples (i.e., 2Ag-0.8, 2Ag12Zn-0.8, 6Ag-0.8, and 6Ag12Zn-0.8). The release of ions in the framework is known to be related with their accessibility and their location in the structure, which may facilitate the antibacterial activity in such binary systems [63,138]. In binary exchanged systems, it is not crucial to use a higher amount of antibacterial ion to achieve higher antibacterial activity due to the synergistic effect [138]. Higher loading of Ag^+ that is more preferred by the zeolite structure was also suggested to cause blocking based on the location and the release rate of Ag^+ [63]. Due to these factors, it was not necessary to use large amounts of Ag^+ in binary systems to achieve a certain antibacterial effect. The results obtained in the current study correlates with the literature work, where 2 wt.% Ag^+ / 12 wt.% Zn^{2+} binary zeolite systems were shown to possess enhanced antibacterial activity and the most acceptable esthetic standards for industrial coating applications.

CHAPTER 5

ANTIMICROBIAL ACTIVITY AND RELEASE KINETICS OF VOLATILE THYMOL MOLECULES ENCAPSULATED INTO HIERARCHICAL MICROPOROUS TITANOSILICATE ETS-10

ETS-10 has unique quantum-confined Ti-O-Ti chains, which had been shown to function in unique adsorption profiles comprising volatile adsorbates. The current study was conducted using ETS-10 due to the possible interaction of ETS-10 crystals and hydroxyl bonds of thymol molecules, presenting a new chemical bond formation. Thus, this chapter highlighted the novel adsorption behavior of thymol molecules in the ETS-10 network owing to its unique structural properties and ease of forming enlarged microporosity.

5.1. Characterization of as-synthesized ETS-10 and Post-Synthesis Treatments of ETS-10 crystals

The FE-SEM images and the X-ray diffraction patterns of as-synthesized and post-synthesized treated ETS-10 crystals are shown in Figure 5.1. It was observed the typical truncated bipyramid morphology of ETS-10 in Figure 5.1a-c.
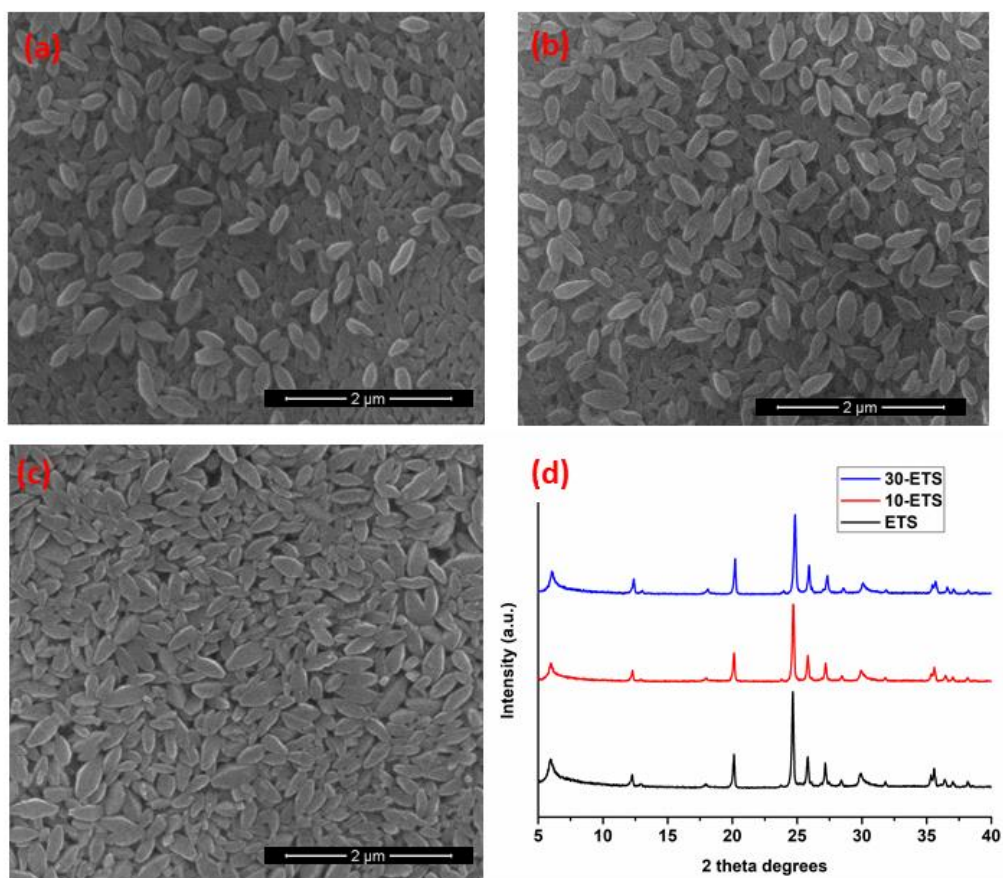
Figure 5. 1. The FE-SEM images and the X-ray diffraction patterns of as-synthesized and post-synthesized treated ETS-10 crystals.

The XRD patterns of 10-ETS and 30-ETS match well with that of ETS-10 in the literature [117], and no additional peaks were observed as shown in Figure 5.1d. The post-synthesis conditions to modify the parent ETS-10 crystals allowed the crystalline structure to be preserved with a slight reduction in the intensities. The intensity of the diffraction peaks between $2\theta = 24.65 - 27.50°$ of the parent ETS-10 was accepted as a reference sample with 100% crystallinity [139]. Based on this estimation, the crystallinity of 10-ETS and 30-ETS were 94.9 and 90.6%, respectively. These results conclude the formation of structural defects into the ETS-10 framework without considerable degradation after post-synthesis treatment.
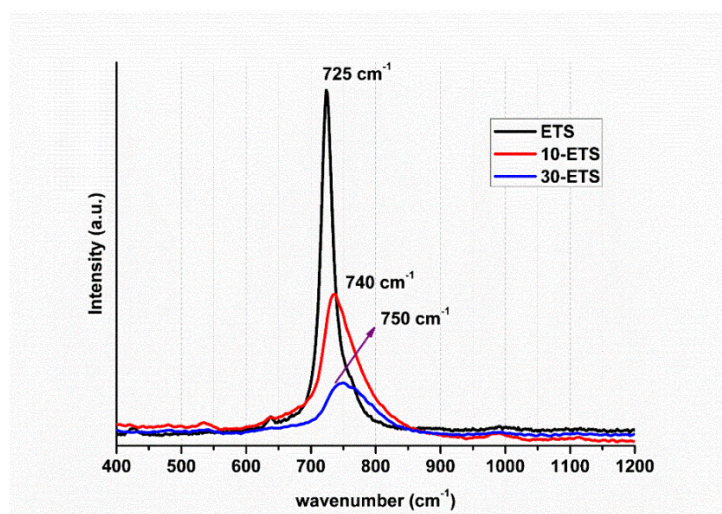
Figure 5. 2. The Raman spectra of ETS, 10-ETS, and 30-ETS-10.

The Raman spectra of ETS, 10-ETS, and 30-ETS-10 were indicated in Figure 5.2. The characteristic Ti-O-Ti stretching band of ETS was shown at 724 cm^{-1}. The post-synthesis treatments gradually decreased this band's intensity and induced 16 cm^{-1} and 26 cm^{-1} redshifts of this Raman band for 10-ETS and 30-ETS, respectively.
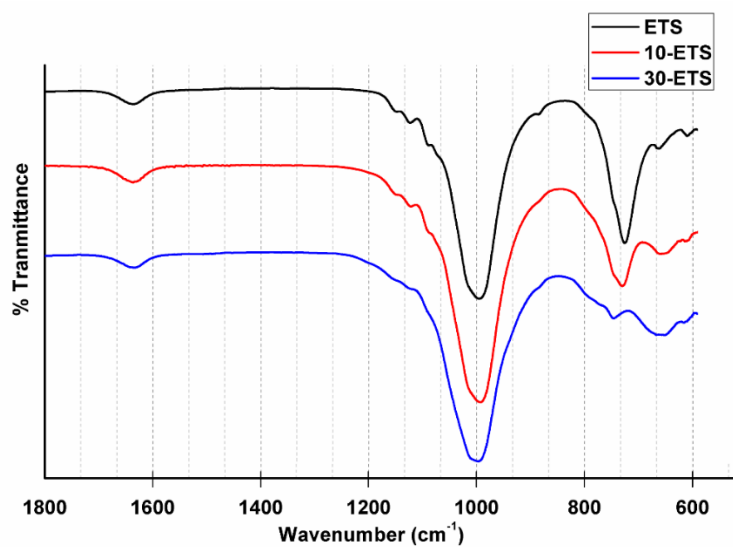
Figure 5. 3. FTIR results of post-synthesis treatment of ETS-10 crystals.

Figure 5.3 shows the FTIR results of post-synthesis treatment of ETS-10 crystals. The destruction of Ti-O-Ti chains upon post-synthesis treatment was also observed from the results obtained by the FTIR analysis. According to Figure 5.3, there was no change in the most intense vibrational band originating from the Si-O-Si stretching band at 997 cm^{-1} [140]. However, the second intense vibrational band at 724 cm^{-1} created from Ti-O-Ti stretching band decreased gradually and shifted to 747 cm^{-1} for 30-ETS sample treated at a higher concentration of H$_2$O$_2$. Moreover, the intensity of another stretching band at 660 cm^{-1} steadily increased with the increase in H$_2$O$_2$ concentration. From these results, it can be concluded that post-synthesis treatment affected Ti-O-Ti bonds without any significant damage induced to Si-O-Si bonds [117].

5.2. Thymol Loading

The proposed interactions between ETS-10 crystals and H$_2$O$_2$ and the loading of thymol into ETS crystals could be monitored by Diffuse Reflectance UV-vis spectroscopy. As shown in Figure 5.4, thymol exhibited a peak at ~450 nm. As expected, thymol encapsulation in ETS with no H$_2$O$_2$ treatment (Figure 5.4a) resulted in a slight increase in the Kubelka-Munk (K-M) diffuse reflectance intensity. Furthermore, with the gradual increase of the concentration of H$_2$O$_2$, the the Kubelka-Munk (K-M) diffuse reflectance intensity of thymol gradually enhanced at ~450 nm along with a blueshift to ~400 nm, indicating successful encapsulation into the cavity of ETS crystal.
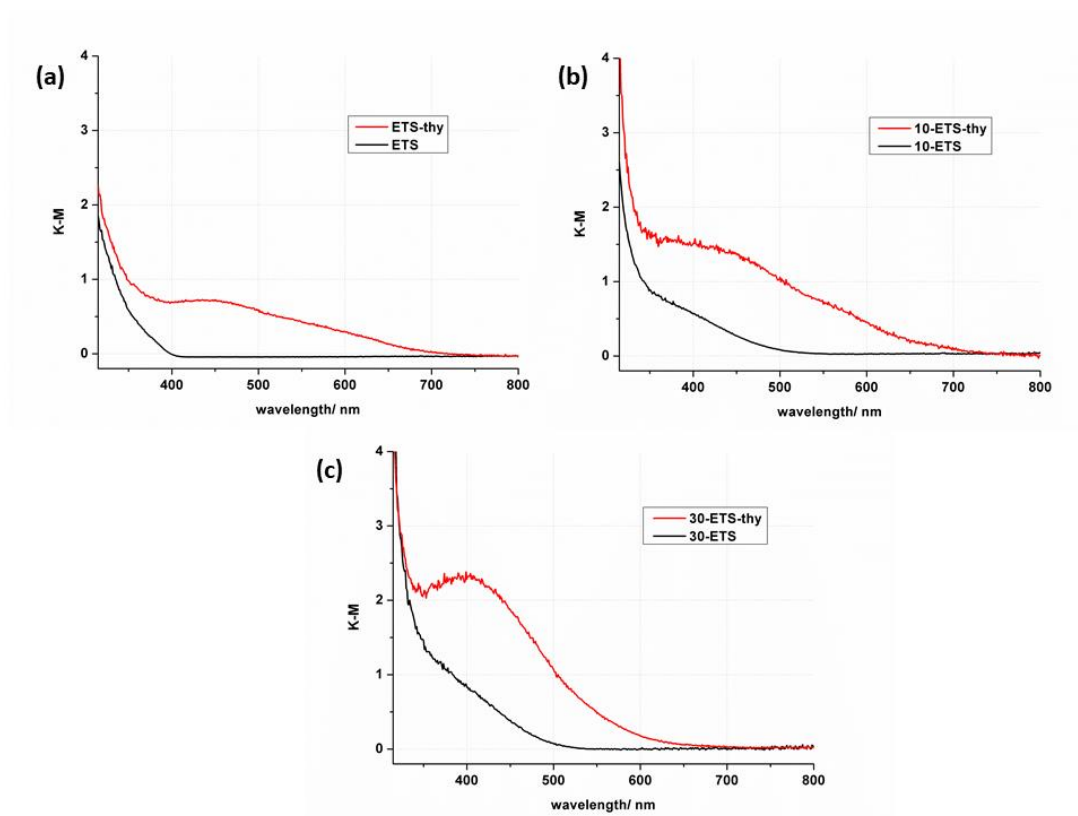
Figure 5. 4. The Diffuse Reflectance UV-vis spectroscopy of thymol loaded ETS crystals. ETS and ETS-thy (a), 10-ETS and 10-ETS-thy (b), and 30-ETS and 30-ETS-thy (b).

The reaction of H_2O_2 with titanosilicates containing Ti^{4+} in tetrahedral coordination was investigated in previous studies [117,118,141]. The interaction leads to the formation of complexes between peroxy groups and Ti^{4+} [117,118]. The formed titanium peroxo complexes exhibit new ligand-to-metal charge transfer (LMCT), observed at around 400 nm as seen in Figure 5.4 [117,141–143].
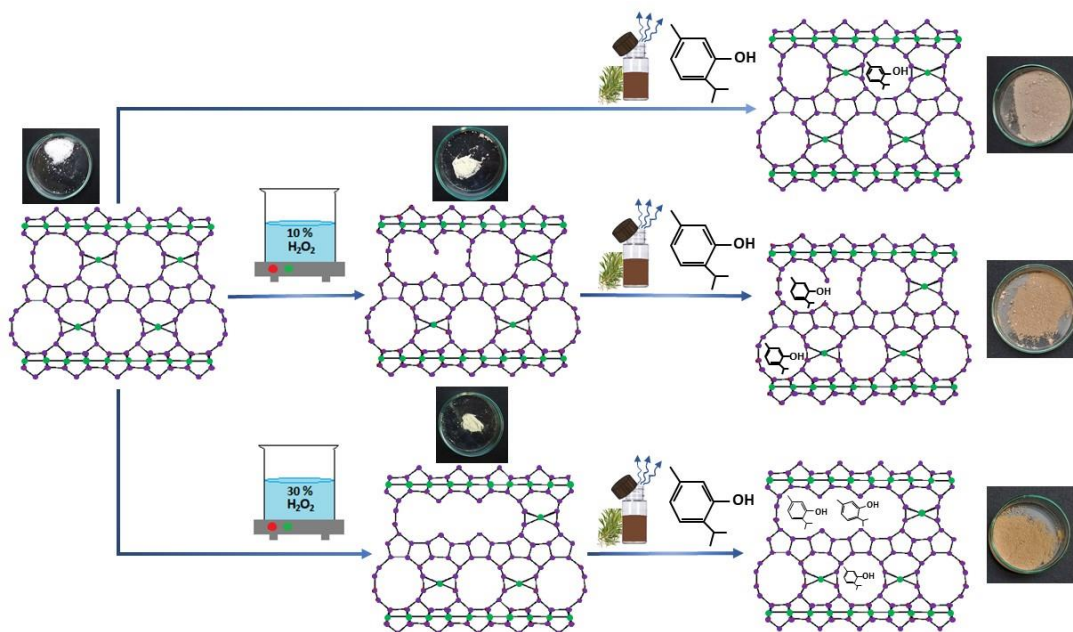
Figure 5. 5. The flow chart of thymol encapsulated ETS crystals.

Also, Figure 5.5 indicates the flow chart of this study and the photographs of the samples. The formation of titanium peroxo complexes revealed a change in color from white to yellow. The formed yellow color remained unchanged after washing double distilled water three times and drying at 323 K (Figure 5.5). The post-synthesis treatment with aqueous H_2O_2 solution triggered breaking Ti-O-Ti chains, forming active Ti sites in the framework. The active Ti sites were prone to react with H_2O_2 molecules and form such Ti-OOH groups in the presence of H_2O_2 molecules [117]. Similarly, the loading of thymol into ETS, 10-ETS, and 30-ETS were subject to the formation of an intense peak around 400-450 nm, which is attributed to the formation of new chemical bonds due to the interaction of Ti-O bonds of ETS-10 crystals and π-conjugated system and hydroxyl bonds of thymol molecules [144–147]. The π- π* transition in the conjugated C = C bonds of thymol brought about the color variance of ETS-10 crystals whose color turned to orangish pink (Figure 5.5) [145].

Table 5. 1. BET analysis of all ETS-10 samples.

Sample Name	S_{total} $(m^2/g)^a$	S_{Ext} $(m^2/g)^b$	$S_{MicroPore}$ $(m^2/g)^b$	Pore Volume $(cc/g)^c$
ETS	328.8	54.4	274.4	0.13
10-ETS	353.2	34.3	318.9	0.14
30-ETS	381.5	78.8	302.6	0.15
ETS-thy	257.7	42.8	214.9	0.1
10-ETS-thy	232.1	47.1	184.9	0.09
30-ETS-thy	189.4	42.1	147.3	0.08

[a] Determined by Multipoint BET
[b] Determined by t-Method
[c] Determined by SF Method

BET analyses of ETS-10 crystals were conducted to investigate the change in surface area after the H_2O_2 treatment and thymol loading. Table 5.1 indicates that after the H_2O_2 treatment, the total surface area increased from 328.8 m^2/g to 353.2 and 381.5 m^2/g for 10-ETS and 30-ETS, respectively. A slight increase in the pore volume was also observed from 0.13 cc/g to 0.14 and 0.15 cc/g for 10-ETS and 30-ETS, respectively. These results suggest that the H_2O_2 solution lead to partial removal of Ti atoms from the ETS-10 framework creating enlarged micropores with hierarchical nature due to the disturbed titania chains and possible removal of titania without significant degradation of crystallinity [117].

The loading of thymol is expected to decrease the surface area and pore volume of ETS-10 crystals. According to Table 5.1, the total surface area and the pore volume decreased after thymol loading for all ETS-10 samples. A gradual decrease in the total surface area (232.1 m^2/g) and the pore volume (0.09 cc/g) were achieved for 10-ETS-thy. The highest reduction in both the surface area and pore volume occurs for 30-ETS-thy (i.e., 189.4 m^2/g and 0.08 cc/g, respectively), which confer the highest loading compared to 10-ETS-thy and ETS-thy. The BET results are consistent with the total amount of thymol loaded in ETS-10 crystals. The thymol loading of the samples was calculated by measuring the weight difference between the ETS samples before and

after thymol exposure. These were measured as 3.14±0.27, 4.51±0.08, and 6.25±0.25 for ETS-thy, 10-ETS-thy, and 30-ETS-thy, respectively. Although these encapsulation amounts do not seem to be high, compared to the thymol loading in as-synthesized ETS-10 crystals, the thymol payload was slightly higher and in accordance with the H_2O_2 treatment amount for hierarchical ETS-10 crystals (i.e., 10-ETS and 30-ETS). In conclusion, the higher thymol loading with enlarged micropore size suggests that the post-treatment of ETS-10 by aqueous H_2O_2 solution is a suitable approach for obtaining more extensive thymol loading into the ETS-10 framework.

5.3. Release Assay and Kinetics

The in vitro release of thymol at pH 7.0 was examined for as-synthesized and hierarchical ETS-10 crystals as seen in Figure 5.6a. All release profiles proceeded in two stages; a burst stage that is determined in the first hour, followed by a slow step, which is observed after one h of the release. Based on the calculated calibration curve of thymol dissolved in PBS, the amount of released thymol was attained for 30-ETS-thy as 42.99 mg·g^{-1}, suggesting that 95.9% of thymol loaded in 30-ETS-thy was released during the burst stage. The release process was completed in 4 days and 12 hours. The total amount of released thymol was estimated to be 28.52 and 15.91 mg·g^{-1} for 10-ETS-thy and ETS-thy, respectively. 98.4% and 93.1% of thymol were released from 10-ETS-thy and ETS-thy frameworks during the burst stage, respectively. The whole release period was accomplished in 2 days and 16 hours for 10-ETS-thy and one day and 3 hours for ETS-thy. The hierarchical pore formation process is believed to cause a prolonged release profile mainly due to the higher extractable loading of thymol.
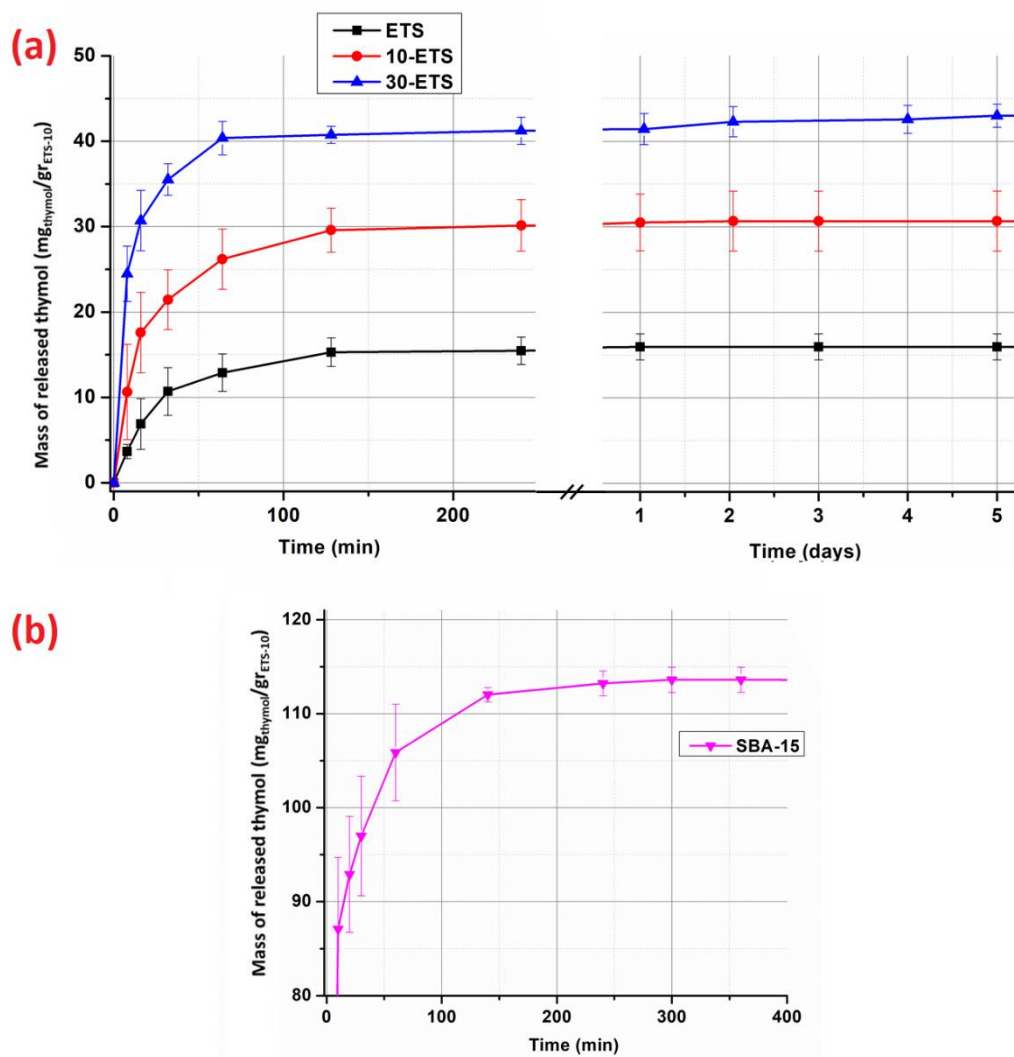
Figure 5. 6. The in vitro release of thymol from ETS-10 samples and SBA-15.

For comparison purposes, the method of thymol encapsulation was also assessed using mesoporous silica SBA-15 as seen in Figure 5.6b. The thymol release from SBA-15 was completed in 300 min. In this study, it was obtained that the release time of thymol was higher in hierarchical ETS-10 crystals when compared to SBA-15.

Table 5. 2. The various kinetics models of thymol release from ETS-10 samples.

Release Kinetics Model		ETS-thy	10-ETS-thy	30-ETS-thy
Higuchi	k	10.711	10.893	11.734
	R^2	0.9734	0.9641	0.9174
Korsemeyer-Peppas	k	1.0923	1.0965	1.1167
	R^2	0.9393	0.8927	0.8536
Elovich	k	19.806	20.759	22.984
	R^2	0.9399	0.9888	0.9939
Hixson-Crowell	k	-0.0065	-0.0101	-0.0085
	R^2	0.9375	0.9211	0.8867

Various kinetic models of thymol release from ETS-10 samples were evaluated. The calculated release rate (k) for the different models and the coefficient of determination (R^2) are displayed in Table 5.2. The best-fitting kinetic release profiles of thymol loaded ETS-10 crystals are illustrated in Figure 5.7. The most appropriate model to explain the release mechanism of thymol from ETS-thy is the Higuchi kinetic release model with the highest R^2 value ($R^2 = 0.9734$). In this release model, the cumulative amount of drug released is directly proportional to the square root of time. The Higuchi kinetic release model is based on Fickian diffusion [148]. This model is suitable for the systems in which the guest is homogeneously dispersed in the host materials [149].
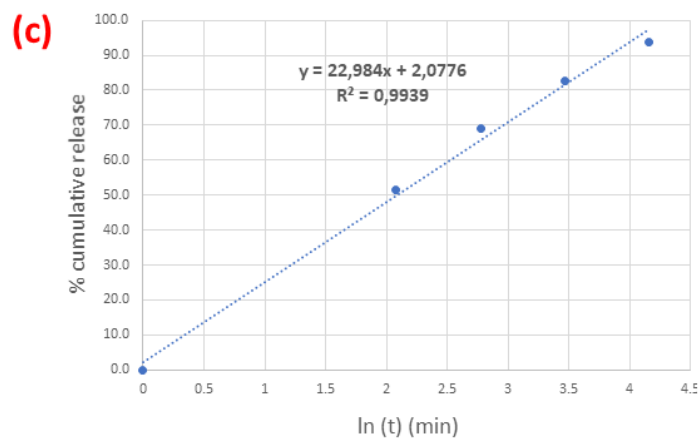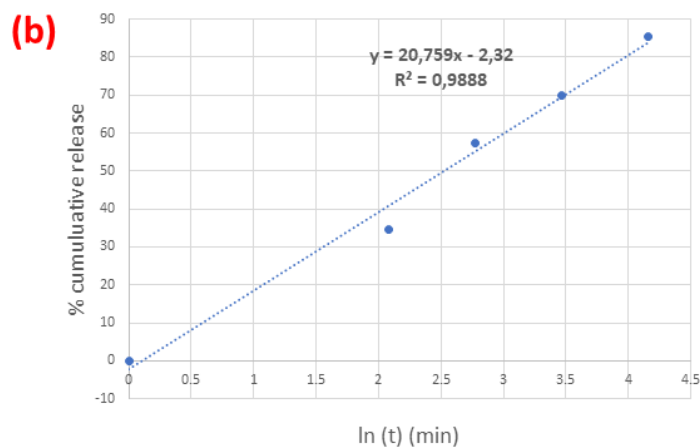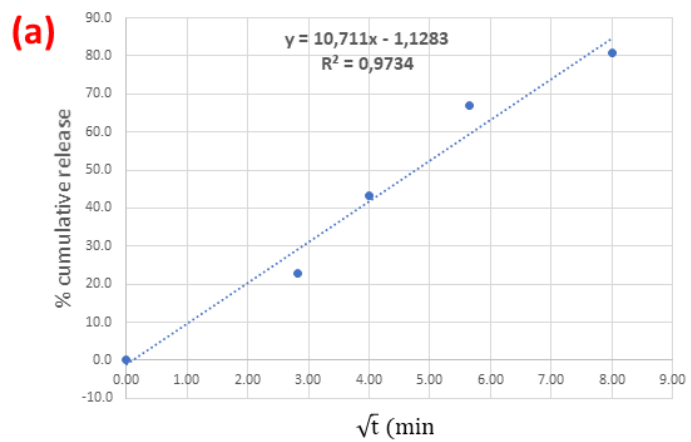
Figure 5. 7. The best fitting kinetic release profiles of thymol loaded ETS (a), 10-ETS (b) and 30-ETS (c).

According to Table 5.2, after the H_2O_2 treatment, the formation of defects into ETS-10 channels produced an alternative release profile to fit the release of thymol from ETS-10 crystals. The Elovich equation was the most appropriate for the thymol release profile from 10-ETS-thy and 30-ETS-thy (R^2 = 0.9888 and R^2 = 0.9939, respectively) (Figure 5.7). Elovich release profile underlines the fact that the thymol release occurs through a logarithmic and time-dependent transport mechanism. In this mechanism, the host's complex framework promotes fast solvent diffusion into and out of the host [74]. The rapid release of adsorbed thymol on the host's outer surface and the slow release of thymol placed in the inner parts of the host was remarked in this release profile [74]. The difference in concentration of H_2O_2 treatment resulted in different pore structures that caused different amounts of thymol and release kinetics.

5.4. Antimicrobial Assays

The antimicrobial assays of thymol loaded ETS-10 crystals were assessed against *P. aeruginosa* as a gram-negative bacterium, *S. aureus* as a gram-positive bacterium, and *C. albicans* as yeast. The disc-diffusion assays' results are graphically represented in Figure 5.8. It can be stated that all thymol-loaded ETS-10 crystals displayed antimicrobial activity; however, such activity was absent for pristine ETS-10 crystals (Appendix C, Figure C.1 and Table C.1).
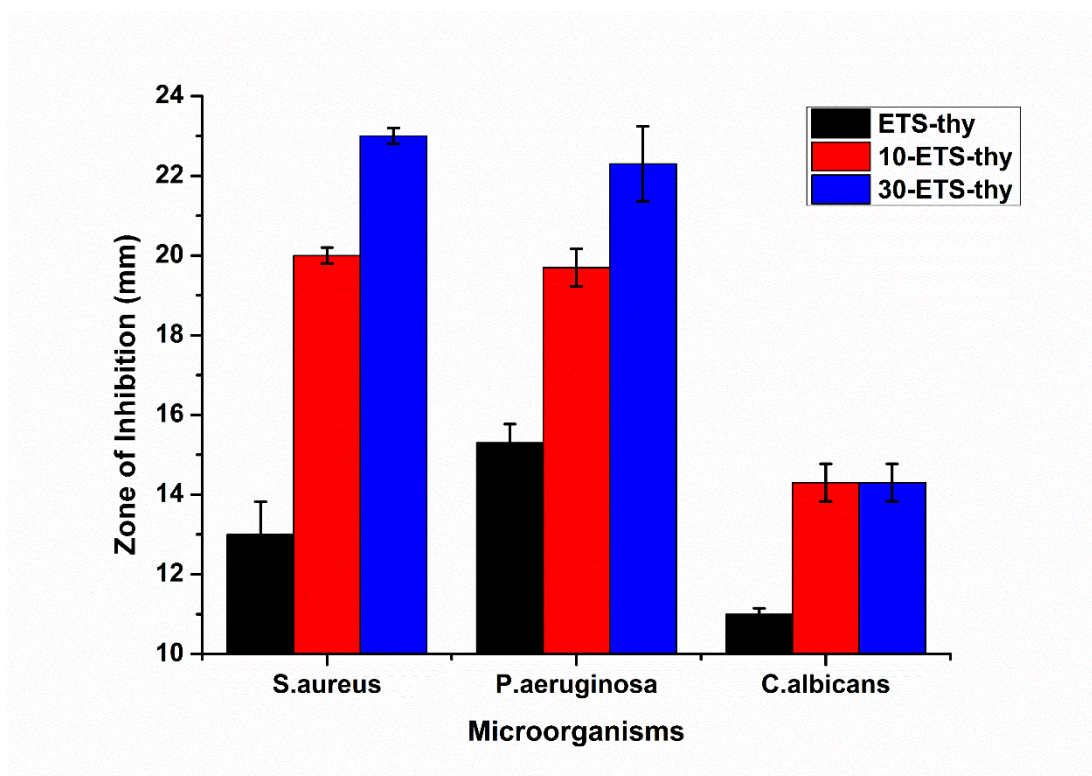
Figure 5. 8. Disc diffusion tests for thymol loaded ETS-10 samples.

An increase in well-defined zones of inhibition was noted for all microorganisms with the increase in H_2O_2 treatment. The inhibition zone diameter of the ETS-thy, 10-ETS-thy, and 30-ETS-thy against *S. aureus* was 13.0 mm, 20.0 mm, and 23.0 mm, respectively. Also, the one of the ETS-thy, 10-ETS-thy, and 30-ETS-thy against *P. aeruginosa* was 15.3 mm, 19.7 mm, and 22.3 mm, respectively. A similar enhancement in antimicrobial activity against *C. albicans* was also noticed. Increasing the formation of defects in the ETS-10 framework due to H_2O_2 treatment offered a higher thymol amount in the framework and increased antimicrobial activity. In other words, a gradual rise in antimicrobial activity can be suggested to be accomplished by the enlargement of ETS-10 crystal pore size due to H_2O_2 treatment.

In conclusion, the higher thymol loading with enlarged micropore size suggests that the post-treatment of ETS-10 by aqueous H_2O_2 solution is a suitable approach for obtaining more extensive thymol loading into the ETS-10 framework. The extensive thymol loading induced an increase in the release time. Compared to the thymol release time from mesoporous SBA-15, hierarchical ETS samples offered a more striking result. The release of thymol from SBA-15 is over at 300 min. On the contrary, the release of thymol from SBA-15 is over at 300 min, the release of thymol increases up to 4 days and 12 hours for 30-ETS. Enlarged micropore size proposes a significant increase in the release time and also antimicrobial activity. The antimicrobial activity against *S. aureus*, *P. aeruginosa,* and also *C. albicans* was enhanced with the post-treatment of ETS-10. Moreover, the addition of zinc cation into the porous structure with the enlargement of micropores could offer superior antimicrobial activity.

CHAPTER 6

BIOCIDE AND RELEASE NATURE OF THYMOL ENCAPSULATED INTO ZINC EXCHANGED POST-TREATED ZEOLITE X

For this part of the study, a large pore Zeolite X, a typical faujasite (FAU) zeolite, was used as a promising matrix for encapsulating essential oils. The zeolite X had been of high demand in encapsulation studies based on its large pore system along with the ease in its commercial availability. Thus, in this chapter, with the potential of high payload capability, zeolite X was selected to encapsulate thymol molecules.

6.1. Characterization of Zeolite X, Post-treated Zeolite X, and Ion-exchanged Forms

SEM images of the zeolite X and hierarchical zeolite X are indicated in Figure 6.1. Figure 6.1a shows the typical intergrown crystal morphology of commercial zeolite X. According to Figure 6.1b, most crystals preserved the integrity of crystal structure; however, the formation of holes in the structure of some crystals was observed after the post-treated process (inset of Figure 6.1b). This deformation can be due to the dealumination of the crystal structure, as also reported in the literature [113].
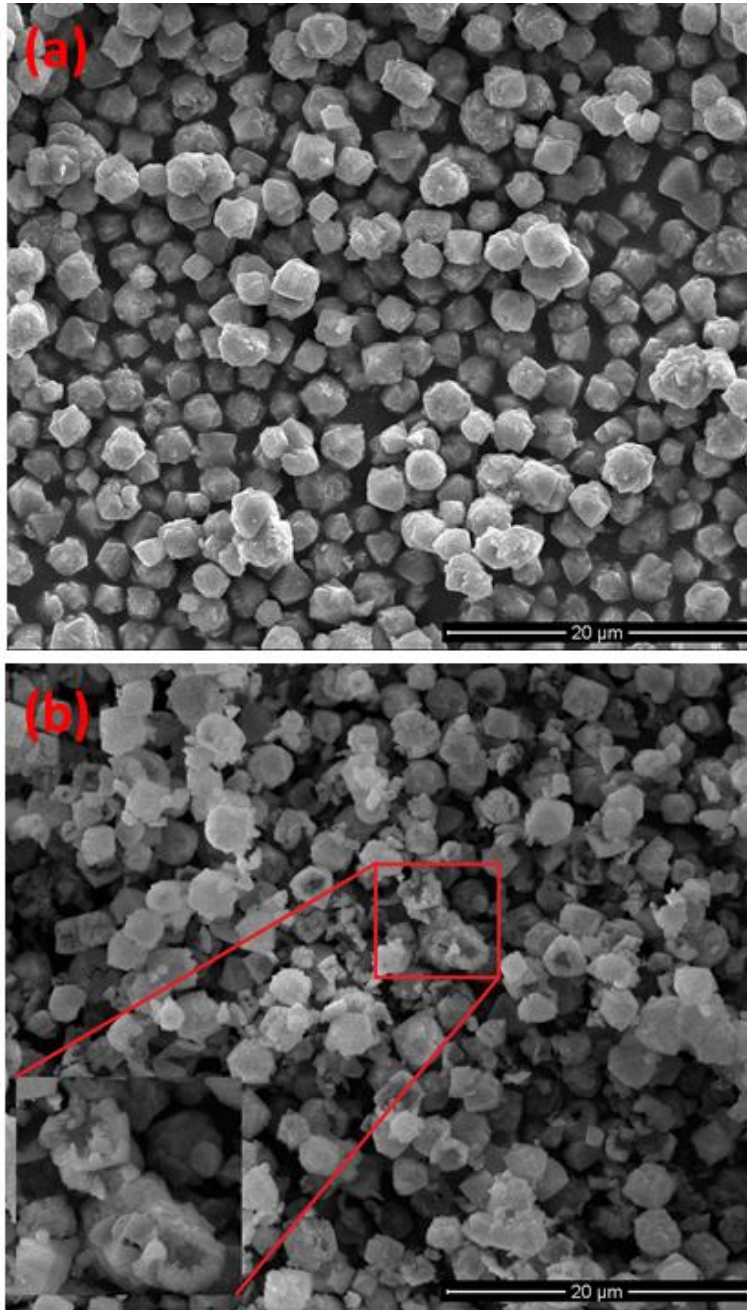
Figure 6. 1. SEM images of X (a) and TX (b).

The BET surface area analyses were performed to determine the change in porous textural properties after the post-treated process. Table 6.1 summarizes the

results of the BET porous textural properties of the samples. According to Table 6.1, the post-treatment process increased the BET surface area from 644.5 to 838.3 m^2/g. Also, the external surface area increased from 142.5 to 781.9 m^2/g and an increase in the pore volume from 0.33 to 0.26 cc/g after the post-treatment process. The micropore surface area was observed to decrease from 502.2 to 56.4 m^2/g. The micropores have been enlarged and converted into mesopores structure. All the findings suggest that the post-treatment applied to zeolite X samples resulted in the hierarchical pore formation, which was aimed for higher thymol encapsulation.

Table 6. 1. Porous textural properties of the zeolite X and post-treated zeolite.

Sample Name	S$_{BET}$ (m^2/g)^a	S$_{ext}$ (m^2/g)^b	S$_{MicroPore}$ (m^2/g)^b	Pore Volume (cc/g)^c
X	644.5	142.2	502.2	0.26
TX	838.3	781.9	56.4	0.33

^{a} Determined by Multipoint BET
^{b} Determined by t-Method
^{c} Determined by SF Method

The crystallinity of commercial zeolite X, post-treated zeolite X, and ion-exchanged forms of these crystals were investigated through X-Ray Diffraction analyses. The X-ray diffraction patterns of the crystals are shown in Figure 6.2. As seen in Figure 6.2, the main peaks for zeolite X were also seen for all treated samples, indicating the structure was preserved. However, the post-treatment approach led to a decrease in the peak intensity zeolite X, which can be attributed to the dealumination treatment applied using H$_2$Na$_2$EDTA (i.e., TX). Moreover, after the ion-exchange processes (i.e., ZnX and ZnTX), there is a slight reduction of crystallinity. This reduction can be attributed to the dealumination of the structure, which could be connected to the position of extra-framework cations [133].
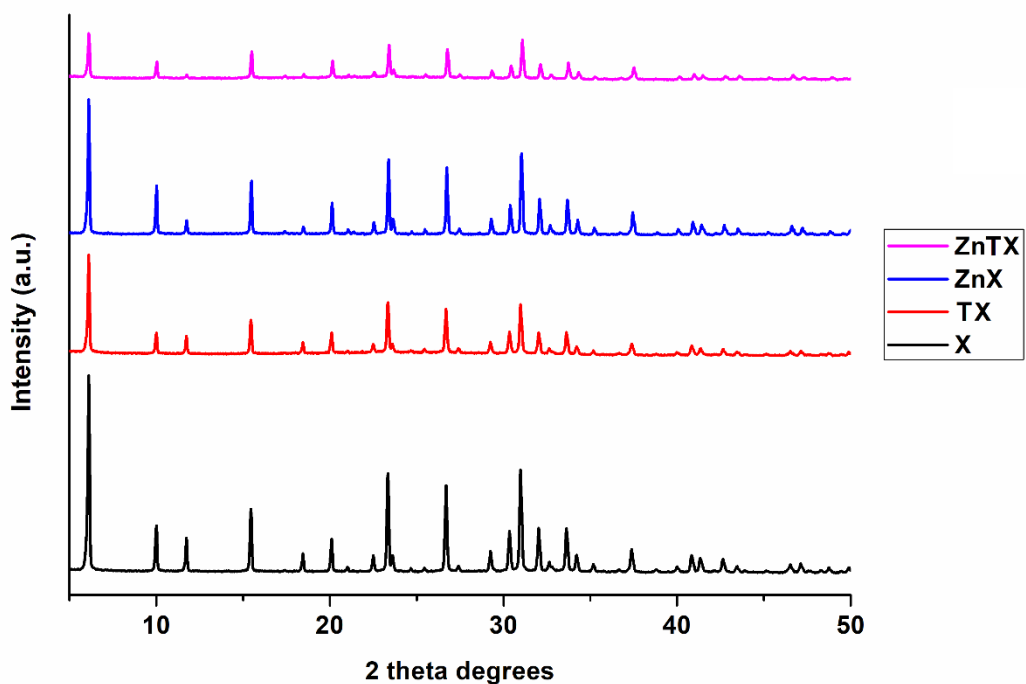
Figure 6. 2. XRD patterns of zeolite X, post-treated X, and ion-exchanged forms of these zeolites.

The ICP-OES analysis was performed, and the results are shown in Table 6.2. The Si/Al ratio of zeolite X increased from 1.18 to 1.86 after the post-treated method (i.e., TX), which is expected since the applied treatment is known to cause the dealumination of the zeolite framework.

Table 6. 2. ICP-OES results of the zeolite X, post-treated zeolite X, and ion-exchanged forms of these zeolites.

Sample	Si/Al ratio	Na wt.%	Zn wt.%
X	1.18±0.2	9.1±0.3	-
TX	1.86±0.2	6.0±0.3	-
ZnX	1.18±0.2	5.2±0.2	6.8±0.2
ZnTX	1.86±0.2	1.9±0.1	7.2±0.2

According to Table 6.2, the Na^+ concentration was observed to decrease upon the loading of Zn^{2+}, which is expected to suggest a successful ion-exchange of Zn^{2+} with Na^+ ions. After the ion-exchange process in the samples of ZnX and ZnTX, thymol was encapsulated into these samples. The maximum loading of Zn^{2+} was determined as 7.2 wt.% for ZnTX experimentally. To retain the thymol concentration as the only variable in this study, the Zn^{2+} concentration in ZnX was adjusted to be about 7 wt.%.

6.2. Thymol Loading

The thymol loading of the samples was calculated by measuring the weight difference between the zeolite X samples before and after thymol exposure. These were measured as 0.41±0.06, 0.44±0.06, 6.77±0.29, and 7.82±0.34 for X-thy, ZnX-thy, TX-thy, and ZnTX-thy, respectively. These results suggest that the post-treatment method applied to the hierarchical pore structure was successful for the enhancement of thymol loading into zeolite X. In the literature, the thymol molecules were generally encapsulated into cyclodextrin, resulting in a high loading capacity of up to 50 % [68,75]. This payload amount was related to the thymol's organic structure, which has a high tendency to absorb organic molecules.

In the literature, Thermal Gravimetric analyses were performed to determine the thermal stability of samples. However, the thymol amount in X-thy and ZnX-thy is under the detection limit, and the one in TX and ZnTX is very close to the detection

limit in this study. Therefore, another method was explored, named the thermal desorption study, and this method was explained in Chapter 3.7. Figure 6.3 shows the change in % thymol amount in ZnTX-thy with varying duration of times the samples were kept at different temperatures.
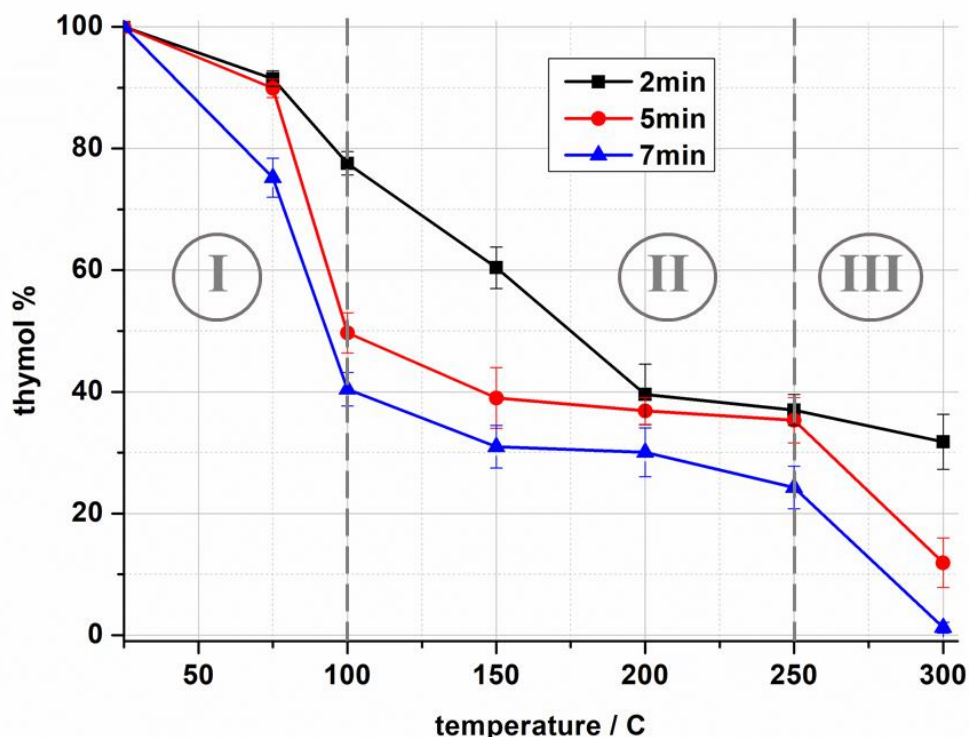
Figure 6. 3. The thermal desorption study of ZnTX-thy.

As shown in Fig 6.3, % thymol released decrease as a function of increased temperature, for which the samples were maintained at all durations of time. The overall amount released from the samples after the treatment at 300 ºC increased with the duration at which the samples were maintained in the order of 11 and 31% for 5 and 7 min, respectively. In general, the released amount can be investigated in three regions. The sharpest decrease was observed in Region-I followed by Region-III. It seems that maintaining samples for 7 minutes seems to release all available thymol

molecules, while it was still remaining in the pores upon 2 and 5-minutes of duration in the oven at 300 ºC. Based on the evaporation temperature of thymol [68], the developed process using zeolite X can be suggested to encapsulate the thymol molecule, resulting in its release at higher temperatures. This result is more evident in Region-II for temperatures between 100 and 250 ºC. After the initial burst release observed until 100 ºC, the amount decreased from the samples showed a more linear profile for 5 and 7 minutes of durations. For the samples kept for 5 minutes at 250 ºC, there was still ~40% thymol remaining in ZnTX-thy. It seems that the physisorbed amount desorbed from the outer surface until 100 ºC with the extended desorption of thymol from the inner framework at higher temperatures. This behavior suggests that the developed encapsulation method was successful for enhancing thermal stability and prolonged release at higher temperatures.

6.3. Release Assay and Kinetics

The in vitro release of thymol in the solution of PBS with 3.5% wt NaCl was examined for zeolite X crystals. The results obtained from zeolite A in its as-received (X-thy and ZnX-thy; Figure 6.4a) and post-treated forms (TX-thy and ZnTX-thy; Figure 6.4b) are shown in Figure 6.4.

The amount of released thymol was measured to be 2.2 ± 0.5 mg·g^{-1} for X-thy, which was completed in 260 min. For ZnX-thy, the amount of released thymol was only slightly higher than that obtained from X-thy (i.e., 3.1 ± 0.2 mg·g^{-1}). However, a faster release was observed for ZnX-thy, which decreased to 70 min. This decrease in release time can be due to replacing two Na$^+$ by one divalent Zn^{2+} cation, causing an increase in pore accessibility for thymol molecules [150].
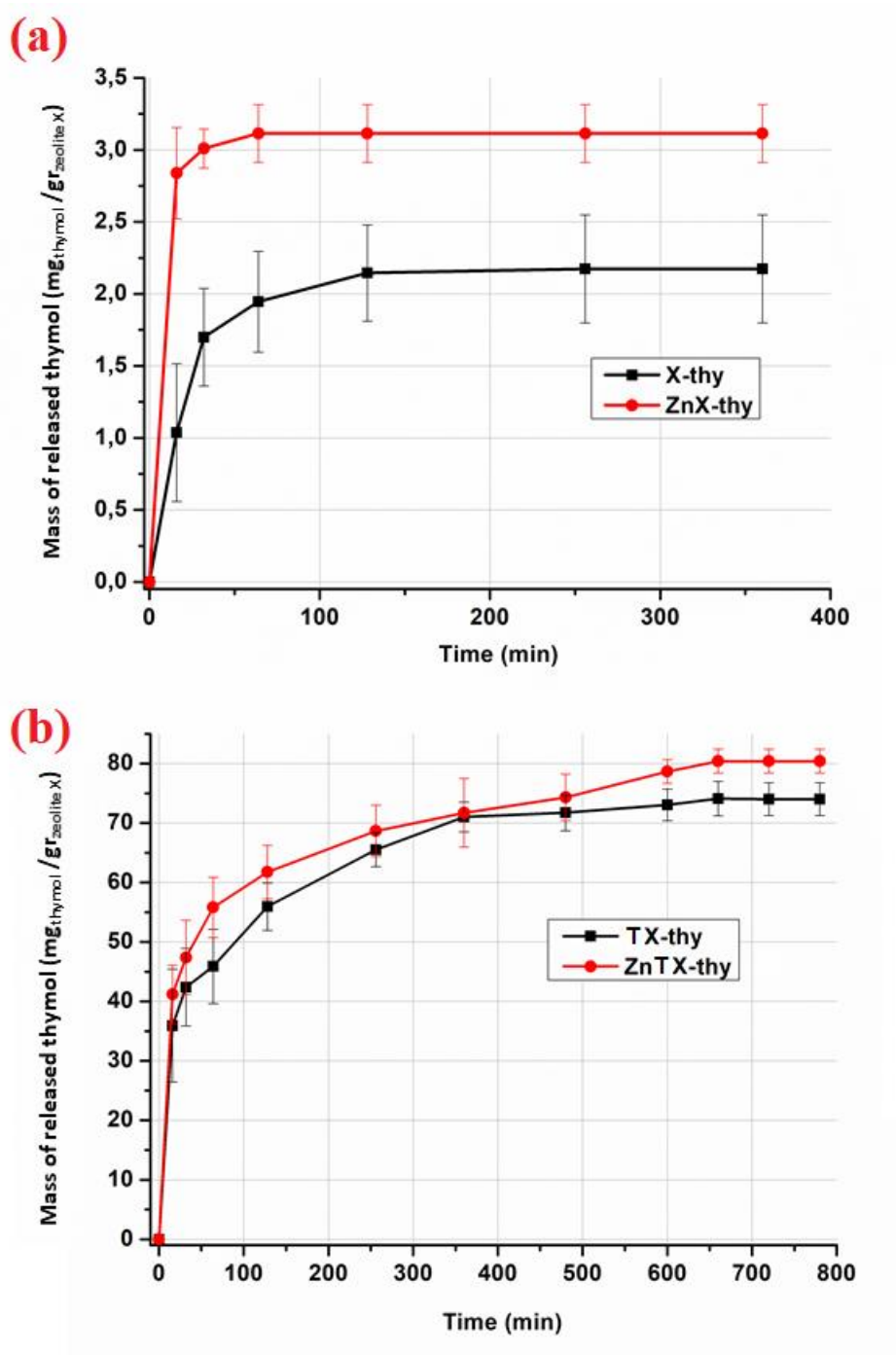
Figure 6. 4. The thymol release assays of X-thy and ZnX-thy (a) and TX-thy and ZnTX-thy (b).

As seen in Figure 6.4b, the amount of released thymol increased significantly for both TX-thy and ZnTX-thy, with a slightly higher loading for ZnTX-thy, increased due to superior adsorption thymol molecules. The thymol loading amounts were found to be 74.3 ± 2.8 and 80.4 ± 1.0 mg·g^{-1} for TX-thy and ZnTX-thy, respectively. Furthermore, the release process was completed at 660 min for both samples. The significant increase in the amount released can be due to the hierarchical structure created in zeolite X upon applying the post-treatment process. In order to assess more details on the mechanism, a kinetic model was developed for these samples.

Table 6. 3. The several kinetics models of thymol release from zeolite X samples.

Release Kinetics Model		X-thy	ZnX-thy	TX-thy	ZnTX-thy
Higuchi	k	11.627	8.2587	5.0539	6.9827
	R^2	0.9727	0.65	0.858	0.8769
Korsemeyer-Peppas	k	1.1501	1.002	0.1509	0.9461
	R^2	0.9546	0.8414	0.8856	0.8906
Zero order	k	0.6147	1.2915	0.8447	0.4868
	R^2	0.7985	0.5383	0.6459	0.605
Elovich	k	19.149	21.815	15.612	16.859
	R^2	0.9695	0.8819	0.9933	0.9940

Several kinetic models for thymol released from zeolite X samples were assessed. The calculated release rate (k) for the different models and the coefficient of determination (R^2) are presented in Table 6.3. The most suitable model to describe the release mechanism of thymol from X-thy is the Higuchi kinetic release model with the highest R^2 value ($R^2 = 0.9695$). In this release model, the cumulative amount of drug

released is directly proportional to the square root of time. The Higuchi kinetic release model is based on Fickian diffusion [148]. This model is a mathematical equation that explains the release rate of drugs from a solid matrix structure and is suitable for the systems in which the guest is homogeneously dispersed in the host materials [149].

As seen in Table 6.3, both ion-exchange and post-treatment processes altered the thymol release kinetics from the zeolite structure. The ion-exchange process gave rise to a quick release (Figure 6.4a). Even if the best appropriate kinetic release model seems to be Elovich kinetic release model according to Table 6.3, the coefficient of determination is quite low (i.e., $R^2 = 0.8819$).

After the post-treatment process, the best fitting profile of the thymol release kinetics from TX-thy was determined to be the Elovich release model with high coefficient of determination (i.e., $R^2 = 0.9933$), as seen in Table 6.3. For the release of thymol from ZnTX-thy, the R^2 value is close to TX-thy (i.e., $R^2 = 0.9940$). Also, similar release behavior is displayed in Figure 6.4b. Thus, the Elovich release model was found to be also the most proper release model for the release of thymol from ZnTX-thy, as seen in Table 6.3. The thymol release occurs through a logarithmic and time-dependent transport mechanism in the Elovich release profile. This profile explains the rapid release of adsorbed thymol on the host's outer surface and the slow release of thymol placed in the inner parts of the host [74]. The post-treatment process can be suggested to improve the accessibility of the zeolite X's surface area and increase the amount of adsorbed thymol. Accordingly, it can be postulated that the superior release of thymol encapsulated from zeolite TX samples exhibited a unique thymol release profile with respect to their counterparts.

6.4. Antimicrobial Assays

The antimicrobial assays of thymol loaded zeolite X were assessed against *P. aeruginosa* as a gram-negative bacterium, *S. aureus* as a gram-positive bacterium, and

C. albicans as a yeast. The disc diffusion assays' results are graphically illustrated in Figure 6.6. The detailed results are in Appendix D.
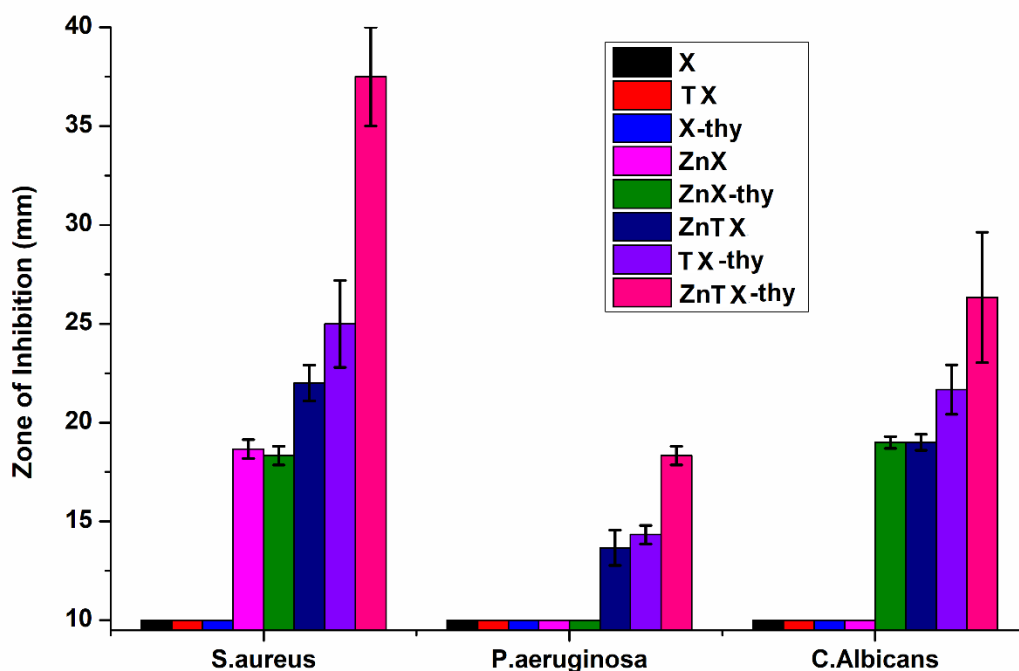
Figure 6. 5. Disc diffusion tests for thymol loaded zeolite X samples.

According to Figure 6.6, neither X nor TX exhibited any antimicrobial activity against all three microorganisms. The ion-exchange of Zn^{2+} cations in the zeolite framework offered an antimicrobial activity (i.e., ZnX and ZnTX). The fact that ZnX showed activity towards *S. aureus*, but not to *P. aeruginosa* and *C. albicans,* which can be explained by the low ion-exchange concentration of Zn^{2+}. Similar result was observed in the literature [64]. Also, ZnTX provides 22.0 mm, 13.7 mm, and 19.0 mm zone of inhibition against *S. aureus, P. aeruginosa,* and *C. albicans,* respectively, whereas TX did not have any antimicrobial property.

The literature stated that thymol molecules exhibited antimicrobial activity against a wide range of microorganisms [18]. However, X-thy did not provide any antimicrobial activity. This could be due to insufficient adsorption of thymol in zeolite X crystals resulting in depleted antimicrobial activity. However, the post-treatment process aiming to enlarge the pore structure resulted in the generation of a superior antimicrobial activity due to higher thymol adsorption. Accordingly, TX-thy exhibited a remarkable antimicrobial activity for all microorganisms (i.e., 25.0 mm, 14.3 mm, and 21.7 mm for *S. aureus, P. aeruginosa,* and *C. albicans,* respectively).

Moreover, it seems that the addition of Zn^{2+} cations in the framework brought about an increased antimicrobial activity into the zeolite structure (ZnTX-thy) once compared to TX-thy samples with no additional cations. This unique zeolitic system (i.e., ZnTX-thy) exhibited 37.5 mm, 18.3 mm, and 26.3 mm zone of inhibition against *S. aureus, P. aeruginosa,* and *C. albicans,* respectively.

In summary, it is believed that the post-treatment process used to create enlarged microporosity in addition to combined ion-exchange and thymol encapsulation resulted in exceptional antimicrobial activity for all microorganisms. Such behavior could neither be obtained upon Zn^{2+}/thymol only counterparts (ZnTX or TX-thy) nor un-treated (ZnX or TX) samples. Thus, it was seen that post-treatment or ion exchange processes alone did not present any significant antimicrobial activity. Applying a combination of the post-treatment and ion-exchange processes provided an enhanced activity throughout the study.

CONCLUSIONS AND FURTHER SUGGESTIONS

This thesis aimed to establish a novel antimicrobial porous structure for the purpose of investigating different agents, such as metallic cations and/or essential oil compounds, to obtain enhanced activity and longer release profiles. In the first part of the study, the process to convert impurity containing natural kaolin into a highly demanded agent with antibacterial activities (99.99 % activity) and desired esthetic criteria (ΔE value < 1) showing universally and industrially accepted standards was explored. Alterations of metal ion concentration in zeolite crystals and their composite forming formulations were investigated. For this purpose, antibacterial metal cations such as Ag^+ and Zn^{2+} exchanged zeolites due to their biocidal activities were used for obtaining electrostatic powder paint coatings. It was found that decreasing Ag^+ ion from 6 to 2 wt.% in addition to Zn^{2+} ion of 12 wt.% resulted in an antibacterial efficacy with 99.99% and 99.96% of bacteria reduction for *E. coli* and *S. aureus*, respectively. The addition of Zn^{2+} ion provided to lessen Ag^+ amount for keeping the antibacterial properties essentially as expected, which was essential for meeting the requirements of industrial esthetic regulations. Accordingly, the addition of binary ion-exchanged zeolites as filler in electrostatic powder paint by an amount of only 0.8 wt.% loading was found to provide three advantages; low cost owing to using kaolin as a raw material, healthier and more economical approach due to utilizing less amount of Ag^+ source; and finally improved color quality.

The toxic impact of silver on the environment makes its use for antimicrobial applications controversial, and the need for alternative environmentally-friendly antimicrobials comes to be crucial. In the second part of this thesis, volatile and difficult to implement thymol molecules were encapsulated into a post-treated zeolitic structure to meet this need. This part highlighted that the post-treated microporous ETS-10 crystals supported a higher amount of thymol encapsulation to allow long-term thymol release and higher antimicrobial activity. The superior accessibility of the

surface area of the post-treated structure was critical to attaining this criterion. The H_2O_2 treatment introduced a gradual increase in surface area and pore volume of ETS-10 channels. In this study, higher accessibility was observed to promote higher encapsulation of thymol in ETS-10 crystals. Furthermore, the formation of defects in the ETS-10 framework after the H_2O_2 treatment led to different release profiles of ETS-10 samples, i.e., Higuchi release model for ETS-thy and Elovich release model for 10-ETS-thy and 30-ETS-thy. The thymol release time was prolonged up to 4 days and 12 hours. Moreover, all samples presented antimicrobial activity against *P. aeruginosa*, *S. aureus*, and *C. albicans.* In summary, the antimicrobial activity of thymol loaded ETS-10 samples gradually increased with increased thymol loading.

In the last part of this thesis, a strategic approach exploiting Zn^{2+} exchange after the post-treatment process of zeolite was adapted to enhance antimicrobial activity besides the adsorption of thymol molecules. To obtain this novel antimicrobial host-guest system, firstly, commercial zeolite X was treated with the aqueous solutions of KCl, NH_4Cl, and Na_2H_2EDTA, consecutively. The post-treated zeolite X crystals were exchanged with Zn^{2+} cations, which was studied extensively in the first part of this thesis based on the fact that Zn is less harmful to the environment. Thereby, post-treated zeolite X crystals were ion-exchanged with Zn^{2+}, followed by thymol encapsulation. The consecutive post-treatment procedures provided controlled dealumination of the structure, which offered higher accessibility of surface area for thymol molecules. The final product developed to obtain a novel hierarchical material with combined Zn^{2+} ion-exchanged and thymol-loaded features exhibited higher antimicrobial activity than their counterparts. The key to this achievement was to utilize three routes together, namely Zn^{2+} ion-exchanged, thymol adsorption, and post-treatment process applied to zeolitic frameworks.

It had been crucial to determine the appropriate release medium and process depending on the applications of thymol-loaded zeolitic systems. In this thesis, the thymol release assays from zeolitic channels were assessed in the liquid phase based

on the drug delivery process in the literature. Besides, the preliminary studies of thymol release in open-air at room temperature, which was not stated in the thesis, were also performed. It was observed that thymol-loaded zeolitic systems did not exhibit any antimicrobial activity after the release process was accomplished in a liquid medium within the investigated time frame. On the contrary, the preliminary results of thymol release in open-air showed that the post-treated ETS-10 crystals with thymol loading exhibited antimicrobial activity against *S. aureus* for up to one year. Furthermore, in antimicrobial applications involving direct contact, the surface of zeolites and zeo-type materials can be chemically modified to attain suitable surface groups for the chemical bonding of thymol molecules. The chemical bonding attained between thymol molecules and zeolite surface groups could offer prolonged antimicrobial activity upon direct contact lasting for years.

In conclusion, global reliance on sustainable antimicrobials has led to dependence on susceptible plants such as essential oils. However, a greater effort is needed to industrialize these essential oils. Promoting essential oil encapsulation into a zeolitic framework presented an opportunity to process them easily. The hierarchical pore structures provided from the post-treatment techniques offered a higher antimicrobial activity and tailorable release. Also, the presence of Zn^{2+} in this modified structure had significant contributions, which offered a sustainable and environmentally friendly antimicrobial structure.

REFERENCES

1. Sim, W., Barnard, R. T., Blaskovich, M. A. T. & Ziora, Z. M. Antimicrobial silver in medicinal and consumer applications: A patent review of the past decade (2007–2017). *Antibiotics* **7**, 1–15 (2018).

2. Yamada, K. *The origins of acupuncture, moxibustion, and decoction : the two phases of the formation of ancient medicine : the origins of acupuncture and moxibustion, the origins of decoction*. (International Research Center for Japanese Studies, 1998).

3. Möhler, J. S., Sim, W., Blaskovich, M. A. T., Cooper, M. A. & Ziora, Z. M. Silver bullets: A new lustre on an old antimicrobial agent. *Biotechnol. Adv.* **36**, 1391–1411 (2018).

4. Matsumura, Y., Yoshikata, K., Kunisaki, S. & Tsuchido, T. Mode of bactericidal action of silver zeolite and its comparison with that of silver nitrate mode of bactericidal action of silver zeolite and its comparison with that of silver nitrate. *Appl. Environ. Microbiol.* **69**, 4278–4281 (2003).

5. Yamanaka, M., Hara, K. & Kudo, J. Bactericidal Actions of a Silver Ion Solution on Escherichia coli , Studied by Energy-Filtering Transmission Electron Microscopy and Proteomic Analysis Bactericidal Actions of a Silver Ion Solution on Escherichia coli , Studied by Energy-Filtering Transmi. *Appl. Environ. Microbiol.* **71**, 7589–7593 (2005).

6. Kwakye-Awuah, B., Williams, C., Kenward, M. A. & Radecka, I. Antimicrobial action and efficiency of silver-loaded zeolite X. *J. Appl. Microbiol.* **104**, 1516–1524 (2008).

7. USTAOĞLU İYİGÜNDOĞDU, Z., DEMİRCİ, S., BAÇ, N. & ŞAHİN, F. Development of durable antimicrobial surfaces containing silver- and zinc-ion–exchanged zeolites. *Turkish J. Biol.* **38**, 420–427 (2014).

8. Mohammed Fayaz, A. *et al.* Inactivation of microbial infectiousness by silver nanoparticles-coated condom: A new approach to inhibit HIV- and HSV-transmitted infection. *Int. J. Nanomedicine* **7**, 5007–5018 (2012).

9. Said, D. E., ElSamad, L. M. & Gohar, Y. M. Validity of silver, chitosan, and curcumin nanoparticles as anti-Giardia agents. *Parasitol. Res.* **111**, 545–554 (2012).

10. Feng, Q. L. *et al.* A mechanistic study of the antibacterial effect of silver ions on <I>Escherichia coli</I> and <I>Staphylococcus aureus</I>. *Journal of Biomedical Materials Research* vol. 52 662–668 (2000).

11. Salim, M. M. & Malek, N. A. N. N. Characterization and antibacterial activity of silver exchanged regenerated NaY zeolite from surfactant-modified NaY zeolite. *Mater. Sci. Eng. C* **59**, 70–77 (2016).

12. Haase, H., Overbeck, S. & Rink, L. Zinc supplementation for the treatment or prevention of disease: Current status and future perspectives. *Exp. Gerontol.* **43**, 394–408 (2008).

13. McMaster, J. *Bioinorganic chemistry. Annual Reports on the Progress of Chemistry - Section A* vol. 101 (2005).

14. Vallee, B. L. & Falchuk, K. H. *The biochemical basis of zinc physiology. Physiological Reviews* vol. 73 (1993).

15. Palmiter, R. D. & Findley, S. D. Cloning and functional characterization of a mammalian zinc transporter that confers resistance to zinc. *EMBO J.* **14**, 639–649 (1995).

16. Sugarman, B. Zinc and infection. *Rev. Infect. Dis.* **5**, 137–147 (1983).

17. Dimapilis, E. A. S., Hsu, C. S., Mendoza, R. M. O. & Lu, M. C. Zinc oxide nanoparticles for water disinfection. *Sustain. Environ. Res.* **28**, 47–56 (2018).

18. Bakkali, F., Averbeck, S., Averbeck, D. & Idaomar, M. Biological effects of essential oils - A review. *Food Chem. Toxicol.* **46**, 446–475 (2008).

19.   Marchese, A. *et al.* Antibacterial and antifungal activities of thymol: a brief review of the literature. *Food Chem.* **210**, 402–414 (2016).

20.   Tiwari, B. K. *et al.* Application of natural antimicrobials for food preservation. *J. Agric. Food Chem.* **57**, 5987–6000 (2009).

21.   Sikkema, J., De Bont, J. A. M. & Poolman, B. Interactions of cyclic hydrocarbons with biological membranes. *J. Biol. Chem.* **269**, 8022–8028 (1994).

22.   Sikkema, J., de Bont, J. A. & Poolman, B. Mechanisms of membrane toxicity of hydrocarbons. *Microbiol Rev* **59**, 201–222 (1995).

23.   Skandamis, P. N. & Nychas, G. J. E. Effect of oregano essential oil on microbiological and physico-chemical attributes of minced meat stored in air and modified atmospheres. *J. Appl. Microbiol.* **91**, 1011–1022 (2001).

24.   Nazzaro, F., Fratianni, F., De Martino, L., Coppola, R. & De Feo, V. Effect of essential oils on pathogenic bacteria. *Pharmaceuticals* **6**, 1451–1474 (2013).

25.   Ju, J. *et al.* Application of essential oil as a sustained release preparation in food packaging. *Trends Food Sci. Technol.* **92**, 22–32 (2019).

26.   Wang, L. H., Zeng, X. A., Wang, M. S., Brennan, C. S. & Gong, D. Modification of membrane properties and fatty acids biosynthesis-related genes in Escherichia coli and Staphylococcus aureus: Implications for the antibacterial mechanism of naringenin. *Biochim. Biophys. Acta - Biomembr.* **1860**, 481–490 (2018).

27.   Gafur, A. *et al.* From bulk to nano-delivery of essential phytochemicals: Recent progress and strategies for antibacterial resistance. *J. Mater. Chem. B* **8**, 9825–9835 (2020).

28.   Espina, L., Gelaw, T. K., de Lamo-Castellví, S., Pagán, R. & García-Gonzalo, D. Mechanism of Bacterial Inactivation by (+)-Limonene and Its Potential Use in Food Preservation Combined Processes. *PLoS One* **8**, 1–10 (2013).

29. Khan, M. S. A., Zahin, M., Hasan, S., Husain, F. M. & Ahmad, I. Inhibition of quorum sensing regulated bacterial functions by plant essential oils with special reference to clove oil. *Lett. Appl. Microbiol.* **49**, 354–360 (2009).

30. Ahmad, A., Khan, A., Akhtar, F., Yousuf, S. & Xess, I. Fungicidal activity of thymol and carvacrol by disrupting ergosterol biosynthesis and membrane integrity against Candida. 41–50 (2011) doi:10.1007/s10096-010-1050-8.

31. Castro, R. D. De *et al.* Antifungal activity and mode of action of thymol and its synergism with nystatin against Candida species involved with infections in the oral cavity : an in vitro study. *BMC Complement. Altern. Med.* 1–7 (2015) doi:10.1186/s12906-015-0947-2.

32. Kh, G. I., Abdel, M. A. & Abdelgaleil, S. A. M. Comparative antifungal activities and biochemical effects of monoterpenes on plant pathogenic fungi. *Pestic. Biochem. Physiol.* **103**, 56–61 (2012).

33. P. Payra, P.K. Dutta, in: S.M. Auerbach, K.A. Carrado, P. K. D. *Handbook of Zeolite Science and Technology*. (Marcel Dekker, 2003).

34. Asel Sartbaeva, Stephen A. Wells, M. M. J. T. & M. F. T. The flexibility window in zeolites. *Nat. Mater.* **5**, 962–965 (2006).

35. Verboekend, D. New Hierarchical Zeolite Catalysts by Post-Synthetic Design. 221 (2012) doi:10.3929/ethz-a-007595445.

36. C. Baerlocher, L. B. M. Database of Zeolite Structures. http://www.iza-structure.org/databases.

37. R. Xu, W. Pang, J. Yu, Q. Huo, J. C. *Chemistry of Zeolites and Related Porous Materials: Synthesis and Structure*. (Wiley, 2007).

38. Rocha, J. & Anderson, M. W. Microporous Titanosilicates and other Novel Mixed Octahedral-Tetrahedral Framework Oxides. *Eur. J. Inorg. Chem.* **2000**, 801–818 (2000).

39. Collins, F., Rozhkovskaya, A., Outram, J. G. & Millar, G. J. A critical review

of waste resources, synthesis, and applications for Zeolite LTA. *Microporous Mesoporous Mater.* **291**, 109667 (2020).

40.   Busca, G. Acidity and basicity of zeolites: A fundamental approach. *Microporous Mesoporous Mater.* **254**, 3–16 (2017).

41.   Nakano, T. & Nozue, Y. Orbital degeneracy and magnetic properties of potassium clusters incorporated into nanoporous crystals of zeolite A. *J. Comput. Methods Sci. Eng.* **7**, 443–462 (2007).

42.   Baerlocher, C. & McCusker, L.B., Olson, D. H. Atlas of Zeolite Framework Types. 194–195 http://www.iza-structure.org/databases/books/Atlas_6ed.pdf.

43.   Faux, D. A., Smith, W. & Forester, T. R. Molecular dynamics studies of hydrated and dehydrated Na+-zeolite-4A. *J. Phys. Chem. B* **101**, 1762–1768 (1997).

44.   Xu, R., Pang, W., Yu, J., Huo, Q. & Chen, J. *Chemistry of Zeolites and Related Porous Materials: Synthesis and Structure*. *Chemistry of Zeolites and Related Porous Materials: Synthesis and Structure* (Wiley, 2007, 2007). doi:10.1002/9780470822371.

45.   Tekin, R., Bac, N., Warzywoda, J. & Sacco, A. Encapsulation of a fragrance molecule in zeolite X. *Microporous Mesoporous Mater.* **215**, 51–57 (2015).

46.   Li, Z. *et al.* Encapsulation of Highly Volatile Fragrances in y Zeolites for Sustained Release: Experimental and Theoretical Studies. *ACS Omega* **5**, 31925–31935 (2020).

47.   Kuznicki, S. M. Preparation of small-pored crystalline titanium molecular sieve zeolites. 1–8 (1990).

48.   Zimmerman, A. M., Doren, D. J. & Lobo, R. F. Electronic and geometric properties of ETS-10: QM/MM studies of cluster models. *J. Phys. Chem. B* **110**, 8959–8964 (2006).

49.   Ji, Z. *et al.* The role of silver nanoparticles on silver modified titanosilicate

ETS-10 in visible light photocatalysis. *Appl. Catal. B Environ.* **102**, 323–333 (2011).

50. Anderson, Michael W *et al.* structure of the microporous titanosilicate ETS-10. *Lett. to Nat.* **367**, 374–351 (1994).

51. Anderson, M. W. *et al.* Microporous titanosilicate ETS-10: A structural survey. *Philos. Mag. Part B* **71**, 813–841 (1995).

52. Jeong, N. C., Lee, M. H. & Yoon, K. B. Length-Dependent Band-Gap Shift of TiO32− Molecular Wires Embedded in Zeolite ETS-10. *Angew. Chemie* **119**, 5972–5976 (2007).

53. Oleksiienko, O., Wolkersdorfer, C. & Sillanpää, M. Titanosilicates in cation adsorption and cation exchange – A review. *Chem. Eng. J.* **317**, 570–585 (2017).

54. Galioglu, S. *et al.* Photochromic behavior of silver nanoparticle incorporated titanosilicate ETS-10 films. *Microporous Mesoporous Mater.* **196**, 136–144 (2014).

55. Galioğlu, S., Zahmakiran, M., Eren Kalay, Y., Özkar, S. & Akata, B. Effect of silver encapsulation on the local structure of titanosilicate ETS-10. *Microporous Mesoporous Mater.* **159**, 1–8 (2012).

56. Atienzar, P., Valencia, S., Corma, A. & García, H. Titanium-containing zeolites and microporous molecular sieves as photovoltaic solar cells. *ChemPhysChem* **8**, 1115–1119 (2007).

57. Yilmaz, B., Warzywoda, J. & Sacco, A. Spectroscopic characterization of the quantum wires in titanosilicates ETS-4 and ETS-10. *Nanotechnology* **17**, 4092–4099 (2006).

58. Malachov??, K., Praus, P., Rybkov??, Z. & Koz??k, O. Antibacterial and antifungal activities of silver, copper and zinc montmorillonites. *Appl. Clay Sci.* **53**, 642–645 (2011).

59. Porta, P. E. P. & Chu, A. E. Umted States Patent [191. (1993).

60. Top, A. & Ülkü, S. Silver, zinc, and copper exchange in a Na-clinoptilolite and resulting effect on antibacterial activity. *Appl. Clay Sci.* **27**, 13–19 (2004).

61. Woo, K. J. *et al.* Antibacterial activity and mechanism of action of the silver ion in Staphylococcus aureus and Escherichia coli. *Appl. Environ. Microbiol.* **74**, 2171–2178 (2008).

62. Kaali, P. *et al.* The influence of Ag +, Zn 2+ and Cu 2+ exchanged zeolite on antimicrobial and long term in vitro stability of medical grade polyether polyurethane. *Express Polym. Lett.* **5**, 1028–1040 (2011).

63. Kaali, P. & Czél, G. Single , binary and ternary ion exchanged zeolite as an effective bioactive filler for biomedical polymer composites. **729**, 99–104 (2013).

64. Demirci, S., Ustao??lu, Z., Yilmazer, G. A., Sahin, F. & Ba??, N. Antimicrobial properties of zeolite-X and zeolite-A ion-exchanged with silver, copper, and zinc against a broad range of microorganisms. *Appl. Biochem. Biotechnol.* **172**, 1652–1662 (2014).

65. Pereyra, A. M., Gonzalez, M. R., Rosato, V. G. & Basaldella, E. I. A-type zeolite containing Ag+/Zn2+ as inorganic antifungal for waterborne coating formulations. *Prog. Org. Coatings* **77**, 213–218 (2014).

66. Dutta, P. & Wang, B. Zeolite-supported silver as antimicrobial agents. *Coord. Chem. Rev.* **383**, 1–29 (2019).

67. López, S., Domínguez, A., Guerrero, Á. & Quero, C. Inhibitory effect of thymol on pheromone-mediated attraction in two pest moth species. *Sci. Rep.* **11**, 1–10 (2021).

68. Chai, X. H., Lin, R. H., Wu, K. G. & Li, S. R. Characterization of β-Cyclodextrin-Thymol Inclusion Complexes. *Adv. Mater. Res.* **233**–**235**, 1766–1773 (2011).

69. Helander, I. M. *et al.* Characterization of the Action of Selected Essential Oil Components on Gram-Negative Bacteria. *J. Agric. Food Chem.* **46**, 3590–3595 (1998).

70. Dorman, H. J. & Deans, S. G. Antimicrobial agents from plants: antibacterial activity of plant volatile oils. *J. Appl. Microbiol.* **88**, 308–316 (2000).

71. Ultee, A., Bennik, M. H. J. & Moezelaar, R. The Phenolic Hydroxyl Group of Carvacrol Is Essential for Action against the Food-Borne Pathogen Bacillus cereus The Phenolic Hydroxyl Group of Carvacrol Is Essential for Action against the Food-Borne Pathogen Bacillus cereus. *Appl. Environ. Microbiol.* **68**, 1561–1568 (2002).

72. Prakash, B. *et al.* Nanoencapsulation: An efficient technology to boost the antimicrobial potential of plant essential oils in food system. *Food Control* **89**, 1–11 (2018).

73. Jobdeedamrong, A., Jenjob, R. & Crespy, D. Encapsulation and Release of Essential Oils in Functional Silica Nanocontainers. *Langmuir* **34**, 13235–13243 (2018).

74. Mattos, B. D. *et al.* Controlled biocide release from hierarchically-structured biogenic silica: surface chemistry to tune release rate and responsiveness. *Sci. Rep.* **8**, 1–11 (2018).

75. Ponce Cevallos, P. A., Buera, M. P. & Elizalde, B. E. Encapsulation of cinnamon and thyme essential oils components (cinnamaldehyde and thymol) in ??-cyclodextrin: Effect of interactions with water on complex stability. *J. Food Eng.* **99**, 70–75 (2010).

76. Rukmani, A. & Sundrarajan, M. Inclusion of antibacterial agent thymol on -cyclodextrin-grafted organic cotton. *J. Ind. Text.* **42**, 132–144 (2011).

77. Ciobanu, A. *et al.* Inclusion interactions of cyclodextrins and crosslinked cyclodextrin polymers with linalool and camphor in Lavandula angustifolia

essential oil. *Carbohydr. Polym.* **87**, 1963–1970 (2012).

78. del Toro-Sánchez, C. L. *et al.* Controlled release of antifungal volatiles of thyme essential oil from β-cyclodextrin capsules. *J. Incl. Phenom. Macrocycl. Chem.* **67**, 431–441 (2010).

79. Marreto, R. N. *et al.* Thermal analysis and gas chromatography coupled mass spectrometry analyses of hydroxypropyl-β-cyclodextrin inclusion complex containing Lippia gracilis essential oil. *Thermochim. Acta* **475**, 53–58 (2008).

80. Hosseini, S. F., Zandi, M., Rezaei, M. & Farahmandghavi, F. Two-step method for encapsulation of oregano essential oil in chitosan nanoparticles: Preparation, characterization and in vitro release study. *Carbohydr. Polym.* **95**, 50–56 (2013).

81. Paula, H. C. B., Sombra, F. M., Abreu, F. O. M. S. & De Paula, R. C. M. Lippia sidoides essential oil encapsulation by angico gum/chitosan nanoparticles. *J. Braz. Chem. Soc.* **21**, 2359–2366 (2010).

82. Liolios, C. C., Gortzi, O., Lalas, S., Tsaknis, J. & Chinou, I. Liposomal incorporation of carvacrol and thymol isolated from the essential oil of Origanum dictamnus L. and in vitro antimicrobial activity. *Food Chem.* **112**, 77–83 (2009).

83. Shemesh, R. *et al.* Antibacterial and antifungal LDPE films for active packaging. *Polym. Adv. Technol.* **26**, 110–116 (2015).

84. Shemesh, R. *et al.* LDPE/clay/carvacrol nanocomposites with prolonged antimicrobial activity. *J. Appl. Polym. Sci.* **132**, 1–8 (2015).

85. Martins, I. M., Rodrigues, S. N., Barreiro, M. F. & Rodrigues, a E. Release Studies of Thymol and p-Cymene from Polylactide Microcapsules. *Ind. Eng. Chem. Res.* **51**, 11565–11571 (2012).

86. Mastromatteo, M., Barbuzzi, G., Conte, A. & Del Nobile, M. A. Controlled release of thymol from zein based film. *Innov. Food Sci. Emerg. Technol.* **10**,

222–227 (2009).

87. Ya-Lin Pan, Robert, You, jing-Feng, Caravajal, Gregory Stephen, Graves, Sharon Anne, Mueller, W. R. Perfume delivery system comprising zeolites. (1997).

88. Sabehat, A. Active materials incorporating microporous solids and essential oils. (2008).

89. Janatova, A. *et al.* Long-term antifungal activity of volatile essential oil components released from mesoporous silica materials. *Ind. Crops Prod.* **67**, 216–220 (2015).

90. Paseta, L., Simón-Gaudó, E., Gracia-Gorría, F. & Coronas, J. Encapsulation of essential oils in porous silica and MOFs for trichloroisocyanuric acid tablets used for water treatment in swimming pools. *Chem. Eng. J.* **292**, 28–34 (2016).

91. Hartmann, M. Hierarchical zeolites: A proven strategy to combine shape selectivity with efficient mass transport. *Angew. Chemie - Int. Ed.* **43**, 5880–5882 (2004).

92. Jia, X., Khan, W., Wu, Z., Choi, J. & Yip, A. C. K. Modern synthesis strategies for hierarchical zeolites: Bottom-up versus top-down strategies. *Adv. Powder Technol.* **30**, 467–484 (2019).

93. Jiang, J. *et al.* Synthesis and structure determination of the hierarchical meso-microporous zeolite ITQ-43. *Science* **333**, 1131–1134 (2011).

94. Inayat, A., Knoke, I., Spiecker, E. & Schwieger, W. Assemblies of mesoporous FAU-type zeolite nanosheets. *Angew. Chemie - Int. Ed.* **51**, 1962–1965 (2012).

95. Egeblad, K., Christensen, C. H., Kustova, M. & Christensen, C. H. Templating mesoporous zeolites. *Chem. Mater.* **20**, 946–960 (2008).

96. Zhu, K., Egeblad, K. & Christensen, C. H. Mesoporous carbon prepared from

carbohydrate as hard template for hierarchical zeolites. *Eur. J. Inorg. Chem.* 3955–3960 (2007) doi:10.1002/ejic.200700218.

97.   Corma, A., Díaz-Cabañas, M. J., Martínez-Triguero, J., Rey, F. & Rius, J. A large-cavity zeolite with wide pore windows and potential as an oil refining catalyst. *Nature* **418**, 514–517 (2002).

98.   Ogura, M. *et al.* Alkali-treatment technique - New method for modification of structural and acid-catalytic properties of ZSM-5 zeolites. *Appl. Catal. A Gen.* **219**, 33–43 (2001).

99.   Naik, S. P., Chiang, A. S. T., Thompson, R. W. & Huang, F. C. Formation of silicalite-1 hollow spheres by the self-assembly of nanocrystals. *Chem. Mater.* **15**, 787–792 (2003).

100.   Schwieger, W. *et al.* Hierarchy concepts: Classification and preparation strategies for zeolite containing materials with hierarchical porosity. *Chem. Soc. Rev.* **45**, 3353–3376 (2016).

101.   Zhang, X. *et al.* Synthesis of Self-Pillared Zeolite Nanosheets by Repetitive Branching. *Science (80-.).* **336**, 1684–1687 (2012).

102.   Chal, R., Gérardin, C., Bulut, M. & VanDonk, S. Overview and Industrial Assessment of Synthesis Strategies towards Zeolites with Mesopores. *ChemCatChem* **3**, 67–81 (2011).

103.   Van Donk, S., Janssen, A. H., Bitter, J. H. & De Jong, K. P. Generation, characterization, and impact of mesopores in zeolite catalysts. *Catal. Rev. - Sci. Eng.* **45**, 297–319 (2003).

104.   Groen, J. C., Moulijn, J. A. & Pérez-Ramírez, J. Alkaline posttreatment of MFI zeolites. From accelerated screening to scale-up. *Ind. Eng. Chem. Res.* **46**, 4193–4201 (2007).

105.   Otomo, R., Yokoi, T., Kondo, J. N. & Tatsumi, T. Dealuminated Beta zeolite as effective bifunctional catalyst for direct transformation of glucose to 5-

hydroxymethylfurfural. *Appl. Catal. A Gen.* **470**, 318–326 (2014).

106. Thibault-Starzyk, F. *et al.* Quantification of enhanced acid site accessibility in hierarchical zeolites - The accessibility index. *J. Catal.* **264**, 11–14 (2009).

107. Ogura, M. *et al.* Formation of uniform mesopores in ZSM-5 zeolite through treatment in alkaline solution. *Chem. Lett.* 882–883 (2000) doi:10.1246/cl.2000.882.

108. Groen, J. C., Jansen, J. C., Moulijn, J. A. & Pérez-Ramírez, J. Optimal aluminum-assisted mesoporosity development in MFI zeolites by desilication. *J. Phys. Chem. B* **108**, 13062–13065 (2004).

109. Groen, J. C., Abelló, S., Villaescusa, L. A. & Pérez-Ramírez, J. Mesoporous beta zeolite obtained by desilication. *Microporous Mesoporous Mater.* **114**, 93–102 (2008).

110. Abelló, S., Bonilla, A. & Pérez-Ramírez, J. Mesoporous ZSM-5 zeolite catalysts prepared by desilication with organic hydroxides and comparison with NaOH leaching. *Appl. Catal. A Gen.* **364**, 191–198 (2009).

111. Tsai, S. T. *et al.* Effects of pore structure of post-treated TS-1 on phenol hydroxylation. *Catal. Today* **148**, 174–178 (2010).

112. Peréz-Ramírez, J., Verboekend, D., Bonilla, A. & Abelló, S. Zeolite catalysts with tunable hierarchy factor by pore-growth moderators. *Adv. Funct. Mater.* **19**, 3972–3979 (2009).

113. Verboekend, D., Keller, T. C., Mitchell, S. & Pérez-Ramírez, J. Hierarchical FAU- and LTA-type zeolites by post-synthetic design: A new generation of highly efficient base catalysts. *Adv. Funct. Mater.* **23**, 1923–1934 (2013).

114. Verboekend, D., Vilé, G. & Pérez-Ramírez, J. Hierarchical y and USY zeolites designed by post-synthetic strategies. *Adv. Funct. Mater.* **22**, 916–928 (2012).

115. Goa, Y., Yoshitake, H., Wu, P. & Tatsumi, T. Controlled detitanation of ETS-

10 materials through the post-synthetic treatment and their applications to the liquid-phase epoxidation of alkenes. *Microporous Mesoporous Mater.* **70**, 93–101 (2004).

116. Lv, L., Zhou, J. K., Su, F. & Zhao, X. S. Local structure changes of microporous titanosilicate ETS-10 upon acid treatment. *J. Phys. Chem. C* **111**, 773–778 (2007).

117. Pavel, C. C., Park, S. H., Dreier, A., Tesche, B. & Schmidt, W. Structural defects induced in ETS-10 by postsynthesis treatment with H 2O2 solution. *Chem. Mater.* **18**, 3813–3820 (2006).

118. Llabrés i Xamena, F. X. *et al.* Enhancement of the ETS-10 titanosilicate activity in the shape-selective photocatalytic degradation of large aromatic molecules by controlled defect production. *J. Am. Chem. Soc.* **125**, 2264–2271 (2003).

119. Beyer, H. K. *Molecular Sieves*. (Springer-Verlag, 2002).

120. Du, C. & Yang, H. Synthesis and characterization of zeolite 4A-type desiccant from kaolin. *Am. Mineral.* **95**, 741–746 (2010).

121. Rezaeinia, H., Ghorani, B., Emadzadeh, B. & Mohebbi, M. Prolonged-release of menthol through a superhydrophilic multilayered structure of balangu (Lallemantia royleana)-gelatin nanofibers. *Mater. Sci. Eng. C* **115**, 111115 (2020).

122. Robertson, A. R. The CIE 1976 color-difference formulae. *Color Res Appl* 7–11 (1977).

123. Wu, I. Y., Bala, S., Škalko-Basnet, N. & di Cagno, M. P. Interpreting non-linear drug diffusion data: Utilizing Korsmeyer-Peppas model to study drug release from liposomes. *Eur. J. Pharm. Sci.* **138**, 105026 (2019).

124. Chen, Y. *et al.* Hierarchical porous nanofibers containing thymol/beta-cyclodextrin: Physico-chemical characterization and potential biomedical

applications. *Mater. Sci. Eng. C* **115**, 111155 (2020).

125.   Pires, F. Q. *et al.* Lipid nanoparticles as carriers of cyclodextrin inclusion complexes: A promising approach for cutaneous delivery of a volatile essential oil. *Colloids Surfaces B Biointerfaces* **182**, 110382 (2019).

126.   Rangkadilok, N. *et al.* In vitro antifungal activities of longan (Dimocarpus longan Lour.) seed extract. *Fitoterapia* **83**, 545–553 (2012).

127.   Bush, K. & Dudley, M. N. *Performance Standards for Antimicrobial Disk Susceptibility Tests ; Approved Standard — Tenth Edition*. *Order A Journal On The Theory Of Ordered Sets And Its Applications* vol. 29 (2009).

128.   Murat, M., Amokrane, a & Mindrale, D. T. Synthesis of Zeolites from Thermally Activated Kaolinite. Some Observations on Nucleation and Growth. *Clay Miner.* 119–130 (1992) doi:10.1180/claymin.1992.027.1.12.

129.   Li, Q., Zhang, Y., Cao, Z., Gao, W. & Cui, L. Influence of synthesis parameters on the crystallinity and Si/Al ratio of NaY zeolite synthesized from kaolin. *Pet. Sci.* **7**, 403–409 (2010).

130.   Liu, X., Wang, Y., Cui, X., He, Y. & Mao, J. Influence of synthesis parameters on NaA zeolite crystals. *Powder Technol.* **243**, 184–193 (2013).

131.   Pak, A. & Mohammadi, T. Zeolite NaA membranes synthesis. *Desalination* **200**, 68–70 (2006).

132.   Antonic, T., Subotic, B. & Stubicar, N. Influence of gel properties on the crystallization of zeolites: Part 1: Influence of alkalinity during gel preparation on the kinetics of nucleation of zeolite A. *Zeolites* **18**, 291–300 (1997).

133.   Oliveira, M. L. M. *et al.* Adsorption of thiophene and toluene on NaY zeolites exchanged with Ag(I), Ni(II) and Zn(II). *Fuel* **88**, 1885–1892 (2009).

134.   Yang, K. & Seff, K. Structure of a very small piece of silver metal. The octahedral silver (Ag6) molecule. Two crystal structures of partially decomposed vacuum-dehydrated fully silver(1+) ion-exchanged zeolite A. *J.*

Am. Chem. Soc. **122**, 7055–7057 (1977).

135. Colyer, L. M., Greaves, G. N., Carr, S. W. & Fox, K. K. Collapse and Recrystallization Processes in Zinc-Exchanged Zeolite-A : A Combined X-ray Diffraction , XAFS , and NMR Study. *J. Phys. Chem. B* **101**, 10105–10114 (1997).

136. Miola, M. *et al.* Silver nanocluster-silica composite antibacterial coatings for materials to be used in mobile telephones. *Appl. Surf. Sci.* **313**, 107–115 (2014).

137. Umadevi, K. & Krishnaveni, M. Antibacterial activity of pigment produced from Micrococcus luteus KF532949. *Int. J. Chem. Anal. Sci.* **4**, 149–152 (2013).

138. Ferreira, L., Guedes, J. F., Almeida-Aguiar, C., Fonseca, A. M. & Neves, I. C. Microbial growth inhibition caused by Zn/Ag-Y zeolite materials with different amounts of silver. *Colloids Surfaces B Biointerfaces* **142**, 141–147 (2016).

139. Das, T. K., Chandwadkar, A. J. & Sivasanker, S. Preparation, characterization and catalytic properties of the microporous titanosilicate, ETS-10. *Bull. Mater. Sci.* **17**, 1143–1153 (1994).

140. Mihailova, B., Valtchev, V., Mintova, S. & Konstantinov, L. Vibrational spectra of ETS-4 and ETS-10. **2449**, 15–17.

141. HUYBRECHTS, D. R. C., VAESEN, I., Li, H. X. & JACOBS, P. A. F A C T O R S I N F L U E N C I N G T H E CATALYTIC ACTIVITY OF T I T A N I U M SILICALITES IN SELECTIVE O X I D A T I O N S D.R.C. H U Y B R E C H T S , I. VAESEN, H.X. LI and P.A. JACOBS. *Catal. Letters* **8**, 237–244 (1991).

142. Lin, W., Frei, H., Berkeley, L. & Uni, V. Photochemical and FT-IR Probing of the Active Site of Hydrogen Peroxide in Ti Silicalite Sieve. 9292–9298

(2002).

143. Ratnasamy, P. & Srinivas, D. Active Sites and Reactive Intermediates in Titanium Silicate Molecular Sieves. **48**, 1–169 (2004).

144. Geobaldo, F. *et al.* and superoxo complexes in titanium silicalite H2O. **16**, 109–115 (1992).

145. Zecchina, A. *et al.* Alkyne polymerization on the titanosilicate molecular sieve ETS-10. *Phys. Chem. Chem. Phys.* **3**, 1228–1231 (2001).

146. Bordiga, S. *et al.* Acetylene, methylacetylene and ethylacetylene polymerization on H-ZSM5: A spectroscopic study. *J. Chem. Soc. Faraday Trans.* **89**, 1843–1855 (1993).

147. Wilkenhöner, U. *et al.* Influence of pore and crystal size of crystalline titanosilicates on phenol hydroxylation in different solvents. *J. Catal.* **203**, 201–212 (2001).

148. Paarakh, M. P., Jose, P. A. N. I., Setty, C. M. & Peter, G. V. Release Kinetics – Concepts and Applications. *Int. J. Pharm. Res. Technol.* **8**, 12–20 (2019).

149. Tan, D. *et al.* Loading and in vitro release of ibuprofen in tubular halloysite. *Appl. Clay Sci.* **96**, 50–55 (2014).

150. Ben Abda, M., Schäf, O. & Zerega, Y. Ion exchange effect on asymmetric dioxins adsorption onto FAU-type X-zeolites. *Microporous Mesoporous Mater.* **217**, 178–183 (2015).

APPENDICES

A. Calculations of Thymol Calibration Curves

The calibration curve of thymol typically involves preparing a set of standards containing a known concentration of thymol solution. The standards were measured by UV-Vis spectrophotometer. The absorbance value for each standard at 274 nm, which is a characteristic thymol absorbance value, was recorded, and the relationship between the absorbance and thymol concentration was established.

The calibration curve of thymol in two different solvents, which are PBS and the solution of PBS with 3.5% wt NaCl, were drawn for both the release assays of chapter 5 and chapter 6. The calibration curves of thymol in the solvents are shown in Figure A1.
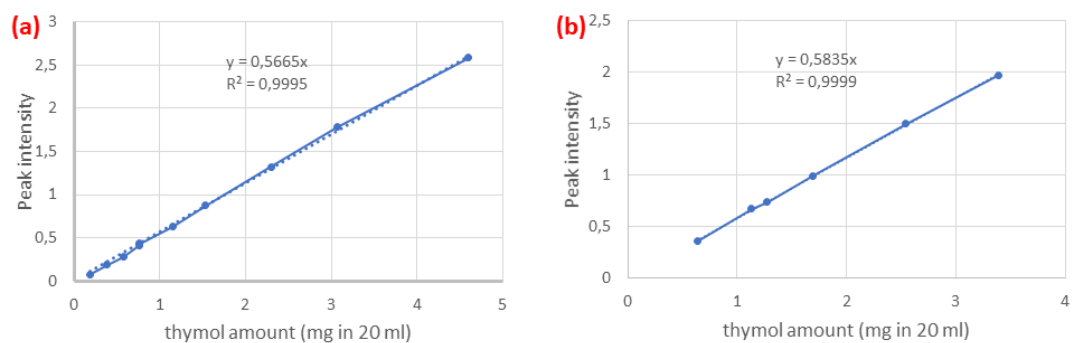

Figure A.1. The thymol calibration curve in PBS at pH 7.00 (a) and the solution of PBS with 3.5% wt NaCl at pH 7.00 (b).

B. Release Kinetics Equations

The mechanisms involved in the release of thymol from the zeolitic framework were investigated by fitting the release profiles to the following theoretical models:

Higuchi; $M_t/M_\infty = k \times t^{1/2}$ (Equation B.1)

Korsemeyer-Peppas; $M_t/M_\infty = k \times t^n$ (Equation B.2)

Elovich; $M_t = k \times \ln(t)$ (Equation B.3)

Zero Order: $M_t = M_0 + k \times t$ (Equation B.4)

Hixson-Crowell; $\sqrt[3]{M_0} - \sqrt[3]{M_t} = k \times t$ (Equation B.5)

where $M_0, M_t\ and\ M_\infty$ are the cumulative amounts of thymol released at the beginning, at time t, and at infinite time, respectively; n and k are the release exponent and the kinetic constants, respectively.

C. Antimicrobial Results of Thymol Loaded ETS-10 Samples

The inhibition zone diameters of pristine and thymol loaded ETS-10 crystals are shown in Figure C.1 and listed in Table C.1.
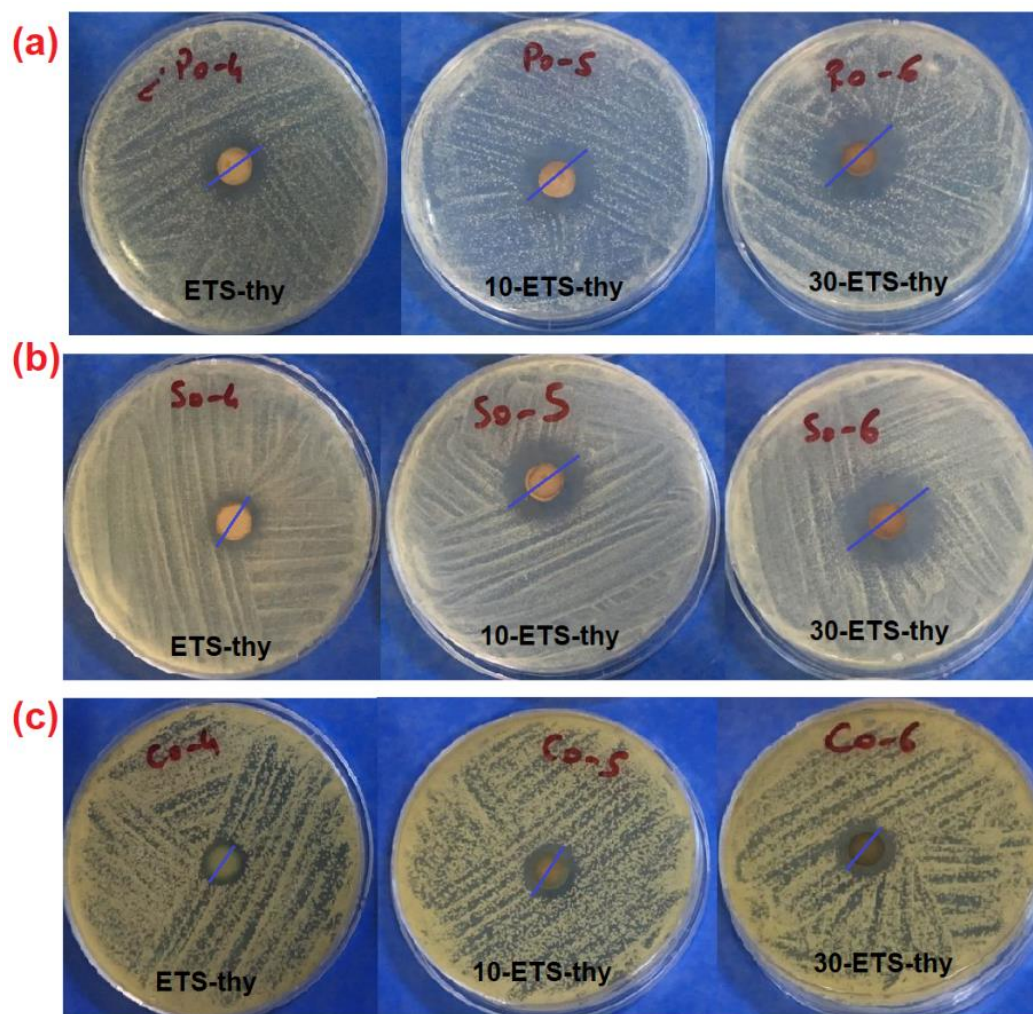

Figure C.1. The inhibition zone diameters of thymol loaded ETS-10 crystals against *P. aeruginosa* (a), *S. aureus* (b), and *C. albicans* (c).

Table C.1. The inhibition zone diameters (mm) of pristine and thymol loaded ETS-10 crystals.

Samples	*S. aureus*	*P. aeruginosa*	*C. albicans*
ETS	-	-	-
10-ETS	-	-	-
30-ETS	-	-	-
ETS-thy	13.0±0.82	15.3±0.47	11.0
10-ETS-thy	20.0	19.7±0.47	14.3±0.47
30-ETS-thy	23.0	22.3±0.94	14.3±0.47

.

D. Antimicrobial Results of Thymol Loaded Zeolite X Samples

The inhibition zone diameters of thymol loaded Zeolite X samples against *S. aureus, P. aeruginosa*, and *C. albicans* are shown in Figure D.1, Figure D.2, and Figure D.3, respectively.
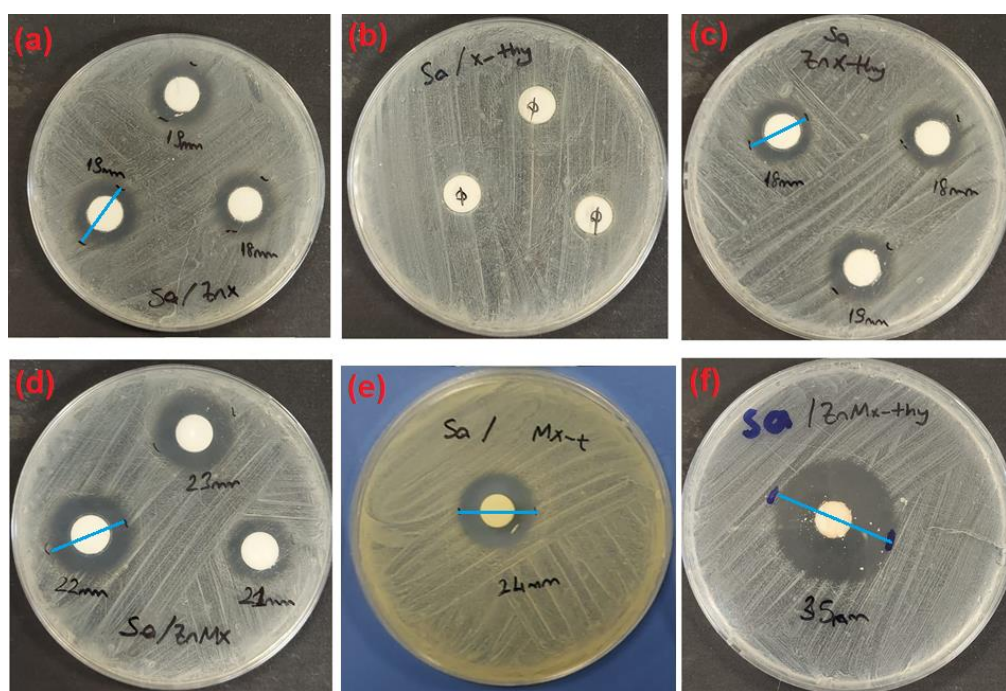

Figure D.1. The inhibition zone diameters (mm) of thymol from ZnX (a), X-thy (b), ZnX-thy (c), ZnTX (d), TX-thy (e), ZnTX-thy (f) against *S. aureus.*
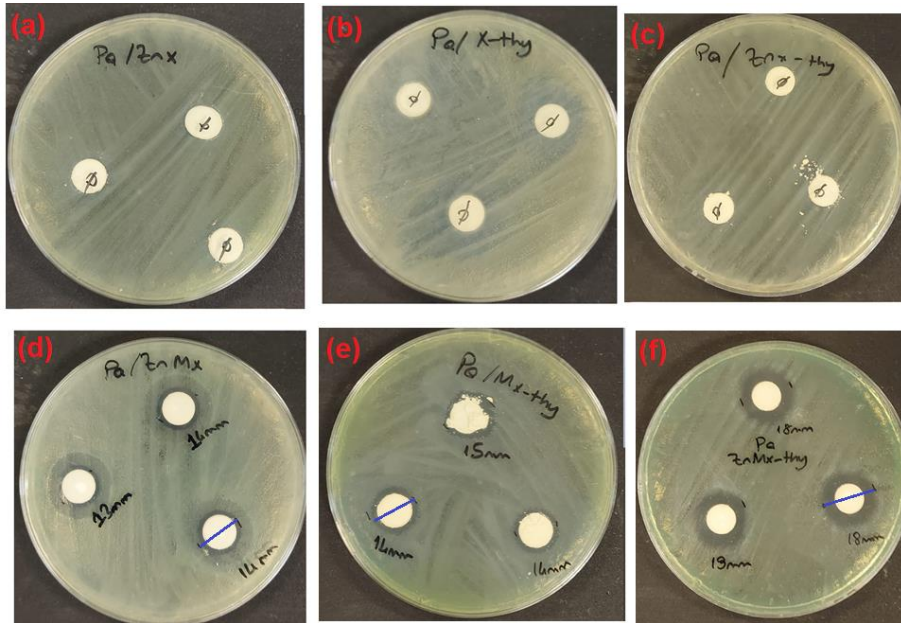
Figure D.2. The inhibition zone diameters (mm) of thymol from ZnX (a), X-thy (b), ZnX-thy (c), ZnTX (d), TX-thy (e), ZnTX-thy (f) against *P. aeruginosa*.
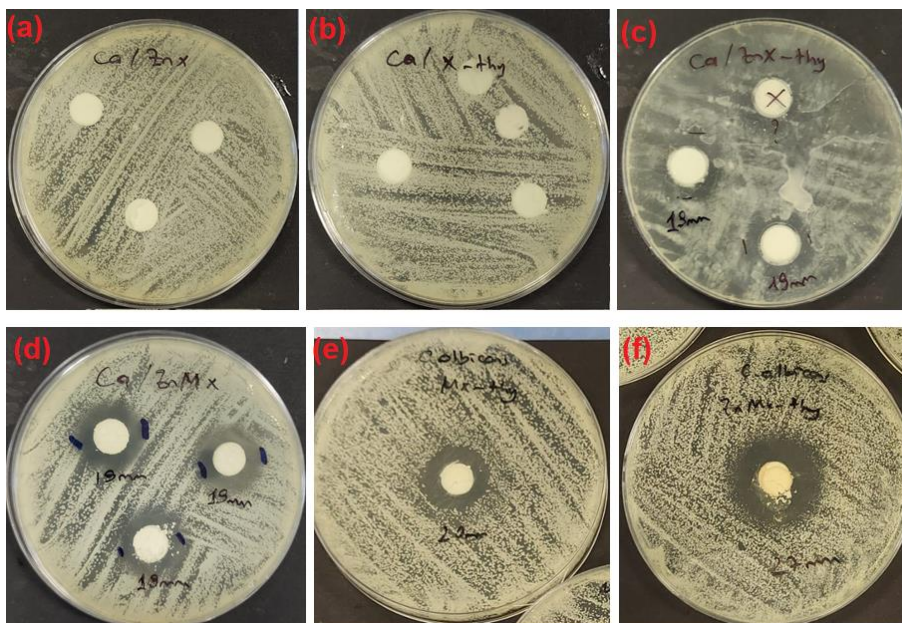

Figure D.3. The inhibition zone diameters (mm) of thymol from ZnX (a), X-thy (b), ZnX-thy (c), ZnTX (d), TX-thy (e), ZnTX-thy (f) against *C. albicans*.

The inhibition zone diameters of thymol loaded Zeolite X samples against *S. aureus, P. aeruginosa*, and *C. albicans* also was listed in Table C.1.

Table C1. The inhibition zone diameters (mm) of thymol loaded Zeolite X Samples.

Samples	*S. aureus*	*P. aeruginosa*	*C. albicans*
X	-	-	-
TX	-	-	-
X-thy	-	-	-
ZnX	18,7±0,47	-	-
ZnX-thy	18,3±0,47	-	19±0,3
ZnTX	22,0±2,4	13,7±0,47	19±0,4
MX-thy	25±2,2	14,3±0,47	21,7±1,2
ZnTX-thy	37,5±2,5	18,3±0,47	26,3±3,3

CURRICULUM VITAE

PERSONAL INFORMATION

Surname, Name	: İşler Binay, Melda
Nationality	: Turkish (TC)
E-mail	: meldasler@gmail.com

EDUCATION

Degree	Institution	Year of Graduation
MS	METU, Micro and Nanotechnology	2014
BS	METU, Department of Chemistry	2011
High School	Süleyman Demirel Science High School	2004

WORK EXPERIENCE

Year	Place	Enrollment
2017-2021	METU	Research Assistant
2012-2013	NUROL Ar-Ge Mühendislik Sanayi Ticaret A.Ş.	Project Engineer

FOREIGN LANGUAGES

Advanced English

PUBLICATIONS

A. THESIS

[1] **M. İşler**, Synthesis and Modification of Titanosilicate ETS-10: Its Role as Host in Host-Guest Systems, M. Sc. Thesis, METU, 2014

B. JOURNALS

[1] **M. İşler Binay**, D. Kart, B. Akata Antimicrobial Activity and Release Kinetics of Volatile Thymol Molecules Encapsulated into Hierarchical Microporous Titanosilicate Ets-10, in press.

[2] **M. İşler Binay**, S. K. Kirdeciler, B. Akata, Development of antibacterial powder coatings using single and binary ion-exchanged zeolite A prepared from local kaolin, Applied Clay Science 182 (2019) 105251.

[3] S. Galioglu, **M. İşler,** Z. Demircioglu, M. Koç, F.Vocanson, N. Destouches, R. Turan, B. Akata, Photochromic behavior of silver nanoparticle incorporated titanosilicate ETS-10 films, Microporous and Mesoporous Materials 196 (2014) 136-144.

C. PATENTS

[1] Termal Dayanımı Arttırılmış, Uçucu Yağ İçeren Hiyerarşik Yapılı Antimikrobiyal Zeolitik Malzemeler (Application number of invention: 2019/21513)

CERTIFICATES

[1] Scanning Electron Microscopy User Certificate, Certificate Number: ODT.S190062.1143, Central Laboratory, Middle East Technical University.

CONFERENCE AND MEETING PRESENTATIONS

[1] 15th Nanoscience and Nanotechnology Conference, "Development of Antibacterial Paint Coatings Using Single and Binary Ion-exchanged Zeolite A Prepared from Local Kaolin" (Oral Presentation), 03-06 November 2019, Antalya-Turkey.

[2] 2017 Materials Research Society (MRS) Fall Meeting and Exhibit, "Biocide Activity of Microporous Titanosilicate ETS-10 Containing Volatile Organic Compound Thymol" (Poster Presentation), 26 November- 1 December 2017, MA, USA.

[3] 7th FEZA Conference The Zeolites: Materials with Engineered Properties, "Biocide Activity of Microporous Titanosilicate ETS-10 Containing Volatile Organic Compound Thymol" (Poster Presentation), 03-07 July 2017, Sofia-Bulgaria.

[4] 18th International Zeolite Conference, "Antimicrobial Paint Coatings Containing Single and Binary Ion-exchanged Zeolite A" (Oral Presentation) 19-24 June 2016, Rio de Janeiro, Brazil.

[5] International porous and powder materials symposium and exhibition PPM 2015, "Antimicrobial Paint Coatings Containing Single and Binary Ion-exchanged Zeolite A" (Poster Presentation), 15-18 September 2015, İzmir - Turkey.

[6] 6th International Symposium on Advanced Micro and Mesoporous Materials, "Antimicrobial Paint Coatings Containing Single and Binary Ion-exchanged Zeolite A" (Poster Presentation), 6-9 September 2015, Burgas, Bulgaria.

[7] 2013 Materials Research Society (MRS) Fall Meeting and Exhibit, "Incorporation of Ruthenium Nanoparticles into Titanosilicate ETS-10: Preparation, Characterization and Photocatalytic Properties" (Poster Presentation), 01-06 December 2013, Boston, MA, USA.

[8] International porous and powder materials symposium and exhibition PPM 2013, "Ruthenium Nanoparticles Encapsulated Disordered Titanosilicate ETS-10" (Oral Presentation), 3-6 September 2013, İzmir-Turkey.

[9] 17th International Zeolite Conference (17th IZC), "Ruthenium Nanoparticles Encapsulated Disordered Titanosilicate ETS-10" (Poster Presentation), 7-12 July 2013, Moscow-Russia.

[10] 8th Nanoscience and Nanotechnology Conference, "Photochromic Behavior of Silver Nanoparticle Incorporated Titanosilicate ETS-10 Films" (Poster Presentation), 25 - 28 June 2012, Ankara-Turkey.

HOBBIES

Horse-Riding, Playing violin, Psychology